Geant4 Simulation of a Time-of-Flight Spectrometer for Measurements of Nuclear Cross Sections Relevant to Particle Therapy and Development of a Reconstruction Algorithm for the Identification of Reaction Products

Von der Fakultät für Mathematik, Informatik und Naturwissenschaften der RWTH Aachen University zur Erlangung des akademischen Grades eines Doktors der Naturwissenschaften genehmigte Dissertation vorgelegt von

Dipl.-Phys.
Jan Philipp Hermes
aus Bielefeld

Berichter: Univ.-Prof. Dr. rer. nat. Achim Stahl
Univ.-Prof. Dr. med. Michael J. Eble

Tag der mündlichen Prüfung: 23.10.2013

Abstract

Particle therapy is a cancer treatment modality, where protons or heavy ions are used to irradiate the tumor region. Accurate calculation of the energy deposition in tissue by a treatment planning program is indispensable to ensure precise irradiation of the tumor. Highest accuracy is achieved with Monte Carlo (MC) methods which, in addition to electromagnetic interactions also take nuclear interactions into account. However, these are not standardly implemented in clinical treatment planning systems today due to the need of high computing power. The simulation toolkit Geant4 is a promising MC instrument, because all physical processes are implemented. Nevertheless, it still has to be validated for energy regions where particle therapy is applied. Some nuclear cross sections are insufficiently known leading to the need for the realisation of new measurements.

On this account a time-of-flight (TOF) spectrometer is designed and engineered at the Physics Institute 3B of RWTH Aachen and simulated using the Geant4 framework. Aim of the experiment is to investigate the abundance of the most frequent reaction channels occurring from inelastic interaction with the target material by focussing a primary carbon ion beam of 2280 MeV on a polyethylene target.

The dissertation at hand addresses the Geant4 simulation of the TOF spectrometer. In this context, the simulation plays an important role in the planning phase of the detector to evaluate the detection concept. In addition, the effects of target thickness and diverse detector systems and geometries on measured variables is investigated. In a second part, the reconstruction algorithm developed in the course of this thesis is presented. Its aim is to reconstruct the kinematic variables necessary for particle identification and full event reconstruction. The algorithm is verified with MC data, a future use to reconstruct measured data is scheduled. Various preparatory analyses are treated leading to the final analysis of the two most important reaction channels. Cut sequences are developed with the aid of Monte Carlo truth to ensure a high level of purity of the reaction signal.

Zusammenfassung

Die Teilchentherapie ist eine Behandlungsmethode gegen Krebs bei der Protonen und schwere Ionen benutzt werden, um die Tumorregion zu bestrahlen. In der Teilchentherapie ist eine genaue Berechnung der eingestrahlten Energiedosis im Gewebe durch ein Behandlungsplanungsprogramm unabdingbar, um eine präzise Bestrahlung eines Tumors zu gewährleisten. Höchste Genauigkeit wird durch den Einsatz von Monte-Carlo-Methoden erreicht, die neben der elektromagnetischen Wechselwirkung auch nukleare Wechselwirkungen berücksichtigen. Aufgrund des hohen Rechenaufwands werden sie jedoch noch nicht routinemäßig im klinischen Alltag zur Behandlungsplanung eingesetzt. Das Simulations-Toolkit Geant4 ist eine vielversprechende Monte-Carlo-Plattform, da es sämtliche physikalischen Prozesse berücksichtigt. Für den in der Medizinphysik relevanten Energiebereich muss dieses Toolkit jedoch noch validiert werden. Einige Wirkungsquerschnitte sind noch unzureichend bekannt, weshalb neue und genauere Messungen erforderlich sind.

Aus diesem Grund wird am III. Physikalischen Institut B der RWTH Aachen ein Flugzeitspektrometer entwickelt und mit Hilfe von Geant4 simuliert. Ziel des Experimentes ist es, durch den Beschuss eines Polyethylentargets mit Kohlenstoffionen der Energie 2280 MeV und dem Nachweis der dabei entstehenden Targetfragmente, nukleare Wechselwirkungsquerschnitte für die in der Teilchentherapie am häufigsten auftretenden Reaktionskanäle zu bestimmen.

Die vorliegende Dissertation behandelt die Geant4-Simulation des Flugzeitsprektometers zur Bestimmung der Targetfragmente. In diesem Kontext wird die Simulation in der Planungsphase des Detektors eingesetzt, um das Detektionskonzept zu evaluieren. Darüber hinaus werden die Auswirkungen der Targetdicke und unterschiedlicher Detektorsysteme und -größen auf die Messgrößen untersucht. In einem zweiten Teil stellt diese Arbeit den in ihrem Rahmen entwickelten Algorithmus vor, der die für die Fragmentidentifikation relevanten kinematisch Variablen rekonstruiert. Der Alogrithmus wird mit Hilfe der Monte-Carlo-Daten verifiziert, eine spätere Benutzung mit experimentellen Daten ist vorgesehen. Es werden diverse Rekonstruktionsszenarien vorgestellt, die auf die finale Analyse der beiden wichtigsten Reaktionskanäle führen. Mithilfe der Monte-Carlo-Wahrheit werden Schnittfolgen entwickelt, um eine möglichst hohe Reinheit des Reaktionssignals zu gewährleisten.

Contents

List of Figures

List of Tables

Chapter 1

Introduction

Cancer is the second most frequent cause of death in the European Union (EU) after cardiovascular diseases causing 29 % of deaths for men and 23 % for women. In 2008, 2.44 million people were diagnosed with cancer in the EU [Fer+10]. These numbers are expected to rise due to the ageing of the European population, because many cancer diseases occur more frequently among older people.

Nevertheless, the relative five-year survival rates improved significantly since the 1980's to 59 % for men and 64 % for women [RG12], due to great advances made in research and treatment. Radiation therapy is one cancer treatment modality and dates back to 1895, where German physicist Wilhelm Conrad Röntgen discovered a new kind of radiation which he called X-rays. One year later, the first therapeutic application of this new kind of radiation took place [Sau10]. Since then much progress has been made in fields such as physics, mathematics, computer science and radiation biology and radiation therapy evolved from an empirical and qualitative discipline to a scientific and precise clinical technology [SBG06].

In general, one distinguishes between brachytherapy (*brachys*: Greek, meaning "short distance") and teletherapy (*tele*: Greek, meaning "distant"). In brachytherapy, radioactive seeds are placed in or near the tumor itself, whereas in teletherapy, an external source of radiation is pointed at the tumor region inside the patient. In both cases, the primary aim is to deliver a lethal dose to the tumor cells while sparing healthy tissue.

Nowadays, photon beams with energies up to 25 MeV are most widely used for tumor irradiation. A disadvantage of this treatment modality is the dose deposition, which decreases exponentially after an initial maximum located a few centimeters under the skin and thus an irradiation of deap-seated tumor sites is difficult to achieve. Therefore, complex radiation fields with different entrance channels, energies and intensities are used in modern Intensity Modulated Radiotherapy (IMRT). However,

the unwanted dose in healthy tissue is not reduced, but rather distributed over a larger volume leading to tolerable damage [KV07].

A new approach is to use protons or heavy[1] ions instead, which offer great benefit compared to conventional radiotherapy. The maximum advantage is the improved depth dose deposition leading to the reduction of dose in normal tissue. At present, protons are used for particle therapy treatment in Germany at HZB in Berlin, RPTC in Munich and HIT in Heidelberg [PTC]. The therapy center in Heidelberg is the world's first heavy ion facility to make use of a 360° rotating beam delivery system [Hei].

Due to the characteristic sharp dose profile of protons and heavy ions, accurate calculation of the energy deposition in tissue by a treatment planning program is indispensable to ensure precise irradiation. Most programs used in daily clinical practice apply algorithms based on simplified models describing electromagnetic processes for the calculation of the target dose. During treatment with protons and heavy ions, nuclear reactions may occur additionally to electromagnetic interactions like ionization processes.

Highest accuracy in treatment planning is achieved with Monte Carlo (MC) methods taking nuclear interactions into account. However, these are not standardly implemented in clinical treatment planning systems today due to the need of high computing power. The simulation toolkit Geant4 originally developed for high-energy physics applications is a promising MC instrument, which still has to be validated for energy regions where particle therapy is applied.

Geant4 is a software library "for simulating the passage of particles through matter" [Ago+03] and organised in an object-oriented class hierarchy. Geant4 contains a large variety of alternative physics models the user may choose from. Due to its modular architecture, the implementation of new physics models and data sets is transparent and open to user validation.

The primary aim of the particle therapy project of the RWTH Aachen Physics Department is to perform new measurements of cross sections for possible reaction channels relevant to proton therapy, since certain cross section data sets show deficiencies and sparse data. The measured data is used to validate the Geant4 toolkit for the energy range where proton therapy is applied. These cross section sets have to be embedded into the Geant4 code to allow for a high predictive power necessary for accurate dose calculation in particle therapy. For that purpose, a time-of-flight (TOF) spectrometer has been designed and simulated within the Geant4 framework

[1] In radiation therapy, ions like ^{12}C are called heavy ions. In nuclear physics, however, these types of ions are considered to be light.

to detect target fragments originating from the nuclear interactions of interest.

The aim of this thesis is to simulate the TOF spectrometer within the context of Geant4 to evaluate the detection layout. Effects of diverse parameters like target thickness are investigated in the design phase of the current setup. Secondly, a reconstruction algorithm is developed to reconstruct the kinematic variables necessary for target fragment identification. This code is steadily checked against MC data and planned to be used for measured data of future beam times.

Chapter 2 provides an overview of the theoretical background relevant within the context of this thesis. The advantages of particle beams in contrast to conventional photon irradiation are discussed in chapter 3. Furthermore, the application of MC methods in particle therapy is demonstrated on two examples. Chapter 4 deals with the description of the detection concept and its implementation into a simulation framework using the Geant4 toolkit is subsequently introduced in chapter 5. The results of the detector simulation will be presented in chapter 6. Finally, the results of the identification of target fragments using the newly developed reconstruction algorithm are discussed in chapter 7.

Chapter 2

Theoretical background

The content of this chapter covers the theoretical background relevant to the scope of this thesis. In section 2.1, the definition of the cross section in particle physics is carried out. Section 2.2 deals with the nuclear models describing the properties of the nucleus. The different categories of nuclear reactions are addressed in section 2.3.

The physical dose plays a significant role in radiation therapy. Its definition is introduced in section 2.4. Furthermore, the particle loss of ion beams due to nuclear fragmentation leads to adjusted dose profiles, which is covered in section 2.5. In order to take the varying biological effects of different particle beams into account, the relative biological effectiveness is discussed in section 2.6.

The MC technique is introduced in section 2.7 and a general overview of the MC concept for the implementation of the transport of protons and ions is subsequently discussed in section 2.8. Because the MC toolkit Geant4 is used for the simulation of the TOF spectrometer, a brief overview is given in section 2.9.

In view of the final analysis of the two most important reaction channels, the definitions of purity and efficiency are established in section 2.10.

2.1 The cross section

In nuclear and particle physics, the cross section is used to express the probability of an interaction to occur between two particles. In fixed target experiments a particle flux per second j (s^{-1}) is typically focused on a target with a certain number of target particles per surface area n (m^{-2}) leading to a production rate N (s^{-1}). The total cross section is then given by

$$\sigma = \frac{N}{nj} \tag{2.1}$$

and has the dimension of a surface. In classical mechanics the geometric cross section can be used to describe reactions between two rigid bodies with radii R_1 and R_2. In case of an overlap of their projection surfaces $\pi {R_1}^2$ and $\pi {R_2}^2$, the geometrical cross section can be defined via

$$\sigma_{\text{geom}} = \pi \left({R_1}^2 + {R_2}^2 \right) \ . \tag{2.2}$$

When defined in this way, the more comfortable dimensional unit *barn* is often used to quantify a cross section: The surface area of nuclei with radii of about $10^{-14}\,\text{m} = 10^{-12}\,\text{cm}$ then amounts to[1] $\propto 1\,\text{b} = 1\,\text{barn} = 10^{-24}\,\text{cm}^2$.

In general, the integral total cross section in equation (2.1) is not accessible in experiments. Detectors often cover a limited solid angle $\mathrm{d}\Omega$, instead. The number of particles emitted into this solid angle at an angle of θ is then connected to the differential cross section via

$$\frac{\mathrm{d}\sigma(\theta)}{\mathrm{d}\Omega} = \frac{1}{nj} \frac{\mathrm{d}N(\theta)}{\mathrm{d}\Omega} \ . \tag{2.3}$$

In particle experiments the particle flux and the number of target particles per cm^2 are known, whereas the event rate into the solid angle $\mathrm{d}\Omega$ is measured. Therefore, the differential cross section can be obtained from experimental measurements.

So far, the energy dependence of the cross section was neglected. In addition to angular dependencies, nuclear reactions depend on energy as well. The double-differential cross section

$$\frac{\mathrm{d}^2\sigma(\theta, E)}{\mathrm{d}\Omega\,\mathrm{d}E} = \frac{1}{nj} \frac{\mathrm{d}^2N(\theta, E)}{\mathrm{d}\Omega\,\mathrm{d}E} \tag{2.4}$$

takes this circumstance into account.

2.2 Nuclear models

In nuclear physics, a uniform model to describe all phenomena in the atomic nucleus does not exist. Unlike for the atomic electron shell, where the forces on the shell electrons can be described by a simple central potential model, interactions between the multiple nucleons are much more complex. This being the case, different nuclear models exist that are more or less suitable for describing the problem at hand. In simplified models where only single-particle states in an average nuclear potential are considered, a number of properties of the atomic nucleus can be explained. Most

[1] The factor π is dropped here.

excited states of nuclear systems, however, may only be understood by assuming the interconnection of several nucleons or collective nuclear models. Two of the most important nuclear models shall now be presented in more detail.

2.2.1 The ideal Fermi gas

Within the scope of the Fermi gas model, first introduced by Fermi in 1926 [Fer26], the nuclear components are treated as identical and independent particles of a statistical ensemble. Because protons and neutrons are particles with spin $s = \frac{1}{2}\hbar$, they obey Fermi-Dirac statistics. By singling out one nucleon, its states can be determined by solving the corresponding Schrödinger equation in an averaged potential generated by all other nucleons. Many conclusions can be drawn with this simple model, e.g. the momentum distribution or binding energy of nucleons in the nuclear potential. The predictions become more accurate, the more nucleons are considered in the statistical ensemble.

The potential $V(r)$ considered in this model has the shape of a potential well. Within the nuclear radius R, it has a constant value before jumping to 0 at the edge of the potential well leading to

$$V(r) = \begin{cases} -V_0 & 0 \leq r \leq R \\ 0, & r > R \end{cases} \tag{2.5}$$

as shown in figure 2.1. The solution of the Schrödinger equation yields a set of energy eigenstates $E = E_x + E_y + E_z = \frac{\hbar^2\pi^2}{2ml^2}\left(n_x^2 + n_y^2 + n_z^2\right)$ characterised by quantum numbers n_x, n_y and n_z spanning the phase space $\mathrm{d}\Omega$, which is proportional to the number $\mathrm{d}n$ of possible states of a particle inside the momentum interval $\mathrm{d}p$:

$$\mathrm{d}n = \frac{1}{8}\mathrm{d}\Omega = \frac{l^3 p^2}{2\hbar^2\pi^2}\mathrm{d}p \ , \tag{2.6}$$

with l being the edge length of the potential well and m the mass of the particle [MK94]. The factor $\frac{1}{8}$ takes into account, that the positive quantum numbers only fill one octant of the phase space.

At a temperature of 0 K, all states below the Fermi energy E_F are occupied. At finite temperatures this Fermi limit becomes more and more indistinct and states above the Fermi energy may be occupied. Integrating equation (2.6) finally yields the Fermi energy

$$E_\mathrm{F} = \frac{1}{2m} 3^{2/3}\pi^{4/2}\hbar^2 \left(\frac{n}{l^3}\right)^{2/3} \ , \tag{2.7}$$

which can be determined with knowledge of the particle number density n/l^3. The volume l^3 of a nucleus can be approximated by $l^3 = \frac{4}{3}\pi r_0^2 A$ and n is simply given by the number of nucleons A leading to $E_\mathrm{F} \approx 30\,\mathrm{MeV}$.

2.2.2 The shell model

The predictions of the Fermi model are limited to global properties of a statistical ensemble of nucleons. Adjusting the average potential $V(r)$ to a more realistic scenario, as it is done in the shell model, one can understand individual nuclear properties like the high separation energies for nuclei with certain numbers of protons or neutrons, the so-called *magic* numbers.

Besides the potential well introduced in section 2.2.1, the potential of the harmonic oscillator is analytically solvable and another candidate for the nuclear potential. The more realistic *Woods–Saxon* potential

$$V_\mathrm{WS}(r) = -\frac{V_0}{1 + \exp\frac{r-R}{a}} \tag{2.8}$$

interpolates between both of them, see figure 2.1. The parameter a is a measure of the edge blurring.

Without further modifications the Woods–Saxon potential is not capable of explaining all magic numbers. By introducing the spin-orbit coupling of nuclei through

$$V(r) = V_\mathrm{WS}(r) + V_{ls}(r)(\boldsymbol{l} \cdot \boldsymbol{s}) \ , \tag{2.9}$$

this circumstance could be corrected [HJS49; GM49], where $\boldsymbol{l}$ is the orbital angular momentum, $\boldsymbol{s}$ the spin of the nucleon and $V_{ls}(r)$ a radial function. The strong spin-orbital coupling of nucleons causes a decisive shift of energy levels. The resulting energy gaps exactly arise at places where shell closures at magic numbers of protons or neutrons occur. A much weaker coupling in atomic physics is resulting in a similar phenomenon, namely the fine structure describing the splitting of spectral lines.

2.3 Categories of nuclear reactions

In what follows, the different types of nuclear reactions are treated in more detail. The listing below provides a general overview of the nuclear reaction categories to be discussed afterwards. Considering a projectile p impinging on a target particle T,

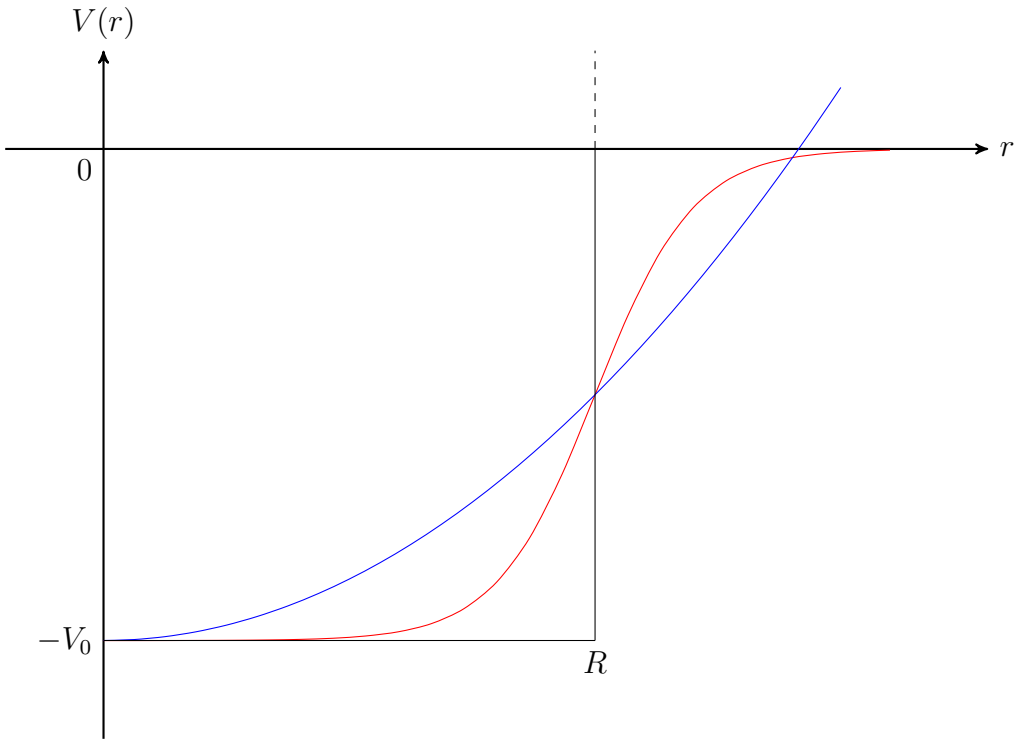

Fig. 2.1: Possible approaches to the nuclear potential: Potential well (black) with depth $-V_0$, harmonic oscillator (blue) and the Woods–Saxon potential with nuclear radius R (red).

the possible interaction channels may be roughly divided into

- elastic scattering of the projectile, where no inner degrees of freedom of the target are excited and the sum of kinetic energies stays constant:

$$\mathrm{p} + \mathrm{T} \rightarrow \mathrm{p} + \mathrm{T} \ ,$$

- inelastic scattering resulting in the excitation of the target nucleus and loss of kinetic energy of the projectile:

$$\mathrm{p} + \mathrm{T} \rightarrow \mathrm{p}' + \mathrm{T}^*$$

- and nuclear transformations, where totally new particles can emerge:

$$\begin{aligned} \mathrm{p} + \mathrm{T} &\rightarrow \mathrm{x}_1 + \mathrm{Y}_1 \\ \mathrm{p} + \mathrm{T} &\rightarrow \mathrm{x}_2 + \mathrm{Y}_2 \\ &\vdots \end{aligned}$$

2.3.1 Elastic and inelastic nuclear scattering

In elastic and inelastic scattering processes described above, particles p and T maintain their identity after the interaction process. In the case of inelastic scattering, kinetic energy of the projectile is transferred to a nucleon of the target material leaving an excited nucleus behind. The energy spectrum of the scattered projectiles provides insight into the structure and excitation spectrum of the target nucleus.

Nuclear scattering processes on a locally restricted scattering center are time-dependent problems, which can be broken down into a stationary context: Assuming a particle beam with a sharp energy distribution entering from the negative z-direction, Heisenbergs's uncertainty principle states a large extent of each particle's wave representation in z-direction. As a result, the wave package can be seen as stationary for short periods of time and the asymptotic pattern of the stationary scattering states can be derived [CTDL99].

For large negative times t the incoming particle effectively feels no potential $V(r)$ and its state can be characterised by a plane wave packet $e^{\mathrm{i}kz}$, where k is the z-component of the wave vector. Entering the scope of the potential, the structure of the wave packet will fundamentally be changed and the development in time gets complicated. The shape of the scattered wave packet will therefore depend on the form and impact of the underlying potential. Again, the asymptotic behaviour for large times t (far away from the scope of the potential) can be derived to $e^{\mathrm{i}kr}/r$ [CTDL99]. In this perspective a spheric wave emanates from the scattering center. In general, the scattering is not isotropic and the information of the angular dependencies is contained in the amplitude leading to the total wave function

$$\psi(\boldsymbol{r}) \overset{r\to\infty}{=} A\left(e^{\mathrm{i}kz} + f(\theta)\frac{e^{\mathrm{i}kr}}{r}\right) \ . \tag{2.10}$$

The amplitude of the incoming particle wave is denoted by A and serves the purpose of normalization. In equation (2.10), only the so-called *scattering amplitude* $f(\theta)$ is dependent on the potential $V(r)$. Involving the incoming and outgoing current densities, one can extract the important relationship for scattering phenomena

$$\left(\frac{\mathrm{d}\sigma(\theta)}{\mathrm{d}\Omega}\right) = |f(\theta)|^2 \tag{2.11}$$

showing that the differential cross section is completely determined by the scattering amplitudes $f(\theta)$ [CTDL99].

2.3.2 Nuclear transformations

In nuclear transformation processes, the collision of projectile and target particles leads to a redistribution of nucleons and hence to completely different particles in the output channel. A differentiation is made between reactions taking place on the surfaces of colliding particles, called *direct reactions* and reactions proceeding over the formation of a temporary *compound nucleus*. Particularly strong energy dependencies of cross sections lead to the formation of *resonance* structures.

Direct reactions

Nuclear reaction processes lasting approximately the time a nucleon takes to traverse a nucleus ($t \approx 10^{-22}\,\mathrm{s}$) are called direct reactions. In this brief period of time, the projectile's energy cannot be distributed among all target nucleons, so that only a small number of nucleons interact with the projectile.

Typical examples are reactions that add nucleons to (*pickup*) or remove (*strip*) nucleons from the projectile nucleus or the absorption of the projectile and subsequent emission (*kickoff*) of nucleons. Reaction types of these forms are sometimes called transfer reactions. Examples of stripping reactions can be found in deuteron-induced reactions like

$$\begin{aligned} \mathrm{d} + {}^{\mathrm{A}}\mathrm{Z} &\rightarrow \mathrm{p} + {}^{\mathrm{A+1}}\mathrm{Z} \\ \mathrm{d} + {}^{\mathrm{A}}\mathrm{Z} &\rightarrow \mathrm{n} + {}^{\mathrm{A+1}}(\mathrm{Z}+1)\ . \end{aligned}$$

In the reverse reaction channel (pickup reaction) one target nucleon might be absorbed by the projectile:

$$\begin{aligned} \mathrm{p} + {}^{\mathrm{A}}\mathrm{Z} &\rightarrow \mathrm{d} + {}^{\mathrm{A-1}}\mathrm{Z} \\ \mathrm{n} + {}^{\mathrm{A}}\mathrm{Z} &\rightarrow \mathrm{d} + {}^{\mathrm{A-1}}(\mathrm{Z}-1)\ . \end{aligned}$$

Processes are called kickoff reactions when the projectile remains in the target nucleus, but a nucleon is emitted posterior, e.g. in

$$\mathrm{p} + {}^{\mathrm{A}}\mathrm{Z} \rightarrow \mathrm{n} + {}^{\mathrm{A}}(\mathrm{Z}+1)\ .$$

This reaction type can be distinguished from inelastic reactions only if the projectile differs from the ejectile. For heavier projectiles than protons or neutrons, even groups of nucleons like alpha particles can be exchanged in so-called cluster transfer reactions

[BWW07].

Characteristic observation variables in direct reactions are angular distributions and absolute cross sections. Due to the fact that the projectile nearly keeps its direction of motion, the angular distributions are not symmetric but peaked in forward direction. Because lifetime and energy uncertainty are linked via Heisenberg's uncertainty principle $\Delta E \Delta t \geq \frac{\hbar}{2}$, cross sections of direct reactions will change slowly with energy [MK94].

Resonances

The strongest energy dependencies of cross sections arise in resonance reactions leading to the formation of local maxima. Resonances may occur when a particle inside a nucleus accumulates more energy than its binding energy ($E > 0$) and enters the domain of unbound states. In contrast to bound states, the particle's wave function does not disappear outside the nucleus, which means that the potential border may be passed leading to capture or emission of a particle. Instead, boundary conditions ensure that the wave function inside the nucleus continuously merges into a wave function in the outdoor space.

In this context, the gradient of the wave function amplitude at the border of the nucleus describes the probability of traversing the nucleus margin. The probability of moving into or out of the nucleus becomes largest when the amplitudes inside and outside the nucleus are equal [MK94]. An example of strong energy dependence of cross sections can be found in the reaction ^{238}U(n, γ)^{239}U shown in figure 2.2.

The width of the resonance structure Γ_{reso} depends on the intensity of the gradient variation when slightly changing the energy of the particle. In the case of strong energy dependence, the width of the resonance will be small. Additionally, the resonance width Γ_{reso} gets broadened when the particle loses energy inside the nucleus through interactions with other nucleons or gamma transitions between nuclear states. Hence, the total width

$$\Gamma_{\text{tot}} = \Gamma_{\text{reso}} + \Gamma_{\text{reac}} \ , \tag{2.12}$$

is composed of the *resonance* width Γ_{reso} and the so-called *reaction* width Γ_{reac}.

A quantitative description of the resonance structure can be drawn within the scattering formalism leading to the resonance cross section named after Gregory

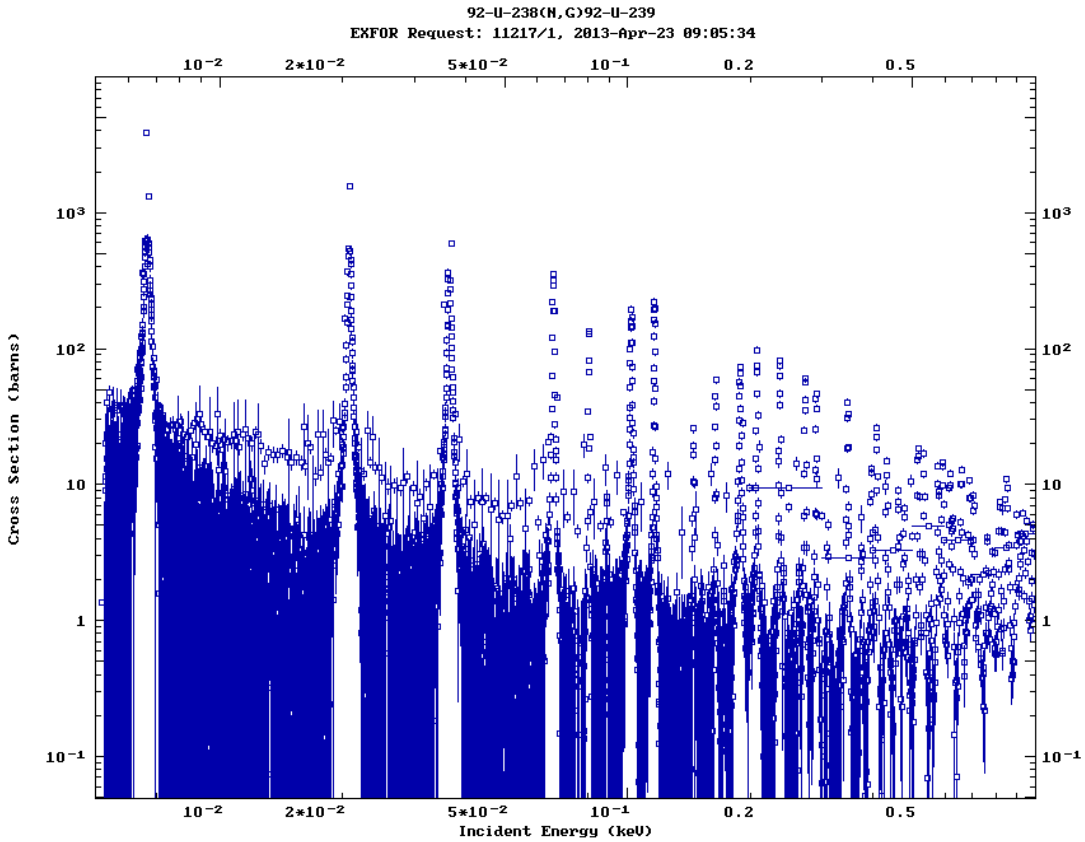

Fig. 2.2: Total cross section for neutron capture of ^{238}U leading to the reaction $^{238}\mathrm{U}(n,\gamma)^{239}\mathrm{U}$. Data retrieved from EXFOR database [Exf].

Breit and Eugene Wigner:

$$\sigma_{\mathrm{reso}} = \frac{\pi}{k^2} \frac{\Gamma_{\mathrm{reso}}^2}{\left(E - E_{\mathrm{reso}}\right)^2 + \frac{1}{4}\Gamma_{\mathrm{tot}}^2} \ , \tag{2.13}$$

where k and E are wave number and energy of the projectile [MK94]. The width of the cross section defined in equation (2.13) at half of the maximum value corresponds to Γ_{tot}.

In deriving equation (2.13), it was assumed that only one resonance state contributes to the cross section and nucleons were described by single-particle states neglecting their interaction. This situation leads to total widths Γ_{tot} of the order of 1 MeV [MK94], whereas the widths observed in experiments, however, are much smaller. Taking the pairwise interactions into account leads to more complicated configurations of wave functions and thus to a splitting of energy levels. Hence, the gradient mentioned above is more sensitive to energy variations leading to much smaller widths in the case of compound nuclei, where pairwise nucleon interactions

are taken into account.

Compound nucleus reactions

It may also happen that the projectile remains in the target nucleus after the first interaction process. Further collisions will lead to thermal equilibrium inside the nucleus. An intermediate system created in this way is called *compound nucleus*.

In a statistical process the excitation energy of the compound nucleus will be equally distributed among all nucleons most of the time, until one particle has accumulated enough energy to escape. This process can take considerably longer (up to $t \approx 10^{-16}\,\mathrm{s}$ [MK94]) than the direct reactions mentioned above leading to a strong dependency of compound cross sections on energy. One might therefore expect sharp resonances only in compound nuclear reactions.

The long lifetime of compound nuclear systems led to the idea that the formation and decay of the compound nucleus are independent [Boh36]:

$$\mathrm{p} + \mathrm{T} \underset{\text{formation}}{\rightarrow} \mathrm{C}^* \underset{\text{decay}}{\rightarrow} \mathrm{b} + \mathrm{Y}$$

with C^* denoting the excited compound nucleus. This implies that the cross section may be expressed as

$$\sigma_{\alpha\beta} = \sigma_{\alpha\mathrm{c}}(E_i) \cdot P_\beta \ , \tag{2.14}$$

where $\sigma_{\alpha\mathrm{c}}(E_i)$ is the cross section for the compound nucleus formation with excitation energy E_i and P_β the probability for the compound nucleus decay into the channel β. This probability can be connected to the decay width Γ via

$$P_\beta = \frac{\Gamma_\beta}{\Gamma} \quad \text{with} \quad \Gamma = \sum_{\beta'} \Gamma_{\beta'} \ . \tag{2.15}$$

The compound nucleus possesses a vast range of varieties of distributing its excitation energy on the residual nucleus and the emitted particle after decay. To gain qualitative statements on the strong energy dependence of the cross section $\sigma_{\alpha\mathrm{c}}(E_i)$, the energy spectra of emitted particles have to be investigated.

In figure 2.3 the energy levels of the compound nucleus, the residual nucleus and the emitted particle are shown. The excitation energies of the compound nucleus and residual nucleus shall be denoted as E_C and E_Y, respectively. E_b labels the kinetic energy of the emitted particle. For large kinetic energies E_b, one observes resonance structures in the energy spectrum of emitted particles corresponding to discrete excitation energies of the residual nucleus. The decay width Γ of these

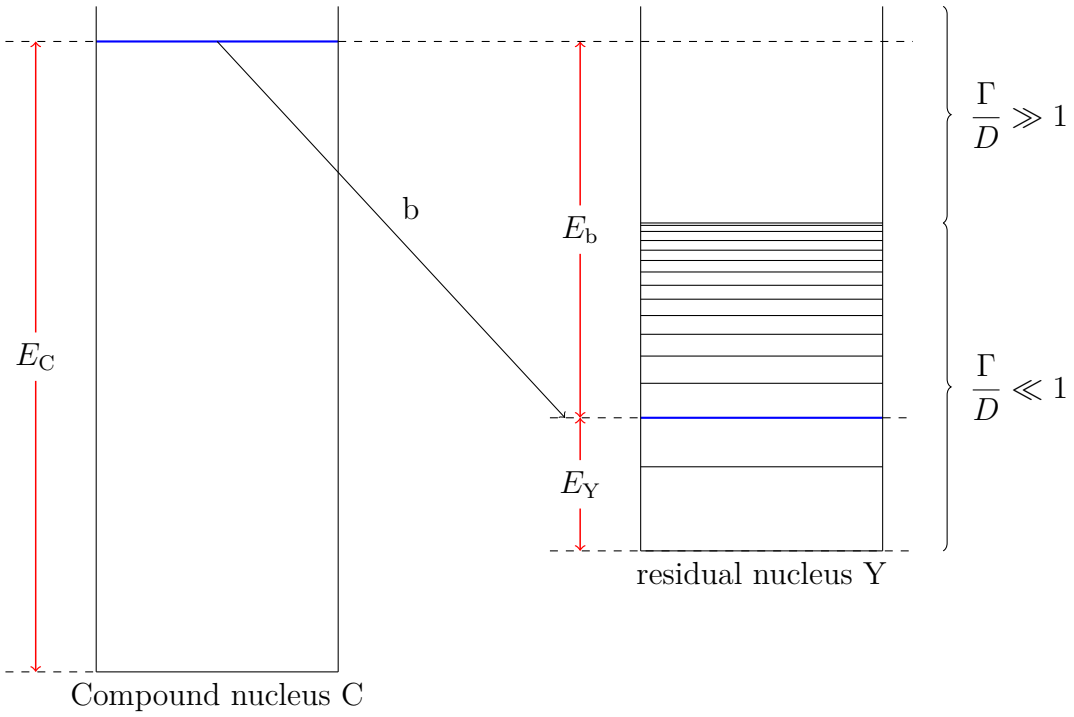

Fig. 2.3: Relations of energies for the decay of a compound nucleus C into a residual nucleus Y and under emission of a particle b. Adapted for own purposes from [MK94].

energy levels is small compared to the average distance D between neighbouring energy levels: $\frac{\Gamma}{D} \ll 1$.

For higher excitation energies E_Y, the distance D between energy levels gets smaller, while simultaneously the width of these levels broadens. Finally, the average spacing D becomes smaller than the level width Γ and states start to overlap: $\frac{\Gamma}{D} \gg 1$. This being the case, resonant structures are no longer observable.

A quantitative treatment of the emission spectra may take place within the framework of a statistical model of nuclear reactions answering the question of how many possibilities exist to distribute the energy among all nucleons. An illustrating example of this situation is that of a jar containing balls flying back and forth and possibly knock against each other. For escaping the jar, one of the balls has to unite a substantial part ϵ of the summed energy of all balls. The number of possibilities of distributing the remaining energy $E_\mathrm{total} - \epsilon$ among the remaining $N - 1$ nucleons divided by the number of possibilities of distributing the energy E_total among all balls N yields the probability of finding such a particle. In the scope of the nuclear statistical model one has to find an expression for the level density as a measure for the probability of distributing the energy ϵ on A nucleons. In addition, the probability

to cross the potential border has to be taken into account.

The total cross section for the transition from initial state α into the final channel β with an emission energy ϵ_β can finally be derived to

$$\sigma_{\alpha\beta} = \sigma_{\alpha c}(E_i) \cdot \frac{W_{c\beta}\epsilon_\beta}{\sum_\beta \int W_{c\beta}(\epsilon)\mathrm{d}\epsilon} \ , \tag{2.16}$$

which is known as the *Weißkopf–Ewing formula* [WE40].

2.4 Physical dose

The absorbed physical dose D ([D] = *Gray* (Gy) = J/kg) is of major importance in radiation therapy as it describes the energy deposition in tissue. It was defined by the International Commission on Radiological Units and Measurements (ICRU) as the quotient of energy loss de deposited in a mass element dm due to ionizing radiation [II93]:

$$D = \frac{\mathrm{d}e}{\mathrm{d}m} \ . \tag{2.17}$$

2.5 Range of nuclear fragments

The energy loss of particles described in the previous section is mainly due to ionization processes via electromagnetic interaction. However, during the passage of particles through matter a small amount of primary particles undergoes a nuclear reaction leading to a number of secondary fragments. Particle beams of heavy ions lose a greater amount of their primary particles than lighter ones. For protons, 1.5 % of primary particles are lost per centimeter, whereas for carbon (3.0 %) or argon (5.0 %) this rate increases [Raj+78].

Since peripheral collisions are the most common reactions, the primary particle loses only one or a small number of nucleons [Ser47]. The corresponding projectile fragments move with nearly the same velocity as the primary particle at the collision point [Hüf85] and their range is given by [Fie+06]

$$R_\mathrm{f} = R_\mathrm{p} \frac{A_\mathrm{f}/Z_\mathrm{f}^2}{A_\mathrm{p}/Z_\mathrm{p}^2} \tag{2.18}$$

with R_p being the initial primary range and A_p and Z_p the atomic mass and atomic number of the primary particle. A_f and Z_f are the corresponding quantities for

the fragment. As can be seen from equation (2.18), projectile fragments with smaller ratios A/Z^2 than the primary particle feature a shorter range. Fragments with higher ratios will stop behind the primary stopping position leading to a dose tail in the depth-dose curve (see dose profile of carbon in figure 3.1).

2.6 Relative biological effectiveness

In cell survival experiments the effect of X-ray and particle radiation can be investigated. The surviving fraction $S(D)$ of cells is usually approximated by an equation of the form

$$S(D) = S_0 e^{-\left(\alpha D + \beta D^2\right)} \ , \tag{2.19}$$

where D is the absorbed dose and α and β are experimentally determined coefficients characterizing the radiation response. The parameter α is a measure for the linear part of the cell survival occurring at small doses, whereas the quadratic part is described by the parameter β yielding the influence of repair at higher doses. The quotient $\frac{\alpha}{\beta}$ finally describes the repair capacity of the cell and hence is an important quantity in evaluating the effect of radiation therapy [Fow89].

In order to take the different biological effects of different radiation into account, the *relative biological effectiveness* (RBE) was introduced:

$$\mathrm{RBE}_{\mathrm{test}} = \frac{D_{\mathrm{ref}}}{D_{\mathrm{test}}} \ , \tag{2.20}$$

which relates the energy dose of the test radiation D_{test} to the energy dose of a reference radiation D_{ref} (most often X-rays) to produce the same biological effect under the same conditions. This means in particular that the RBE determines the photon-equivalent dose by multiplication with the absorbed physical dose.

2.7 The Monte Carlo technique

The history of modern MC techniques dates back into the 1940s, when physicists like Fermi, Ulam, von Neumann and Metropolis realized to examine physical problems, especially properties of radioactive nuclei, from a stochastic perspective at Los Alamos National Laboratory. Even before the availability of modern (electronic) computers, first efforts were made, for example by using analog computers like the FERMIAC invented by Fermi for studies in neutron transport. A good survey of these very early applications can be found in [Met87] written by Metropolis.

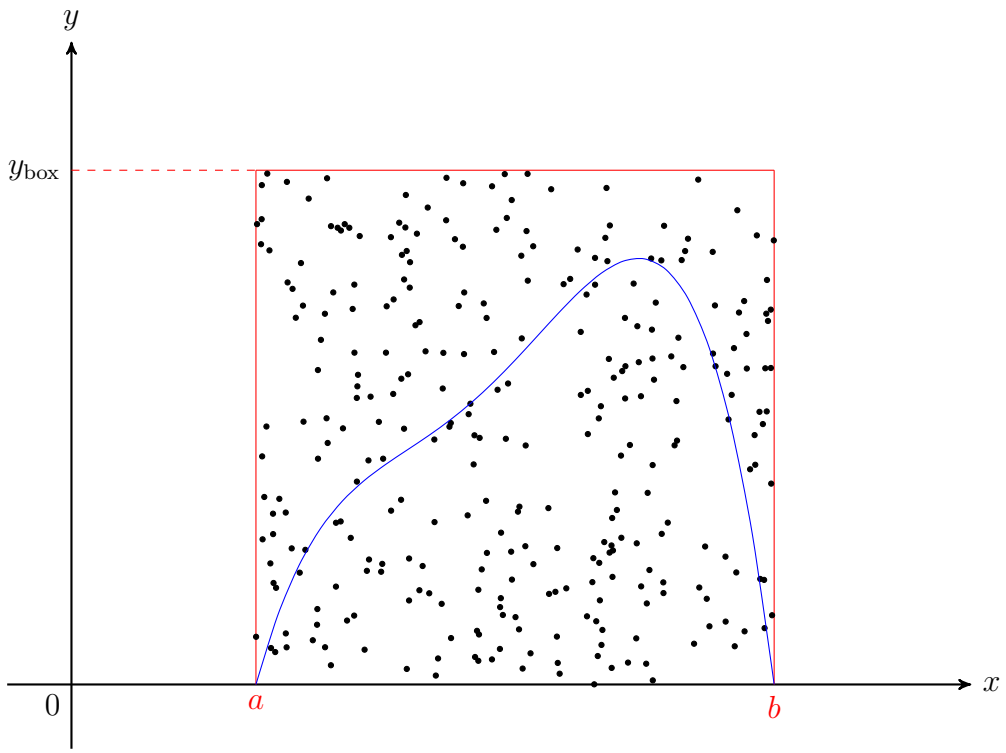

Fig. 2.4: Schematic representation of the "hit-or-miss" method for evaluating the integral of the function $f(x)$ (blue curve). A number of points is randomly sampled within the area denoted by the red box.

MC methods, in contrast to analytical or numerical strategies, use repeated random sampling on a pre-determined probability distribution law to approximate a specific measure. One of the simplest examples is the evaluation of definite integrals

$$y = \int_a^b f(x)\,\mathrm{d}x \ , \tag{2.21}$$

which cannot be solved analytically. In this case a box is defined ranging from $x = a$ to $x = b$ and from $y = 0$ to $y = y_{\text{box}}$ with $y_{\text{box}} > f(x)$, as shown in figure 2.4. Then a number N of random numbers are drawn uniformly within the area of the box and the number N_0 of points with $y_{N_i} < f(x)$ is stored. An approximation to the integral is then given by:

$$y \approx y_{\text{approx}} = \frac{N_0}{N}\left[y_{\text{box}}(b-a)\right] \ . \tag{2.22}$$

Increasingly accurate results are achieved the more often the MC experiment is repeated and since the result is an average, it is associated with a statistical uncertainty decreasing as $\propto 1/\sqrt{N}$. In addition, further factors have to be taken into account in order to gain useful simulation results, which were summarised by Sawilowsky

[Saw03]:

- the (pseudo-random) number generator has a long period before the sequence repeats,
- the (pseudo-random) number generator produces values that pass tests for randomness,
- the proper sampling technique is used,
- the algorithm used is valid for what is being modelled and
- the MC code simulates the phenomenon in question.

It is obvious that the outcome of the MC simulation is heavily dependent on the efficient production of random number streams. The usage of physical processes like radioactive decay or white noise generation in electrical circuits to produce random numbers is impractical and the creation of new numbers is too slow to be relevant for modern MC experiments. Computer algorithms to produce random numbers are deterministic, because they produce a periodic sequence of numbers. To obtain numbers that are effectively random (called pseudo-random) only a small subset of a single period has to be used. For example, the generator TRandom3 implemented in the data analysis framework ROOT, based on the Mersenne twister algorithm [MN98], has a period of $2^{19937}-1$ and is the recommended one by the ROOT authors [The].

The MC technique unfolds its full potential in multi-dimensional problems, where the time to solve the problem with alternative approaches may grow exponentially with the number of dimensions. An integration in ten-dimensional space using 20 integration points in each dimension leads to an overall number of integration points of $20^{10} \approx 10^{13}$, which cannot be handled by modern quad-core processors in less than a couple of hours. Metropolis and Ulam suggested to use a statistical approach, the MC method, to avoid this "curse of dimensionality" [MU49] by taking, for example, 10^4 integration points at random and use only those to evaluate the integral. Applying the ergodic theorem, the thus obtained estimate should approximate the real value with great accuracy.

The basic and more or less graphic examples given in this section are not able to show the outreach of the MC technique into other scientific or non-scientific fields of study. It has pretty much become one of the standard tools for example in lattice gauge theories like quantum chromodynamics (QCD), fluid dynamics or non-equilibrium and irreversible processes like crystal growth or growth of structures and patterns. But also research areas like sociophysics, finance and medicine profit from MC evaluations.

2.8 Proton and ion transport and interaction

In many MC codes, the transport of particles is simulated by discretizing the trajectory of a particle into a series of small steps between two interaction sites. Protons or heavy ions and secondary particles are tracked in a statistical sense as they interact with the material through which they pass. This way, each process associated to a particle proposes a step length after which the next interaction would statistically occur and the shortest one is taken and the interaction invoked (see figure 2.5).

The physics of particle interactions are modeled using theoretical models or experimental cross section data for electromagnetic and nuclear interactions stored in interaction data tables. These include interaction probabilities for each interaction and for each type of element of the target material.

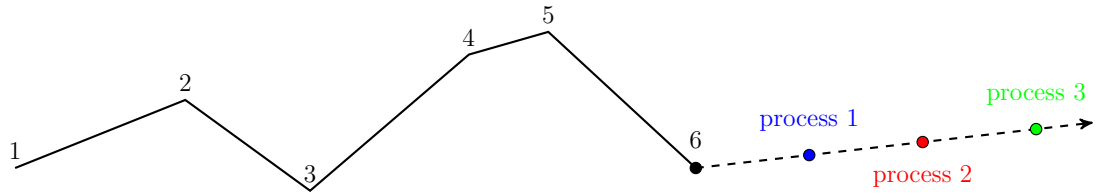

Fig. 2.5: Schematic representation of a snapshot of a particles trajectory consisting of several steps and the current position ● of the particle. Each step is terminated by a process with the smallest step length sampled. In this example process 1 will be triggered next.

2.9 The Geant4 toolkit

Before describing the Geant4 toolkit in section 2.9.2 to 2.9.4, a short overview over the most frequently used MC codes in particle therapy is given in section 2.9.1.

2.9.1 MC codes used in particle therapy

MCNPX ("**M**onte **C**arlo **N**-**P**article e**X**tended") [Wat02] is a general purpose MC transport code developed at Los Alamos National Laboratory and represents a major extension to the original *MCNP* code to nearly all particles and all energies. In contrast to Geant4, the use of MCNPX does not require programming skills. All user input is defined in an ASCII input file defining the geometry, physics classes, the particle source and even the use of variance reduction techniques.

FLUKA ("**FLU**ktuierende **KA**skade") [Fer+05] is another general purpose MC toolkit for simulating particle transport and interaction with matter. Claiming that the implementation of accurate and modern physics models has highest priority,

results are tested against experimental data at each interaction and conservation laws are enforced on each step. About 60 different particles can be simulated, including polarized and optical photons. As with MCNPX, FLUKA does not require any programming skills to set up an application. Instead, FLUKA reads an ASCII input file with a number of commands and options.

SHIELD-HIT ("SHIELD-**H**eavy **I**on **T**herapy") [Bas+12] is the medical version of the SHIELD transport code. It is designed for the precise simulation of therapeutic beams of protons and heavy ions used in particle therapy. Energy loss of charged hadrons are computed according to the Bethe formula. The nuclear interaction models were developed at JINR (Joint Institute for Nuclear Research), Dubna and INR RAS (Institute for Nuclear Research of the Russian Academy of Sciences), Moscow and are grouped together in the MSDM-generator. Like MCNPX and FLUKA, SHIELD-HIT uses input files in order to define material compositions, beam parameters and geometries.

2.9.2 Philosophy of Geant4

Geant4 ("**GEO**metry **AN**d **T**racking") [Ago+03] is a MC toolkit simulating the passage of particles and their interactions with matter. The code is written in C++ programming language and provides a complete range of functionality organised in separate and independent classes each maintained by a working group of experts.

The origin of the development of Geant4 can be found in two studies carried out at CERN and KEK in 1993, which proposed to improve the Geant3 code for the next generation of high energy physics experiments. Both activities merged and research and development of the resulting project was finished in 1998 with the first release of the new Geant4 code [Ago+03].

The development of Geant4 was driven by the software needs of modern particle and nuclear physics experiments. As these experiments become increasingly complex and the corresponding detectors greater in size and better in sensitivity, a robust and hierarchical software framework needs to be implemented. As stated above, the modularity of Geant4 ensures high flexibility, so that specific components can be used by other components through well-defined interfaces. The implementation of physics should be "transparent and open to user validation" [Ago+03], so that physics models and data can be added or customized and the user can decide which models to be used in his own simulation. These considerations led to the present design concept of Geant4 with its underlying hierarchical structure based on the Booch methodology [Boo04], which shall be discussed in the next section.

2.9.3 Structure of Geant4

The classes of the Geant4 code are divided into 17 major categories associated in linear and unidirectional dependency, as shown in figure 2.6. Bottom categories are used by the ones listed higher in the diagram and each category holds a number of classes within its context. The description of each category follows the remarks made in [Ago+03].

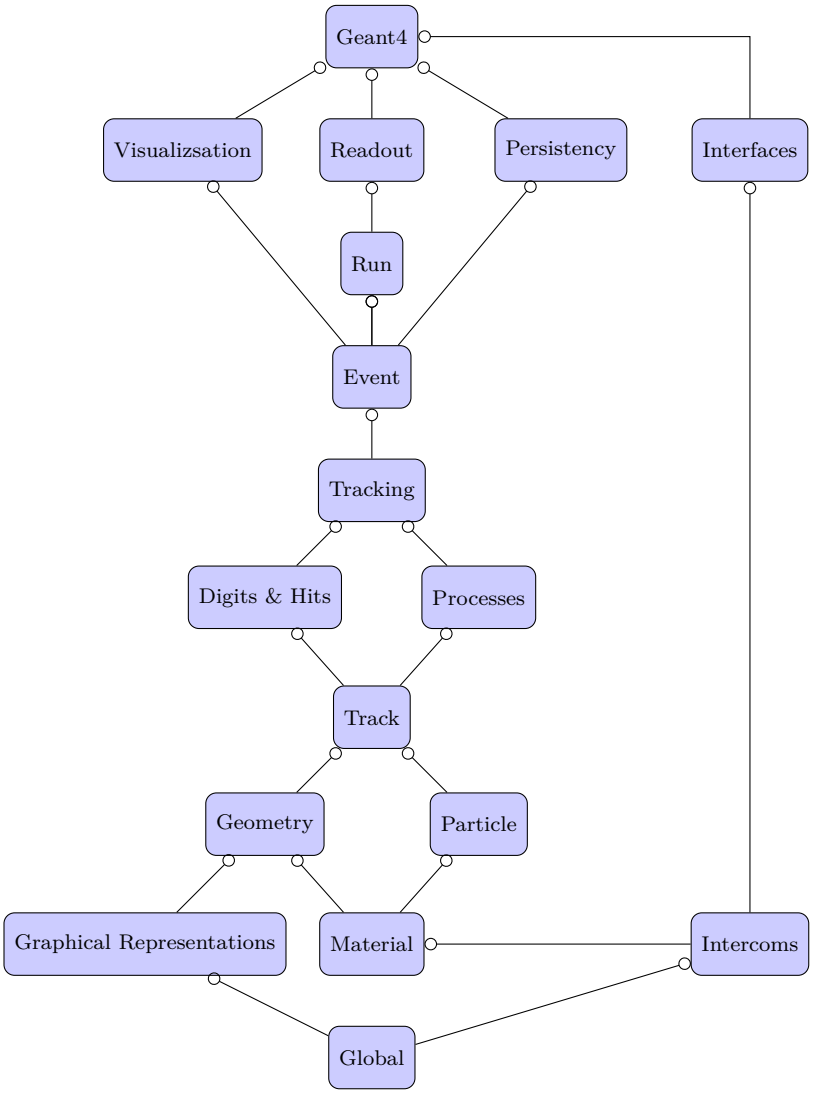

Fig. 2.6: Category diagram of Geant4. Lines with an open circle symbol ○—— denotes a *using* relationship. Categories at the circle end uses the adjoint category.

1. Global The category *Global* at the very bottom of the diagram contains classes, types, structures and constants, which are of general use within the Geant4 frame-

work. This includes the system of units, the basic types like `G4int`[2] or random number generator routines.

2. Graphical Representation *Graphical Representation* classes define the visualization attributes of detector components, i.e. the visualization styles (wireframe or solid surfaces) and colours of detector surfaces.

3. Material Materials are defined in the *Material* category classes. The user may construct materials out of several chemical elements, which have to be defined before material construction. It is also possible to have correct isotope composition by composing elements out of a single isotope or a mixture of isotopes. When using optical photons in Geant4, the material category also provides capabilities of describing the properties of optical surfaces, like surface roughness of finish.

4. Intercoms The *Intercoms* category enables the user to communicate and interact with specific components of a Geant4 application without affecting the dependencies of other classes. User commands can be applied in an interactive session, in batch mode via macro file(s) or hard coded C++ calls.

5. Geometry The *Geometry* category provides the ability to set up a geometrical structure by describing a hierarchy of different volumes. The concept of solids enables the user to define the shape of a component ranging from simple basic shapes like boxes, spheres or cylinders to solids composed of different shapes joined together by boolean operations. For medical purposes it is possible to build a geometry based on CT data from DICOM ("Digital Imaging and Communications in Medicine") images. Once the solid is defined, it can be linked to a logical volume representing a volume of a certain shape made of a certain material. A logical volume can hold other attributes (like visualization attributes) or daughter volumes, but is independent of the physical position. After defining the logical volume, a physical volume can be created, which is a placed instance of the volume and incorporates all attributes.

6. Particle Particles are defined in a *Particle* category class, namely `G4ParticleDefinition`. It describes the basic properties of particles like mass, charge or spin.

[2]The Geant4 basic types are simple typedefs to the types defined in the Standard Template Library (STL) of C++.

7. Track Current attributes of particles during the simulation (kinetic energy, momentum, position, etc.) are kept in classes of the *Track* category.

8. Digits & Hits Especially for larger detection setups simulated in Geant4, it is useful to introduce sensitive detectors, which can be linked to logical volumes. Each time a track traverses a sensitive volume, a hit is produced which is a "snapshot of a physical interaction or an accumulation of interactions of a track" [Gea12]. A digitization (short: digit) can be used to simulate the read-out of the detector signal and thus is created from the hit collection in that specific detector part. The corresponding category is therefore called *Digits & Hits*.

9. Processes The *Process* category uses particle information of the track category to calculate a step length for a given process.

10. Tracking The *Tracking* category finally steers the invocation of the process which proposed the shortest step length (see section 2.8 and figure 2.5) and tracks the particle step by step until the track is finished.

11. Event An event is the main unit of a Geant4 simulation and consists of the track of the primary particle and the tracks of all particles created during its evolution in the detector, by decay, scattering or any other kind of process.

12. Run The collection of events within a run which share a common beam and detector setup is finally managed by the *Run* category.

13. Visualization It is possible to display the detector geometry and particle trajectories during or after a Geant4 run. The *Visualization* category offers classes to provide a variety of user requirements like detector debugging, surveying of events or high-quality output for presentations and theses. Different visualization drivers can be selected to satisfy the users purposes.

14. Readout In some cases it is useful to define a *Readout* geometry, which can be different from the geometrical representation. For example, if one is interested in the energy depositions within specific cells or layers of a sandwich calorimeter,

15. Persistency the *Persistency* category offers an interface for saving run, event, hits, digits and geometry information and retrieve them in post-simulation processes. Typically, C++ (transient) objects are deleted from the heap when the application is terminated. In order to use this functionality, the user has to set environment variables before installing the Geant4 toolkit. Suitable objects can then be passed to the `G4PersistencyManager` which creates persistent objects in a special database.

16. Interfaces Closely related to the Intercoms category is the *Interfaces* category, which offers concrete graphical or non-graphical user interfaces to steer the simulation. These interfaces are created in the `main()` function and should be chosen according to the users computer environment. The class `G4UIterminal`, for example, opens a session on a command-line terminal for user input.

17. Geant4 The topmost category *Geant4* does not mean any actual piece of code of the Geant4 toolkit. It can be rather understood as an indication that everything below is specific Geant4 code separated from the user classes (e.g. the `main` function).

2.9.4 Structure of an application

Mandatory classes

There are three mandatory classes the user has to implement to set up a Geant4 application, which cover the most important features of a detector simulation:

1. The properties of the primary beam particles are defined in the user's *PrimaryGeneratorAction* class,
2. the creation and positioning of all volumes forming the simulation geometry is accomplished in the *UserDetectorConstruction* class and
3. the selection of physics models and processes used in the simulation is done in the *UserPhysicsList*.

Because Geant4 does not provide default behavior for these classes, they have to be derived from the abstract base classes provided by Geant4: `G4VUserDetector-Construction`, `G4VUserPhysicsList` and `G4VUserPrimaryGeneratorAction`.

PrimaryGeneratorAction The initial parameters of the primary particles are given in this class. Here, the user defines the particle type, its initial energy, position and momentum direction. Rather than giving fixed values, distributions may be used

to describe one or more of the quantities mentioned above. At the beginning of each event the method `GeneratePrimaries()` is invoked to produce a new primary vertex.

DetectorConstruction The properties of the detector are described in terms of geometries and materials. As described in section 2.9.3, a detector geometry consists of several volumes defined via the concept of solids, logical volumes and physical volumes giving rise to a hierarchical volume tree structure.

Material definition is accomplished using the classes `G4Element`, `G4Material` and `G4Isotope`. Elements may be defined directly with respect to their atomic properties like atomic mass and number or from isotopes by their relative abundance. A `G4Material` describes the macroscopic properties of matter. This again can be achieved either directly by specifying macroscopic quantities like charge, mass and density or by adding previously defined elements to the material.

PhysicsList Particles and physics processes are defined in this class. Constructing a PhysicsList is not straightforward and the user must wisely select the processes he wants to use in his detector simulation and assign them to appropriate particles. Finally, each particle is equipped with a list of processes describing how and when an interaction occurs. For this, a process provides a `GetPhysicalInteraction-Length()` method which proposes a step length and the `DoIt()` method invokes the process as can be seen in figure 2.5.

For several processes (especially hadronic ones), there are different models and cross section sets valid for different energy intervals to choose from. It is the user's responsibility to implement the most appropriate model and assign it to the specific process. In this context a model is a class whose methods implement the details of an interaction [Gea10].

User action classes

There are five additional optional user action classes (additional to the mandatory `PrimaryGeneratorAction`) the user may implement to access and control the simulation at various stages: `G4UserRunAction` on run level, `G4UserEventAction` on event level, `G4UserTrackingAction` on track level, `G4UserSteppingAction` on step level and `G4UserStackingAction` for stack management.

The `G4UserStackingAction` class manages the priority control of particle tracks, i.e. which particles are tracked first. An intelligent stack management may lead to a

better computational performance by selecting proper events for further processing and termination of irrelevant events.

2.10 Purity and efficiency

In order to determine the purity and efficiency, the truth information from MC data is used to compare the true particles to those from reconstruction. The so-called *MC truth* represents the actual parameters used in the simulation, the identities of generated particles and basically any other information which can be retrieved by the user.

The number of particles reconstructed as type r which are of true type t will be denoted as n_r^t. Mathematically, the purity is the ratio of the number of reconstructed particles n_r^t, which are really of type t to the number of all particles reconstructed as type r:

$$\mathcal{P}^t = \frac{n_r^t}{\sum_i n_r^i} = \frac{\#\text{ correctly reconstructed events}}{\#\text{ reconstructed events}} \,. \tag{2.23}$$

The purity $\mathcal{P}^t$ therefore describes the effectiveness of separating the particles of interest from particles with similar kinematic variables leading to a misidentification in the reconstruction algorithm.

The efficiency $\mathcal{E}^t$ specifies the efficiency of the particle identification by the ratio of correctly identified particles to the number of particles of true type t, which can actually be found by the analysis algorithm:

$$\mathcal{E}^t = \frac{n_r^t}{\sum_i n_i^t} = \frac{\#\text{ correctly reconstructed events}}{\#\text{ correct events}} \,. \tag{2.24}$$

It has to be noted that with $\mathcal{E}^t$ the efficiency of the analysis mechanism is meant, i.e. detector efficiencies are assumed to be equal for all particle types.

For a fixed detection setup, it is impossible to increase both purity and efficiency by applying specific cuts. Instead, an acceptable compromise needs to be found with the development of specific cut sequences for each reaction channel leading to values of $\mathcal{P}^t$ and $\mathcal{E}^t$ being as high as possible. These cut sequences may than be applied to measured data sets.

Chapter 3

Aspects of proton and heavy ion application in particle therapy

This chapter deals with the advantages of applying particle beams in radiation therapy. Concerning this issue, the impact of physical, biological and computer-specific aspects are discussed. Section 3.1 underlines the physical aspects of proton and heavy ion beams compared to conventional photon irradiation, whereas the biological effects of ionizing particles is discussed in section 3.2. Accurate MC methods can be adopted in particle therapy in various fields of application. Some examples are introduced in section 3.3.

3.1 Physical advantages of particle beams

In this section, two fundamental differences between particle beams and conventional photon irradiation are discussed leading to beneficial effects of proton and heavy ion beams. The dose profiles are compared in section 3.1.1, while the benefit of nuclear fragmentation of particle beams is presented in section 3.1.2.

3.1.1 Depth-dose distribution

The most prominent advantage of particle beams compared to conventional photon irradiation is the different depth-dose profile (see figure 3.1). For clinical photons the dose curve features a maximum a few centimeters beneath the skin. After the initial build-up region, the characteristic exponential dose decrease due to the absorption law determines the dose profile and hence an irradiation of deep-seated tumor sites is complicated.

By contrast, the dose profile of protons and heavy ions is characterised by a sharp

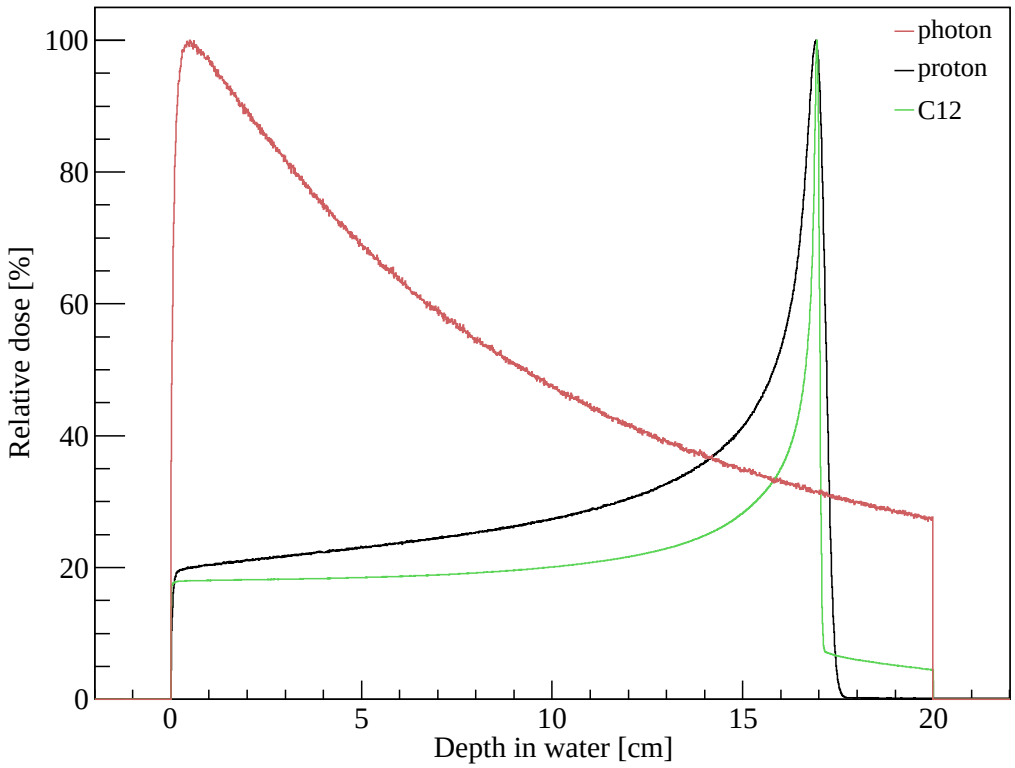

Fig. 3.1: Dose deposition in water of 300 MeV/u carbon ions, 158 MeV protons and photons simulated with Geant4. The photons were generated by bombarding 20 MeV electrons on a tungsten target. The curves have been normalised to the same height corresponding to a dose of 100 %.

maximum at the end of the particle range. This peak was first investigated by William Bragg [BK05] and is therefore called *Bragg peak*. The position of the Bragg peak can be adjusted to the desired depth by varying the kinetic energy of the incident ion beam allowing for precise irradiation of deep-seated tumors. In addition, the depth-dose curves of particle beams with different energies can be added optimally to form a spread-out Bragg peak which covers the entire tumor volume.

Particularly when it comes to an irradiation of tumors in the vicinity of organs at risk, proton and heavy ion radiation demonstrate their benefit of sharp dose profiles at the end of their range. In this context, organs at risk are radiosensitive organs or tissues next to tumor sites, which may receive a certain dose only to avoid irreversible damage.

Ideally, the tumor volume is completely covered by 100 % of the prescribed dose, while the surrounding healthy tissue should be spared. In daily clinical routine, a compromise between maximum dose in the tumor region and acceptable dose in healthy tissue has to be found.

3.1.2 Benefit of nuclear fragmentation for in vivo quality assurance

As was demonstrated in section 2.5, the residuals after nuclear fragmentation feature a specific range depending on their mass and charge and the initial range of the primary ion.

It may happen that one of the fragments is a positron emitter (e.g. the projectile fragment ^{11}C in the case of carbon beams). These isotopes allow for *in vivo*[1] quality assurance of the treatment by detecting the photon pair originating from the annihilation of the positron with an electron of the tissue material.

In proton therapy, β^+-emitting projectile fragments do not occur. Instead, the signal of the target fragments may be used to track the beam path inside the patient. It is therefore of great importance to have knowledge about the target material composition and the cross section for the reaction channels leading to a production of β^+-emitters.

The analysis of positron-emitting nuclear fragments using *positron emission tomography* (PET) allows to monitor beam positioning inside the patient. The spatial distribution of the β^+-activity, either measured online or offline, is compared to the predicted activity calculated in the treatment plan. The activity profile induced by carbon ion beams shows a sharp peak, because only the positron emitters ^{11}C and ^{10}C with half-lives of 19 s and 19 min contribute. This peak is superimposed by a broad and flat background distribution originating from target fragmentation [SESE10]. In this case, the range of the primary beam can be determined with an accuracy of 2 mm [KV07].

The activity of proton induced fragmentation does not show a clear peak structure due to the absence of projectile fragments; only the target fragments give a measurable signal. Nevertheless, it was shown that the quality assurance of proton therapy via PET analysis is feasible with millimeter precision for mono-energetic and spread-out Bragg peak fields on PMMA[2] phantoms [PPE04; PEH02].

3.2 Biological aspects

Different types of radiation produce different biological effects in tissue for the same physical dose. Depending on the energy transfer along the particles trajectory,

[1] Latin for "within a living organism".

[2] Poly(methyl methacrylate), a transparent thermoplastic commonly known under the trademark name *Plexiglas* [Roh].

sparsely ionizing radiation with low energy transfer $\mathrm{d}E/\mathrm{d}x$ (e.g. or X-rays or protons) is distinguished from densely ionizing radiation with high $\mathrm{d}E/\mathrm{d}x$ (e.g. carbon ions) in radiation therapy. The diversification in biological effectiveness is the result of an interplay between physical aspects like ionization density and biological parameters like cell repair capacities. Free ionization electrons and secondary ionizations destroy biochemical compounds and molecules.

In this regard, the most sensitive target is the DNA molecule inside the cell nucleus holding the genetic information (figure 3.2 (a)). Most of the isolated base damages and single strand breaks (figure 3.2 (b)) can be repaired with high reliability. For higher doses the probability of double strand breaks (figure 3.2 (c)) increases, finally leading to clustered lesions, where the cell loses its ability to divide (figure 3.2 (d)).

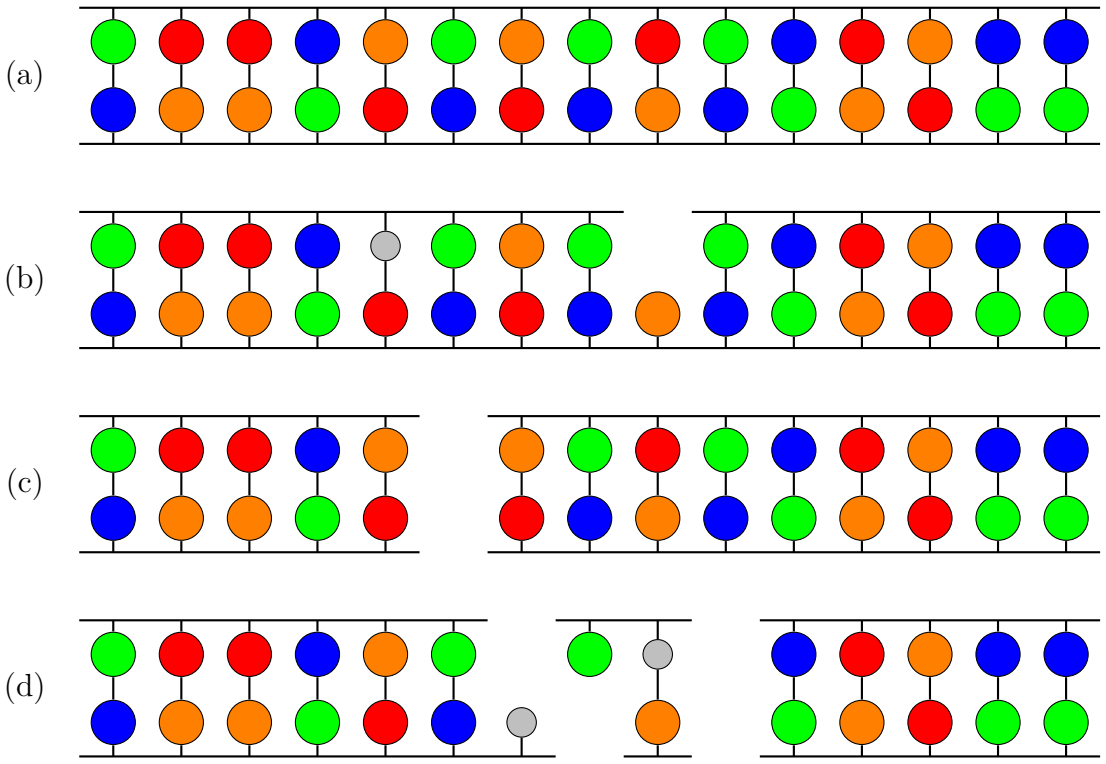

Fig. 3.2: Schematic presentation of an undamaged DNA molecule and its four nucleobases adenine, thymine, guanine and cytosine (a), single strand break and base damage of one of the nucleobases (b), double strand break (c) and a clustered lesion (d). Adapted for own purposes from [Wey04].

The energy transfer $\mathrm{d}E/\mathrm{d}x$ on tissue (which is closely related to the concept of *linear energy transfer* LET in dosimetry) for protons is quite similar to that of therapeutic X-rays. A review of a wide range of published data on determinations of RBE

values in *in vivo* and *in vitro*[3] systems by Paganetti et al. affirmed the use of a generic RBE of 1.1 for proton therapy [Pag+02]. RBE is set to this value for 150 – 250 MeV beams at several therapy centers like Massachusetts Generical Hospital, Loma Linda University or Paul Scherrer Institut [Pag+02].

In case of heavy ions like ^{12}C, a constant RBE is no longer reasonable, since the microscopic energy distribution along the particle's path varies. The number of ionization events is much higher compared to X-rays or protons leading to greater $\mathrm{d}E/\mathrm{d}x$ values. Furthermore the increase of RBE starts earlier than for protons, namely on the last two centimeters of range [KV07]. Additional dependencies (see e.g. [SESE10]) led to a poor general understanding of biophysical processes that governs biological response, so that no general model has been developed yet. Up to now there are six treatment facilities offering particle therapy with heavy ions [PTC], each one of them applying a different biophysical model for dose calculation.

Radio-resistant hypoxic tumors are ideal targets in proton and heavy ion irradiation due to enhanced RBE leading to improved clinical results [Bar+66; Bew68; Fur+00; Sta+04]. Hypoxic tumor cells are cells with a lower oxygen level than healthy cells due to the lack of blood-supplying vessels controlling oxygen flow to the cells in the tumor core. In general, hypoxic cells are up to three times more radioresistant than well blood-supplied normal tissue [Wey04].

Since the first treatment with particle radiation started at the Lawrence Berkeley Laboratory (LBL) in 1954, many patients have been treated with protons or heavy ion therapy. These treatment modalities have been proven to feature advantages over conventional therapy with X-rays at specific radiation sites like skull base. The dose profile allows for greater tumor conformity and hence a limiting dose in healthy tissue. At long last, nuclear reactions may occur during treatment, which can be used to verify the beam path inside the patient.

3.3 Applications of the Monte Carlo method in particle therapy

Two important applications of the MC method in particle therapy are discussed in this section, namely the secondary neutron dose estimation in section 3.3.1 and the use of MC codes as a commissioning tool in section 3.3.2.

[3]Latin, literally for "in glass", meaning "in an artificial environment outside the living organism".

3.3.1 Neutron dose estimation

Secondary neutrons are produced during proton treatment due to nuclear reactions and may contribute to the dose in tumor and healthy tissue. Charged target fragments have a limited range according to equation (2.18) and deposit their dose in the vicinity of the primary stopping position. This is not true for neutrons which are uncharged.

The unwanted neutron dose in healthy tissue stems from the production in the accelerator head and other structural components and in the patient himself and could be a significant contribution to the integral dose. In this respect, the risk of secondary malignancy production should be kept in mind especially for young patients [ZJP08].

Currently, two proton-beam delivery techniques exist: (1) In passive scattering various collimators, compensators and scatterers individually manufactured for each patient are placed in the beam line to produce a homogenous dose in the target region. (2) The active scanning technique uses magnets to steer the proton beam over the target volume and deliver the calculated dose to each voxel.

Because the secondary neutron dose largely depends on the geometry of the beam line, it is expected that active scanning methods produce less background radiation[Sch+02; Ago+98]. However, literature concerning this issue is very scarce making new measurements and their comparison to MC codes necessary.

An estimation of neutron doses in three substantially different facilities was carried out in [Ago+98], namely the proton therapy facilities of the National Accelerator Centre (NAC) in Faure, South Africa and of the Paul Scherrer Institute (PSI) in Villingen, Switzerland and the eye irradiation system at the Centre Antoine–Lacassagne (CAL) in Nice, France. The first one implements the passive scattering technique, whereas the second facility uses active beam scanning. The authors confirm the initial assumption of lower neutron doses in active beam scanning and estimate the contribution to the overall dose in passive beam scattering to be of the order of 1 Gy for a treatment dose of 60 Gy. Each beam delivery geometry was simulated using the FLUKA MC code (see section 2.9.1) and results were found to be consistent with measurements.

3.3.2 Monte Carlo as a commissioning tool

The construction of new proton therapy facilities is an expensive and persistent challenge. At a cost in the order of $100 million, the construction often takes years

until the first patients are treated. In order to reduce the time being spent on the commissioning and implementation of a (new) treatment planning system, MC data may be used prior to the availability of measured data. The simulation of the beam delivery system taking account of all its sub-structures could substitute beam data until construction is completed.

It was proven that it is possible to configure and test proton treatment planning in advance to avoid a potential risk of delay after the initial startup [New+07].

Chapter 4

Detection concept of the time-of-flight spectrometer

The first section of this chapter emphasizes the need for new measurements, particularly addressing sparse nuclear cross section data in the energy range relevant to particle therapy.

The new detector concept designed by the medical physics group of the Physics Institute 3B, RWTH Aachen to realize these measurements will be introduced in section 4.2. Special attention will be paid to the changes to the predecessor setup designed and engineered by Luc Schlömer in his diploma thesis [Sch09]. The hardware design including all detection components is subsequently presented in section 4.3.

4.1 The necessity of new measurements

The implementation of electromagnetic interactions in MC codes like Geant4 is rather uncomplicated as the underlying processes can be well described by theoretical models [JP08]. For nuclear reactions this is no longer valid and the implementation of hadronic physics is not straightforward. Within the Geant4 framework, there are different approaches to model final states.

Data driven models are largely based on evaluated or measured data. This way of modeling physics is considered to be optimal provided that the underlying data is available in adequate number. For example, data driven models are used in the scope of neutron transport, photon evaporation, calculation of inclusive cross sections and isotope production [Ago+03].

Parameterised models are mainly based on parameterisations and extrapolations of measured data like cross sections. This approach is used in hadronic shower physics, fission processes or estimation of inelastic final states.

Theory driven models are dominated by theories like quantum chromodynamics (QCD) or parton string models. The final state is then determined by sampling from theoretical distributions.

While the final implementation into the software framework may be different in distinct MC codes, the underlying modeling approaches and data bases are the same in many cases. As was shown in [Pia+10], some models and parameters used for simulating protons and their interactions with matter exhibit uncertainties, due to "incomplete understanding of fundamental physics processes, or practical inability to treat them thoroughly, non-existent or conflicting experimental data for a physical parameter or model, or the application of a physics model beyond the experimental conditions in which its validity has been demonstrated".

One of these data bases containing nuclear reaction data is the *Cross Section Information Storage and Retrieval System* (CSISRS) developed 40 years ago and which is still in use [Hol05]. Once in a while the name *EXFOR* ("Exchange Format") is used when CSISRS is meant, since both libraries are identical after they have merged in 1988 [Hol05]. With the help of the EXFOR database, the uncertainties and deficiencies of nuclear parameters are outlined using the example of nuclear cross sections for the production of secondary particles in proton therapy.

Secondary particle production data

The basic goal of the detection concept introduced in section 4.2 is to identify target fragments originating from nuclear reactions of protons irradiating the target material. In order to mimic the conditions in particle therapy, an appropriate target material has to be chosen. Because the most abundant elements in the chemical composition of human tissue are oxygen (65.0 % by weight) and carbon (18.5 % by weight) [Fri72], they are target material candidates. For reasons of usability, carbon is preferred to oxygen for the initial setup. In the future, further target materials are considered to be used. The most frequent output channels were determined by Oxana Grünwald in her PhD thesis [Grü11]. Table 4.1 quotes the top three reaction channels.

As already mentioned in section 3.1.2, positron-emitting isotopes play an important role in quality assurance during particle therapy treatment. The positron emitter ^{11}C is the most frequent target fragment in the energy range from 0 MeV – 200 MeV and its cross section has therefore thoroughly been investigated, as can be seen in figure 4.1.

Figures 4.2(a) and 4.2(b) show the cross section data for ^{11}B and ^{10}B production,

Tab. 4.1: Most abundant reaction channels of protons on a graphite target. The notation ^{X}C symbolizes the carbon isotopes ^{12}C and ^{13}C occuring in graphite. The possible presence of photons is described by the term γ'.

$p + {}^{X}C$	$\rightarrow$	$^{11}C + n + p + \gamma'$
		$^{11}B + 2p + \gamma'$
		$^{10}B + n + 2p + \gamma'$
		$\vdots$

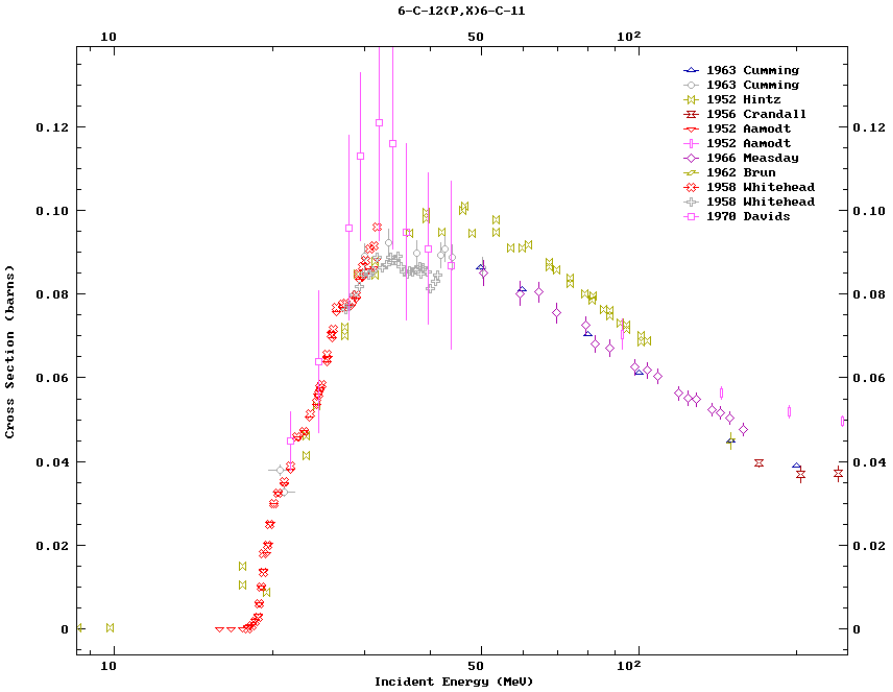

Fig. 4.1: Production cross section data for the reaction ^{X}C(p, X)^{11}C. Data retrieved from EXFOR database [Exf].

respectively. It is clearly evident that the measured data in these channels is not sufficient to predict cross section data accurately: The errors are to some extent substantially greater than 20 % and in the case of ^{10}B there are only three data points.

As described in section 3.3.1, neutrons play a significant role in secondary dose deposition. The estimation of its effect on specific patient topographies would in general be feasible by MC codes, the cross section for the production of ^{10}B along with a secondary neutron does not allow this consideration to be concluded. Furthermore, the measurement of de-excitation gammas (denoted as γ' in table 4.1) can be used as a method to verify in vivo the range of a clinical proton radiotherapy beam [VSS12].

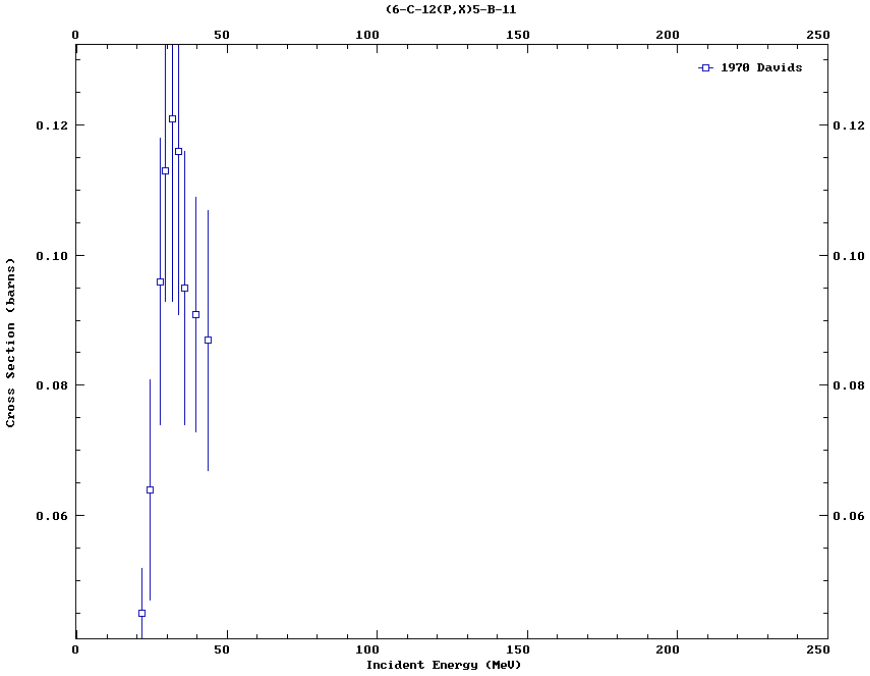

(a) cross section data for the reaction ^{X}C(p, X)^{11}B

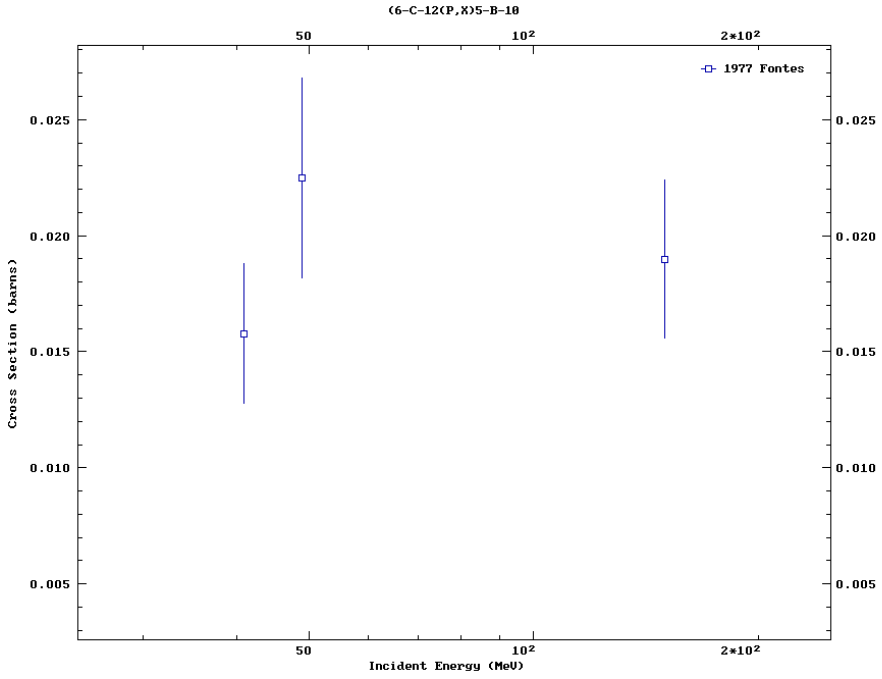

(b) cross section data for the reaction ^{X}C(p, X)^{10}B

Fig. 4.2: Production cross section data for ^{11}B and ^{10}B for energies relevant to proton therapy. Data retrieved from EXFOR database [Exf].

This procedure again requires a highly reliable simulation.

Therefore, it has to be concluded that the production data of two of the three most frequent nuclear reaction channels is not sufficient for accurate MC simulation in particle therapy. Regarding other reaction channels, a comparable situation arises as was extensively investigated in [Grü11]. New measurements have to be realized to fill this lack of insufficient data.

4.2 Current detector concept and inadequacies of the predecessor setup

The current detector concept presented in this thesis is the third iteration of a time-of-flight spectrometer developed by the medical physics group of Physics Institute 3B at RWTH Aachen. The first detector was designed and engineered by Kathrin Gester [Ges08], a redesign leading to the predecessor of the current setup was performed by Luc Schlömer [Sch09]. A schematic overview of this layout can be found in figure A.1 on page 121.

First, the basic concept of the predecessor setup is presented, before pointing out a number of inadequacies leading to the current layout. In particular, the concept of inverse kinematics is introduced in section 4.2.3, because it is applied in the current detection setup.

4.2.1 Detector concept

The aim of the detection setup is to measure double differential cross sections (see equation (2.4)) of sparse nuclear reaction channels. Therefore, it is necessary to identify the target fragments of these reactions.

A target fragment is characterised by its atomic charge Z and mass A and the kinetic energy E of individual target fragment species is varying making it necessary to stop the particles in a specific detection component to measure their total energy. In total, one is left with the three unknown variables Z, A and E to be determined for each fragment by measuring three kinematic variables in order to enable particle identification.

Because particle therapy is performed at rather low energies (up to $\approx 250\,\mathrm{MeV}$ in the case of protons), the velocity of fragments is low compared to the speed of light. This allows particle identification via time-of-flight techniques with flight distances in the order of few meters. At the end of the flight distance the present detector system

measures the energy loss per path length $\mathrm{d}E/\mathrm{d}x$ and the total energy loss E_{tot}. Together with the time-of-flight TOF the measurement of a set of three kinematic variables is realized.

4.2.2 Inadequacies of the predecessor layout

Several beam times at the COSY ("Cooler Synchrotron") storage ring of the Forschungszentrum Jülich revealed the need of a further redesign of the detection system. Thus, the inadequacies of the predecessor setup are discussed shortly:

- In the previous setup protons with kinetic energies of 200 MeV were focused on a graphite target to induce nuclear reactions (see figure A.1 in the appendix). 5 mm thick plastic scintillators stopped the time measurement and determined the energy loss per path length $\mathrm{d}E/\mathrm{d}x$. However, many of the target fragments exhibited too little kinetic energy to traverse one of the scintillators, but got stopped inside. This led to the problem that only their masses could be distinguished, rather than their charge [Grü11].
- In addition, the detection system was designed to measure only the time-of-flight and energy loss $\mathrm{d}E/\mathrm{d}x$ of particles. As mentioned above, one has to measure the total energy E_{tot} as well to identify a target fragment.
- As it will be shown in section 6.1, a large part of observed events were due to scattered protons instead of reaction products produced within the target which subsequently hit one of the stop scintillators. This misinterpretation distorts the statistics of correct target fragment hits and could have possibly been prevented by adding a properly chosen shielding to the detection setup.

The new detector design is built to avoid the aforementioned problems by applying the concept of inverse kinematics. Before going into more detail concerning the hardware setup, this concept will be explained.

4.2.3 Inverse kinematics

The concept of inverse kinematics means that the role of target and projectile particles are interchanged. In the case of the new TOF spectrometer, a primary carbon ion beam focused on a target containing hydrogen (e.g. polyethylene) is used to investigate the abundance of target fragments originating from nuclear interaction with the target material. Keeping the center-of-mass energy constant, the exchange of target and projectile does not change physics when viewed in the center-of-mass system.

Due to the high energy of the primary carbon ions (2280 MeV), the reactions to be examined are boosted in forward direction. Thus, a smaller detection area is needed leading to a more compact layout. Furthermore, thicker targets may be used so that the probability of carbon ions inducing a nuclear reaction is increased. Finally, the target fragments possess enough energy to traverse specific detectors of a few millimeter thickness for a $\mathrm{d}E/\mathrm{d}x$ measurement, which was one of the problems of the predecessor detection layout.

4.3 Hardware design

The current detector setup is shown in figure 4.3. An enlarged view of the detection chamber can be found in figure 4.4. Detectors terminating the TOF also perform measurements concerning $\mathrm{d}E/\mathrm{d}x$. These components are discussed in section 4.3.1. The calorimeter for total energy determination is treated in section 4.3.2.

The veto system to suppress background from the start detector is presented in section 4.3.3. A detection chamber housing all detection components is the topic of section 4.3.4.

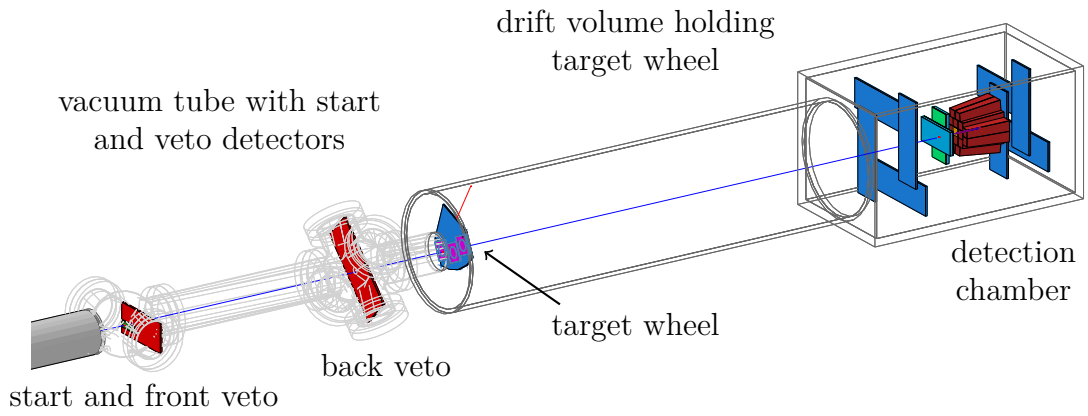

Fig. 4.3: Geant4 model representing the simulated TOF spectrometer and a single primary particle entering from the left. For a more detailed view of the first vacuum tube, see figure 4.6. The detection chamber is shown in figure 4.4.

4.3.1 Hardware components for TOF and dE/dx measurements

Start detector Primary particles coming from the left in figure 4.3 first hit the start scintillator and initiate the time-of-flight measurement. The start detector was designed and constructed by Eva Kreysing and Alexander Mantz in the course of

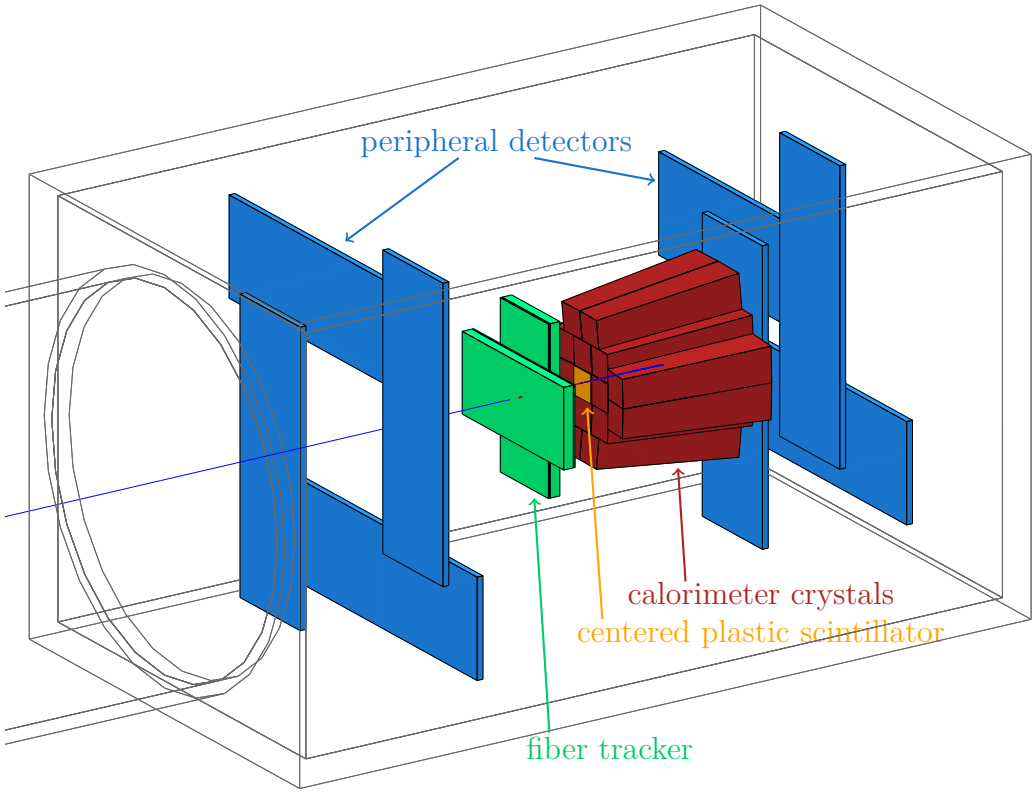

Fig. 4.4: Geant4 model representing the simulated detection chamber and a single primary particle getting stopped in the center plastic scintillator after crossing the fiber tracker modules.

their bachelor thesis [KM10]. It consists of a 1 mm thick plastic scintillator of type BC-422 manufactured by Saint-Gobain. This material has a short rise time of 0.35 ns [Saib], which allows for a good timing resolution. The readout is performed by four $1 \times 1\,\mathrm{mm}^2$ Silicon photomultipliers (SiPM). Because nuclear reactions may occur within the start detector, the thickness of the start scintillator has to be chosen carefully. If it is too thick, the probability of a nuclear reaction increases, but it has to be thick enough to produce a sufficient amount of light for readout.

After passing the start detector, the primary particle impinges on the target and potentially undergoes a nuclear reaction with the target material, where the target fragments of interest are created. The time measurement is stopped as soon as a particle hits one of the fiber tracker modules.

Fiber tracker A fiber tracker module is composed of scintillating fibers glued together to form a five-ply ribbon. Each fiber tracker is 64 mm in width and 170 mm in length, the fibers have a diameter of 240 µm. Two modules are aligned perpendic-

ularly to each other in horizontal and vertical orientation. In so doing, an "array" of perpendicular fibers is built allowing to achieve spatial information of particle hits. Photos of a fully mounted fiber tracker module and the fiber layers can be found in the appendix B in figures B.1 to B.3. In addition, the readout system consisting of 32 SiPM can be seen in the last two pictures.

The energy deposited in the fiber tracker modules is further used for the energy loss measurement. Particles traversing the fibers lose a small amount of their energy due to interaction with the fiber material. This energy loss $\mathrm{d}E/\mathrm{d}x$ is one of the measured quantities introduced in section 4.2 that enables particle identification. The fiber ribbons are glued and mounted on a support structure made of Rohacell® foam, which is light enough so that particles do not lose a considerable amount of energy compared to the $\mathrm{d}E/\mathrm{d}x$ in the fibers.

Scintillation bar tracker During the design phase of the detection setup, the assembly of plastic scintillation stripes was considered for additional TOF and $\mathrm{d}E/\mathrm{d}x$ measurements. Therefore, this detection device is redundant to the fiber tracker. It has been added to the already existing implementation of the fiber tracker into the `DetectorConstruction` in the initial phase of this thesis and used for specific analyses. A schematic drawing of the detection chamber containing the scintillation bar tracker can be found in figure 4.5. Henceforth, this detection device is simply called bar tracker.

Peripheral detectors The peripheral or frame detectors are used to gain information of particles which do not hit the fiber tracker due to an increased scattering angle or pass the calorimeter setup.

They are monolithic plastic scintillator slabs of material type EJ-230 (comparable to Saint-Gobain's BC-420) manufactured by Eljen Technology with sensitive areas in the dimensions of $80\,\mathrm{mm} \times 235\,\mathrm{mm} \times 5\,\mathrm{mm}$. A small groove is milled into the long edges of each scintillator holding a wavelength shifting fiber for light collection and guidance to the SiPM.

Four of these modules are placed in front of the fiber trackers as shown in figure 4.4 to detect particles showing greater angles with respect to the beam line axis. Becasue these particles will not hit the calorimeter after passing the frame detectors, only TOF and $\mathrm{d}E/\mathrm{d}x$ information is collected.

Another four identical modules are located right behind the calorimeter as a tail catcher detecting particles which managed to pass the crystals. In particular, these are lighter particles like protons or deuterons.

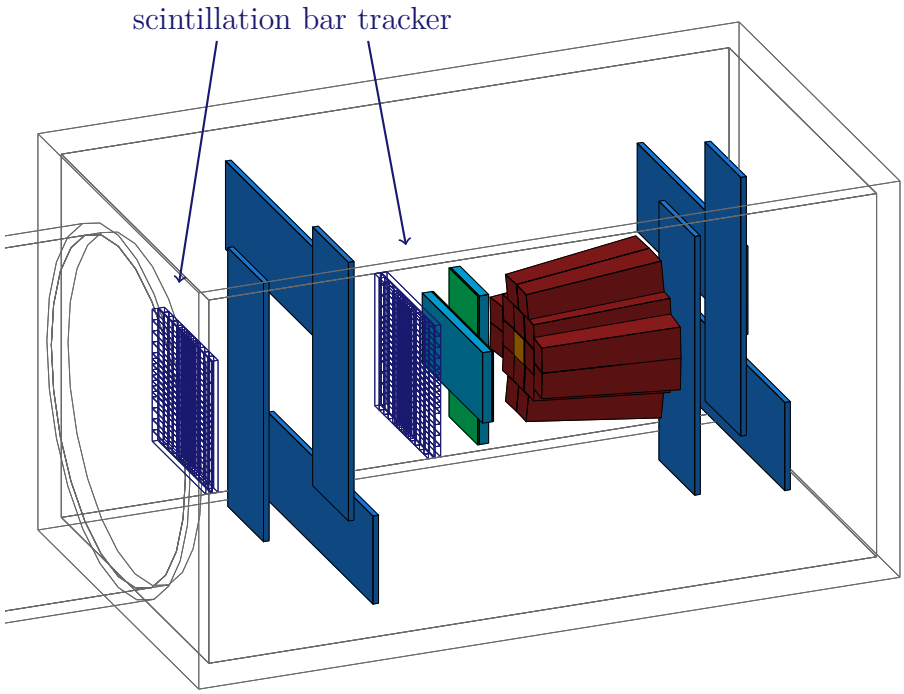

Fig. 4.5: Drawing of the detection chamber with the additional scintillation bar trackers. There are four modules, two of which are arranged perpendicularly to form a grid allowing for spatial resolution. The measures of the inner stripes are 120 mm × 5 mm × 5 mm and therefore half as thick as the outer stripes with dimensions of 120 mm × 10 mm × 5 mm.

4.3.2 Hardware components for total energy measurement

The total energy is finally measured by stopping the particle in one of 16 BGO calorimeter crystals (BGO: bismuth germanium oxide, chemical formula $Bi_4Ge_3O_{12}$, density 7.13 g/cm^3 [Saia]). In the center position of the arrangement the BGO crystal is replaced by a plastic scintillator. This is done to avoid high beam rates, which increases the risk of damage on the (rather expensive) BGO crystals.

The dimensions of the crystals are slightly varying because they originate from longer crystals which were cut in half and polished afterwards. Edge lengths are within in the range of 20 – 30 mm and crystal lengths are roughly 114 – 120 mm [Kos13]. A photo of the BGO crystals and the centered plastic scintillator mounted in a specifically designed clamp can be found in the appendix in figure B.4.

4.3.3 Veto detectors

As mentioned above, it may occur that a nuclear reaction takes place in the start detector or primary particles are scattered away from beam axis. A veto system consisting of two plastic scintillators each having a small aperture is placed behind

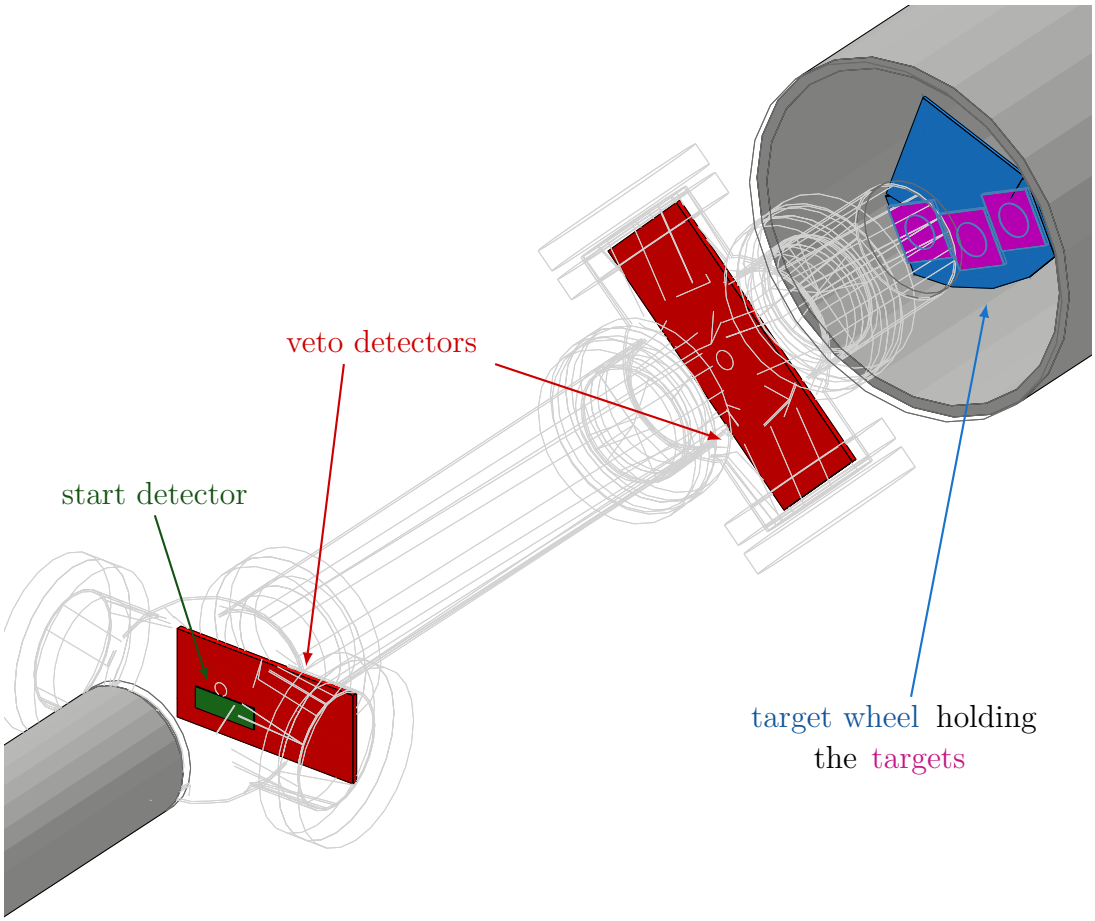

Fig. 4.6: Geant4 model representing the first vacuum tube holding the start and veto detectors. The connecting vacuum tube on the right contains the target wheel for the choice of different target thicknesses.

the start detector, so that a veto signal is triggered by particles hitting one of the scintillators. This signal can be used to filter the background from the start detector, while the primary particles correctly passing the start detector and the veto hole produce no veto hit. The effectiveness of this system was examined in [Grü11] and the results can be found in figure A.2 in the appendix. Table 4.2 lists the dimensions of each veto scintillator and its aperture.

Tab. 4.2: Dimensions and aperture diameter of the veto detectors.

	dimensions [mm^3]	**aperture diameter [mm]**
front veto	$180 \times 83 \times 5$	11.95
back veto	$255 \times 99 \times 5$	17.15

4.3.4 Vacuum chamber

The experiment is performed in vacuum of 0.1 mbar or better. As was investigated in [Grü11], keeping the residual pressure below this value is sufficient for an accurate separation of the target fragment masses. The actual setup is subdivided into three components. Start and veto detectors are housed in a pipe with an inner diameter of 10 cm and a length of 1 m. This pipe is connected to the beam tube of the accelerator.

A second vacuum tube (inner diameter 30 cm, length 1.2 m) joined to this pipe acts as a drift volume for the target fragments, so that the TOF is long enough for adequate measuring. The target itself is placed at the beginning of the tube (see figure 4.6).

After passing the drift tube, the target fragments enter the detection chamber holding the detectors for TOF, $\mathrm{d}E/\mathrm{d}x$ and E_{tot} measurements. The inner dimensions of the chamber are 33 cm × 33 cm × 60 cm.

4.3.5 Light readout

The light produced in the scintillators is collected and subsequently read out by photon sensitive devices. In the setup presented here, silicon photomultipliers (SiPM) and PIN diodes are used. The start and veto detectors, the peripheral detectors, the central calorimeter plastic scintillator and the fiber tracker modules use SiPM for readout, whereas the BGO crystals are coupled to PIN photodiodes.

For further information concerning SiPM and PIN photodiodes see the (hardware) theses of the medical physics group, for example [Sch09; Bac11; Lew12; Kos13].

Chapter 5

Implementation of the time-of-flight spectrometer into a Geant4 simulation

One of the main tasks of this thesis is the detailed simulation of the detection layout using the Geant4 libraries, for example for evaluating the setup (results see chapter 6). Each detection component is integrated into the simulation, whereas the readout devices like SiPM and PIN photodiodes are left out. This is because optical processes are not considered in the present detector simulation. Instead, the measured resolutions are considered after simulation in the reconstruction code (see chapter 7) to retrieve realistic results.

Sections 5.1 to 5.3 address the implementation of the three most important (and the only mandatory) classes of a Geant4 simulation, the `DetectorConstruction`, the `PhysicsList` and the `PrimaryGeneratorAction`. Additional classes of some importance for the detector simulation will be presented subsequently in section 5.4.

Section 5.5 shortly summarizes which Geant4 version was used to gain the results presented in this thesis and which programs helped to accumulate the data.

5.1 Defining the detector setup: DetectorConstruction

As mentioned in section 2.9.4, the Geant4 `DetectorConstruction` class offers the user the possibility to describe his own geometry on the concept of solids, logical volumes and physical volumes. Thus, the materials, dimensions and the relative positions of detector volumes must be known. The more exact the real measures and

material compositions are incorporated into the `DetectorConstruction`, the more precise are the results obtained from the simulation.

Materials The materials of the detector simulation are implemented manually with the exact composition wherever possible. An example is the aluminium alloy used for the detection chamber manufactured by the mechanics workshop of the Physics Institute 3B of RWTH Aachen.

Another method of implementing materials is the use of the NIST ("National Institute of Standards and Technology") database, which has its own Geant4 utility class `G4NistManager` to steer the implementation of materials. This database includes the natural isotopic compositions of elements and further provides material compositions of important chemical compositions like bone or muscle[1]. The NIST database is used to specify the materials of the BGO crystals (density: $7.13\,\mathrm{g/cm^3}$, atomic weight per fraction: O: 0.154126, Ge: 0.17482, Bi: 0.671054), the fiber tracker and peripheral detectors (density: $1.032\,\mathrm{g/cm^3}$, H: 0.085, C: 0.915) and the polyethylene target (density: $0.94\,\mathrm{g/cm^3}$, H: 0.143711, C: 0.856289).

The fibers used for the fiber tracker are of type SCSF–78MJ manufactured by Kuraray [Lew12]. A fiber core is surrounded by two claddings, each having a thickness of 3 % of the total fiber diameter of 240 µm. Sense and purpose of these claddings is to confine the light to the core by total reflection at the boundaries, so that little light is lost. The refractive indices of the claddings are therefore lower than that of the fiber core. Although optical processes are not considered in the simulation, the claddings are simulated for the sake of accuracy and in preparation for a possible future simulation of the readout. Table 5.1 summarizes the required information of the fibers to be used in the `DetectorConstruction`. A datasheet with a comprehensive list of properties of Kuraray's scintillating fibers can be found in [Kur]. Furthermore, the Rohacell® foam of the support structure is simulated using a density of $0.052\,\mathrm{g/cm^3}$.

Tab. 5.1: Materials used for each fiber component and the corresponding densities.

	material	**chemical formula**	**density [g/cm³]**
core	polystyrene	C_8H_8	1.050
inner cladding	polymethylmethacrylate (PMMA)	$C_5H_8O_2$	1.190
outer cladding	fluorinated polymer	corporate secret	1.400

As mentioned in section 4.3.4, the experiment is running in vacuum of 0.1 mbar or

[1] A comprehensive list of all NIST materials can be found at `http://geant4.cern.ch/UserDocumentation/UsersGuides/ForApplicationDeveloper/html/apas10.html`

better. This is achieved using the ideal gas law to define the density of the vacuum, which is a mandatory quantity in the material definition of Geant4. In this context, a temperature of 293 K is assumed.

Geometries The geometric shape of each detection component is simulated using the pre-defined solids of Geant4 like boxes, tubes or trapezoids in the case of the BGO crystals. These basic solids can be composed to form *boolean solids* for more complex structures. In many cases volumes need to be placed inside other volumes. The veto detector, for example, is composed of a regular box-shaped scintillator (solid: `G4Box`) housing a slice-shaped aperture (solid: `G4Tubs`). The visualization of the detector construction is shown in the foregoing chapter in figures 4.3 to 4.6.

5.2 Particles and processes: PhysicsList

One of the main purposes of the thesis of Oxana Grünwald [Grü11] was to find an optimal configuration of physics processes and models for use in particle therapy applications. Geant4 processes are divided into several categories. Because optical processes are not considered, three categories remain which have to be taken into account:

- electromagnetic (section 5.2.1),
- hadronic (section 5.2.2) and
- decay (section 5.2.3).

It is the user's responsibility to choose between a variety of models relevant to different energy ranges for each process. Large effort is required to verify which model is the most appropriate for a specific process.

Due to the use of inverse kinematics (see section 4.2.3), physics models are slightly varying to the ones determined in [Grü11]. Starting from the physics setup validated for the predecessor setup, the applied models and the differences will be discussed in the following.

5.2.1 Electromagnetic physics

Geant4 electromagnetic (EM) physics manages the EM interactions of leptons, photons, charged hadrons and ions. The processes are organized in a package structure each intended for specific purposes. For the use of Geant4 in particle therapy the *standard electromagnetic* (SEM) package [Bur+04] and the *low energy* model [Cha+01;

Cha+04] are possible candidates. The SEM package averages atomic shell effects and it is not expected to yield accurate results below 1 keV [Ago+03]. The low energy package provides alternative models extended to lower energies down to 250 eV.

C. Z. Jarlskog and H. Paganetti carried out a comprehensive study of electromagnetic and hadronic interactions against measured data in order to find the most suitable physics setting to be used in proton therapy [JP08]. As a conclusion, "the standard electromagnetic model was found to be more suitable than the low-energy parameterized" [JP08].

In addition to its default implementation `G4EmStandardPhysics`, the SEM package offers several sub-packages with modified parameters or extended models for specific purposes. The SEM model with its third option `G4EmStandardPhysics_option3` is recommended by the Geant4 SEM working group for use in medical physics applications [Gre+10; Iva11]. It is therefore added to the `PhysicsList` and replaces the default package used in [Grü11].

An overview of the implemented electromagnetic models is given in the following. Hadronic and decay processes are treated in sections 5.2.2 and 5.2.3. Most of the physics described in these sections can be studied in more detail in [Gea10].

Standard electromagnetic model with option 3

The `G4EmStandardPhysics_option3` package was designed for applications requiring higher accuracy of electron, hadron and ion tracking in the absence of a magnetic field [Geab].

A primary particle with total energy E_{prim} will explicitly generate a secondary particle with kinetic energy T, if $T > T_{\text{cut}}$. A production threshold T_{cut} (simply called range cut) has to be defined below which secondaries are not produced. Rather than specifying an energy cut-off, these thresholds are defined as a distance or range and than converted into energies for each material. The proper determination of cuts is a delicate issue. Large cut values could lead to imprecise stopping of particles. If cuts are chosen to be very low, more CPU time is used to track low-energy secondary particles. Nevertheless, the SEM package comes along with default cut values, which are used in the simulation of the TOF spectrometer.

Continuous energy loss Below the threshold T_{cut} the "soft" secondaries are simulated as continuous energy loss by their parent particle via

$$\frac{\mathrm{d}E_{\text{soft}}(E_{\text{prim}},\, T_{\text{cut}})}{\mathrm{d}x} = n_{\text{at}} \int_0^{T_{\text{cut}}} \frac{\mathrm{d}\sigma(Z,\, E_{\text{prim}},\, T)}{\mathrm{d}T} T \,\mathrm{d}T \tag{5.1}$$

where n_{at} is the number of atoms per unit volume and

$$\frac{\mathrm{d}\sigma(Z,\, E_{\text{prim}},\, T)}{\mathrm{d}T} \tag{5.2}$$

denotes the differential cross section per atom (with atomic number Z) for the ejection of a secondary particle with kinetic energy T.

The mean rate of the continuous energy loss is pre-calculated in the initialization phase of Geant4 and stored in a $\mathrm{d}E/\mathrm{d}x$ table. During runtime, values of continuous energy losses ΔT of particles can be obtained using these tables:

$$\Delta T = \frac{\mathrm{d}E_{\text{soft}}}{\mathrm{d}x}\Delta s \ , \tag{5.3}$$

with Δs being the step length. By default, 120 bins are stored in these tables for the energy range of 100 eV to 100 TeV using the SEM package leading to a corresponding resolution of 10 bins/decade [Gea10]. In the SEM option 3 sub-package a default value of 220 bins in the energy range of 100 eV to 10 TeV is used. A doubled resolution of 20 bins/decade is achieved.

Integration of equation (5.1) leads to the Bethe restricted energy loss formula (energy transfers are restricted to $T \leq T_{\text{cut}} \leq T_{\text{max}}$) [Ber+12], which takes several corrections into account:

$$\frac{\mathrm{d}E_{\text{soft}}}{\mathrm{d}x} = 2\pi r_e^2 m_e c^2 n_{\text{el}} \frac{z^2}{\beta^2}\left[\ln\left(\frac{2m_e c^2\beta^2\gamma^2 T_{\text{up}}}{I^2}\right) - \beta^2\left(1 + \frac{T_{\text{up}}}{T_{\text{max}}}\right) - \delta - \frac{2C_e}{Z} + F\right] \tag{5.4}$$

The constants, properties and corrections used in equation (5.4) are summarized in table 5.2.

Because inverse kinematics is applied in the current setup, carbon ions are used as beam particles. The energy loss of ions heavier than protons is calculated using scaled kinetic energies:

$$T_{\text{scaled}} = T\frac{M_{\text{base}}}{M_{\text{particle}}} \tag{5.5}$$

Base particle for ions with $Z > 2$ is the virtual particle `G4GenericIon`, which has mass, charge and further quantum numbers of the proton [Gea10]. The continuous energy loss is then defined via a scaling relation:

$$\frac{\mathrm{d}E}{\mathrm{d}x}(T) = q_{\text{eff}}^2\left[F_1(T)\frac{\mathrm{d}E}{\mathrm{d}x}_{\text{base}}(T_{\text{scaled}}) + F_2(T,\, q_{\text{eff}})\right] \ , \tag{5.6}$$

where q_{eff} is the effective nuclear charge. For slow ions q_{eff} differs from the nucleus

Tab. 5.2: Summary of variables used in equation (5.4). c, $\beta = v/c$ and $\gamma = 1/\sqrt{1-\beta^2}$ have their usual meanings.

symbol	definition
	constants
r_e	classical electron radius $e^2/4\pi\epsilon_0 m_e c^2$
$m_e c^2$	electron mass $\times c^2$
	particle and material properties
n_{el}	electron density in the material
z	charge of the hadron
Z	atomic number of the material
T_{up}	$\min(T_{\mathrm{cut}}, T_{\mathrm{max}})$
T_{max}	maximum energy transferable to a free electron
I	mean excitation energy in the material
	correction functions
δ	density effect function
C_e	shell correction function
F	higher order correction

charge due to the interaction of electrons with matter [Gea10]. An approach of calculating effective charges of ions from its atomic number and velocity can be found in [ZM89]. F_1 and F_2 are correction functions taking the Birks effect, Bloch corrections and low energy corrections into account.

Delta ray production For $T_{\mathrm{cut}} < T < T_{\mathrm{max}}$ secondary particles are explicitly generated, which themselves ionize the penetrated matter. The cross section for producing secondary electrons with $T \ll I$ is given by

$$\frac{\mathrm{d}\sigma}{\mathrm{d}T} = 2\pi r_e^2 m_e c^2 Z \frac{z^2}{\beta^2}\frac{1}{T^2}\left[1 - \beta^2\frac{T}{T_{\mathrm{max}}} + \frac{T^2}{2E^2}\right] , \tag{5.7}$$

where I is the mean excitation energy of the material.

Once the kinetic energy of the δ-electron is successfully sampled, the direction of the electron is determined. The azimuth angle ϕ is sampled isotropically, whereas the energy-momentum conservation is used for calculating the polar angle θ. From this, the energy and momentum of both the parent particle and δ-electron can be derived and transformed into the global coordinate system.

5.2.2 Hadronic physics

As the nuclear system evolves with time, different phases are reached which are treated by selected models within Geant4. First, the primary beam particle enters a nucleus of a specific material and interacts with individual nucleons via two-body collisions. Secondary particles eventually produced in these collisions participate in the collision process leading to an intra-nuclear cascade of two-body interactions. When the kinetic energy of the participants falls below some threshold, the cascade is stopped and the residual excited nucleus is treated by de-excitation models until statistical equilibrium is reached. The equilibrated nucleus is allowed to emit further nucleons or photons, if its excitation energy is large enough. In summary, a nuclear reaction chain is divided into

- an intra-nuclear cascade,
- the de-excitation of the pre-equilibrium state nucleus and
- a further de-excitation of the equilibrium state nucleus.

The models chosen in this work for simulating each nuclear state shall be discussed in the following.

The binary light ion cascade Two cascade models exist and are applicable in the energy region of the current simulation: The Bertini cascade model and the binary cascade model. Recommendations found in the literature [JP08] prefer the binary cascade model as it seems to be more compliant with measurements. This led to the decision to use the binary cascade model for the simulation of the predecessor detection setup [Grü11]. The binary cascade model is implemented in two different classes. The `G4BinaryCascade` class is applicable to primary protons and neutrons and thus was used in the predecessor setup. With the new detector layout, the second class `G4BinaryLightIonReaction` applicable to light[2] ions like ^{12}C is the optimal solution [Iva11].

The binary cascade simulates the inelastic scattering of protons, neutrons and light ions with target nuclei for projectile energies up to 10 GeV [Geaa]. Each interaction can be described by a binary collision between a nucleon of the target material and a component of the projectile. Secondary particles produced in these collisions enter the cascade interface leading to an intra-nuclear cascade.

The initial condition of the cascade algorithm is made up of the projectile's properties and three-dimensional models of the target and projectile nucleus. Target and

[2]In the context of nuclear physics and in contrast to radiation therapy, ^{12}C is a light ion.

beam nuclei are supposed to be spherical and isotropic. Nuclei with $A > 16$ are modeled using a Woods–Saxon density distribution, for lighter nuclei ($A \leq 16$) a harmonic oscillator shell model approach is applied. The momenta $\boldsymbol{p}_i$ of nucleons are sampled randomly between 0 and the Fermi momentum $p_{\mathrm{F}}^{\max}(r_i)$.

Next, an impact parameter b is sampled and corresponding distances of closest approach $d_i^{\min}$ to each target nucleon i are calculated. A nucleon i is considered as a possible interaction candidate, if

$$d_i^{\min} < \sqrt{\frac{\sigma_i}{\pi}} \; . \tag{5.8}$$

The σ_i are two-body elastic and reaction cross sections and where available, experimental data is used as direct input or for parameterizations. Possible collision candidates fulfilling equation (5.8) are ordered by their time-of-flight to the point of closest approach $d_i^{\min}$. The projectile is then transported to the first collision. If no collision candidate was found, a new impact parameter is sampled. At the end of the step, the interaction between the primary and the nucleon is checked for Fermi exclusion and if accepted, it is simulated and the secondary particles emerging from the binary-collision are treated as primary particles and new interaction sites are calculated as described above.

The cascade process is terminated when the maximum kinetic energy $T_{\max}$ and the mean kinetic energy of the participants T_{mean} fall below certain thresholds. In Geant4 version 9.4 these thresholds are set to $T_{\max} = 75\,\mathrm{MeV}$ and $T_{\mathrm{mean}} = 15\,\mathrm{MeV}$. The state of the residual nuclear system is then registered as the initial state for the precompound model, which is subsequently invoked.

The precompound model The implementation of the precompound model allows for two use cases: It can be used as an independent hadronic interaction model and as an interface model between the cascade model valid at higher energies and the equilibrium model [LW00]. In the current simulation, it is used as the latter one being invoked automatically by the binary cascade model after cascade has terminated in order to equilibrate the excited nucleus.

The precompound model is based on Griffin's semiclassical exciton model [Gri66], where the nucleus states are characterized by the number of excitons n_{exc}. In this context, an exciton is understood as a particle excited from the ground state and leaving a hole behind. The excited nucleus is equilibrated by successive two-body interactions. At each step of the equilibrium process two competing decay modes may be invoked: (1) exciton-exciton interactions to other configurations and (2) the

emission of particles into the continuum.

In the first case, only transitions with $\Delta n_{\text{exc}} = 0, \pm 2$ are taken into account. The composite nucleus may also decay by one of the six evaporation channels, namely the emission of n, p ^{2}H, ^{3}H, ^{3}He and ^{4}He. When the nuclear system has reached statistical equilibrium, a state where the average number of excitons remains constant, a compound nucleus with excitation energy E^* is left behind. Further de-excitation of the thermalized compound nucleus is handled by a set of equilibrium models.

Equilibrium models Depending on the atomic mass A, atomic number Z and the excitation energy E^* of the residual nucleus, different equilibrium models are called which may lead to the emission of photons, nucleons or heavier fragments. The decay process is managed by the `G4ExcitationHandler` class, which steers the invocation of equilibrium models for the final breakup of the nucleus and returns a list of target fragments without excitation energies.

The de-excitation models treated by the excitation handler are `G4VMultiFragmentation`, `G4VFermiBreakUp`, `G4VEvaporation` and `G4VPhotonEvaporation`. Figure 5.1 illustrates the conditions for their invocation and the flow towards a final set of stable reaction products.

At high excitation energies $E^* > 3\,\text{MeV/nucleon}$, the statistical breakup via an explosion-like de-excitation process becomes dominant. The multifragmentation model `G4VMultiFragmentation` predicts the final state of a nucleus after this form of decay. As soon as a channel has been selected, the kinetic energies of fragments are determined obeying a Boltzmann distribution in the rest frame of the nucleus. All fragments are then transported by solving the equations of motion in a time-dependent Coulomb field [Bot+87].

For lighter nuclei ($A < A_{\text{max}} = 17$, see figure 5.1) smaller excitation energies comparable to the binding energy of the nucleus may lead to a breakup into two or more fragments [Gea10]. In this context, the `G4VFermiBreakUp` model is used, which was first introduced by Fermi in 1950 [Fer50]. As statistical multifragmentation, the Fermi breakup process is an explosion-like decay. However, final states are assumed to be in ground state or low-lying excited states [Gea10]. Once a configuration has been selected, momenta of fragments are sampled randomly over the whole phase space without any constraint.

The `G4VEvaporation` class simulates the de-excitation of an excited nucleus by emission of light fragments. The excitation energy is shared by a large number of nucleons, until one nucleon has united enough energy to leave the nucleus. Therefore,

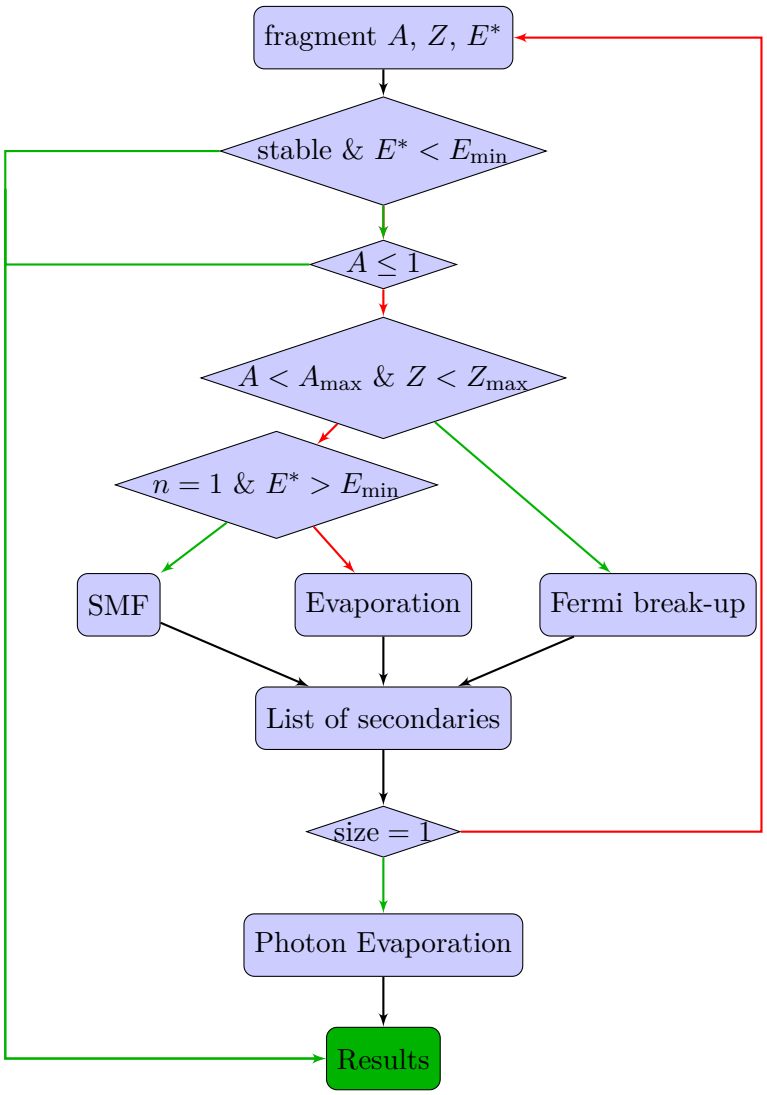

Fig. 5.1: Flowchart derived from the program code of the excitation handler class illustrating the de-excitation loop of fragments. The initial fragment characterized by A, Z and E^* enters the de-excitation loop if it is unstable, sufficiently excited and heavier than a proton. Light nuclei will most likely treated by the Fermi break-up model. Only in the first iteration ($n = 1$), the particle may undergo statistical multifragmentation. For the (possibly) following iterations either the evaporation model or Fermi break-up is applied. At the end of the de-excitation loop, it is checked whether the particle has decayed ($n_{\mathrm{sec}} > 1$) or not. In the former case, each of the new fragments enters the de-excitation loop. In the latter case, when no decay was possible, the final invocation of the photon evaporation model leads to a stable, unexcited particle.

the emission of very light particles is most likely to occur. The channels which lead to the evaporation of these light nuclei are managed by the `G4VEvaporationChannel` class. By default, there are six competing channels to be treated, namely the emission of n, p, ^{2}H, ^{3}H, ^{3}He and ^{4}He. Weisskopf and Ewing were the first one to introduce

a statistical theory for the decay of compound nuclei [WE40].

In the last step of the excitation phase, photons with discrete energies are evaporated from the excited nucleus controlled by the `G4VPhotonEvaporation` class. Experimental data in the form of excitation energies, spins, parities and transition probabilities from the Evaluated Nuclear Structure Data File (ENSDF) is implemented in the code to model discrete E1, M1 and E2 photon transitions which are considered in this step.

5.2.3 Decay

The `G4Decay` class manages the decay of particles in flight and at rest. For a particle in flight, a step length $\lambda = \gamma\beta c\tau$ is calculated considering the half-life τ of the particle [Gea10]. If the particle is at rest, the decay time in the rest frame of the particle is converted to a decay length. The class also chooses a decay mode according to the branching ratios defined in the class `G4DecayTable`. Geant4 has pre-defined decay tables for most unstable particles based on data from the Particle Data Group [Ber+12], which are used in the present detector simulation.

5.3 Generating a primary event: PrimaryGeneratorAction

The `PrimaryGeneratorAction` class describes the properties of the beam and creates the initial particles at the beginning of each event. For the simulation of the TOF spectrometer, a kinetic energy of 2280 MeV is used for the primary carbon ions, which corresponds to the same center-of-mass energy as 200 MeV protons, a typical energy applied in particle therapy with protons. The primary particles are generated roughly 350 cm before the target.

Multiwire proportional chambers installed at the beam site at COSY are able to measure the beam profile at various positions of the beam line. According to the COSY control team during beam time in January 2011, the full width at half maximum (FWHM) in front of the collimator amounts to 0.74 cm. This value is used to simulate a gaussian distributed particle position at the primary vertex.

5.4 Further classes

Three further classes of some importance are discussed in the following, namely the Geant4 `SteppingAction` in section 5.4.1 and the `SimulatedData` and `MeasuredData` in section 5.4.2.

5.4.1 SteppingAction

One of the most important Geant4 classes concerning data selection and storage is the optional user action class `SteppingAction`, which is invoked for each step of a Geant4 simulation. Therefore, the implementation of this class needs to be handled with care as it is very time-consuming. For the simulation of the TOF spectrometer, the `SteppingAction` is used to check for particle transition through detection volumes. In so doing, information about start and veto hits or the occurrence of nuclear reactions in the target is accessed, for example. Apart from this, any information of interest for a specific purpose may be stored for post-simulation analysis. However, the key task of the `SteppingAction` is to retrieve the energy deposition and time-of-flight of particles in the fiber tracker and calorimeter crystals. In this context, the detectors are not addressed by their volume name strings[3], but rather by their *region information* described in the following.

Geant4's concept of region and region information is applicable to logical volumes, which, as a result, become *root logical volumes*. All daughter volumes belonging to the root logical volume share the same region, unless a daughter volume itself is assigned to another region. One advantage of the region concept is to group several volumes into a joint region. For example, both veto detectors are summarized in the "veto region". Furthermore, each region may have its unique production cut, which is commonly used for sandwich calorimeters.

At the end of each event, the `SteppingAction` controls the storing of the event. If certain conditions are met, the event is passed to the `AnalysisManager` class. Most often these conditions include a start hit, no veto hits and energy depositions in the fiber tracker and calorimeter.

5.4.2 SimulatedData and MeasuredData

The two classes described in this section are not derived from Geant4. Instead, they act as a data storage environment and format chosen for the predecessor setup

[3]Each physical volume may be retrieved by its name, which is a parameter of string type.

continued to be used for the present detector simulation. As mentioned in section 5.4.1, relevant data is stored for post-simulation analysis on an event-by-event basis. There are basically two different kinds of data objects, which are stored in the `MeasuredData` and `SimulatedData` classes:

1. Data comparable to real measured data in the experiment, like energy depositions and time-of-flights without the knowledge of its causative particle. This data is stored in the `MeasuredData` class.
2. Further information containing the MC truth, such as particle species for energy depositions or the occurrence of nuclear events in the target. Data of this character is used to evaluate the detection layout or to train the analysis and develop suitable cuts. It is stored in the `SimulatedData` class.

Both classes implement specific STL[4] data container types for simulation data.

The ROOT data analysis framework developed at CERN provides the ROOT Tree environment, which was designed to store large quantities of same-class objects [The07]. The Tree structure may contain integers, real numbers, STL data containers or even ROOT objects and is filled with simulation data at the end of each event. An example is the energy deposition per path length $\mathrm{d}E/\mathrm{d}x$, which is stored in a STL map individually for each detection component. Afterwards, the energy deposition can be retrieved by reading the volume name of the specific detector saved in the map together with its energy deposition. Because the present data acquisition (DAQ) implements the ROOT Tree format too, the reconstruction framework presented in chapter 7 is capable of reading measured data.

5.5 Geant4 versioning and data accumulation

As new versions of the Geant4 code are continuously released every year, physics may slightly change between different versions. In order to ensure consistent results, all results presented in chapter 6 and 7 are obtained using version 9.4.p04 of the toolkit and the corresponding physics models implemented in that version. The suffix "p04" labels the patch number to the actual version. Patches contain bug fixes and it is recommended to apply the latest one to the version in use.

The execution of a Geant4 application can either be accomplished locally, i.e. on the user's desktop PC, or the computing cluster of the physics institutes may be used to gain higher statistics. Therefore, the high throughput computing tool *Condor* is

[4] *Standard Template Library*, a C++ software library.

installed on the cluster. Condor is a workload management system for compute-intensive jobs and provides a queuing mechanism, which manages the execution and completion of parallel jobs submitted by the user [Con]. In order to gain enough statistics, condor is used for the analyses presented in this thesis.

One category of the Geant4 toolkit is Visualization (see section 2.9.3), for example for post-event investigation of geometries and trajectories. Event displays or detector layouts presented in this thesis are produced using the HepRApp viewer and the DAWN event display. By selecting one of these viewers in the initialization state of the Geant4 application, Geant4 will produce a specific file (.heprep or .prim) holding all information of the run, which can be used after program completion with the corresponding viewer.

Chapter 6

Simulation results of the detector concept evaluation

The results of the Geant4 simulation of the TOF spectrometer regarding the validation of the experimental setup are discussed in this chapter. On the one hand, the simulation of the predecessor layout [Grü11] is modified to evaluate its behaviour and to investigate the layout of the newly designed detection setup during its planning phase. In this context, sections 6.1 and 6.2 address the effects of beam collimation and the angular distribution of target fragments.

On the other side, the simulation of the present setup finally serves to evaluate and adjust certain structural components, like target thickness or size of the BGO calorimeter. These results are discussed in sections 6.3 to 6.5.

6.1 Effects of beam collimation

In order to investigate the effects of beam collimation and to be more closely in tune with the real situation, the implementation of a collimator into the existing detector simulation of the predecessor setup (see figure A.1) is performed and its effect on statistics of correct and unwanted stop detector hits is investigated.

A steel foil separates the vacua of the accelerator beam tube of COSY at the Forschungszentrum Jülich and the vacuum chamber of the TOF spectrometer. A collimator made of copper is placed upstream just in front of the steel foil in order to collimate the proton beam to a smaller width. The distance "center of collimator" – "front edge of detection chamber" has been roughly measured to 3.1 ± 0.1 m. The measures of the collimator are $50\,\text{mm} \times 80\,\text{mm} \times 80\,\text{mm}$ and the diameter of the collimator hole amounts to 5 mm. Both components, the steel foil and the collimator are implemented into the `DetectorConstruction`. A graphical representation obtained

from the simulation can be found in figure 6.1.

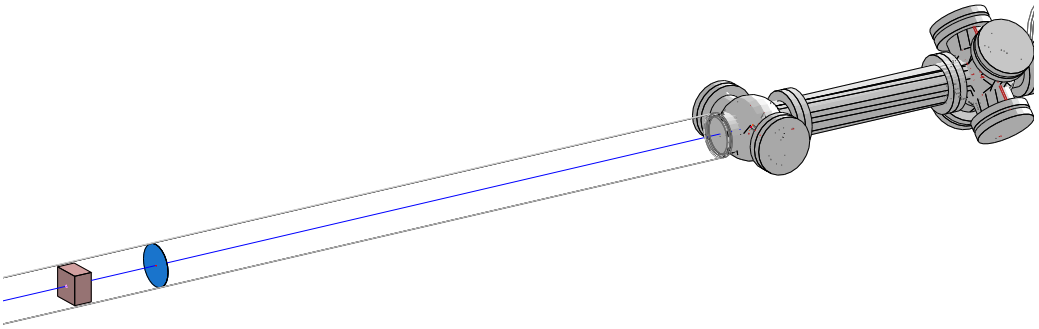

Fig. 6.1: Geant4 model representing the simulated accelerator vacuum tube housing the collimator (brown) and the steel foil (blue). On the right edge of the picture the vacuum tube holding start and veto detectors can be seen.

One can follow the particle's trajectories up to the vacuum chamber holding the scintillation detectors by zooming out of the detection setup. This is shown in figure 6.2 and reveals a possible background on the detectors originating from particles scattered by the collimator material. This leads to the question of whether a part of these events may lead to a misinterpretation as a correct event, because no shielding was used so far to shield scattered particles.

The simulation code of the predecessor detection setup [Grü11] has been extended, so that an analysis of detector events divided into *unwanted* and *correct* events can be realized. The event classifications are made up of combinations of specific detector hits:

Start detector hit: A primary proton passes the collimator, hits the start detector and initiates the TOF measurement.
$\rightarrow \text{Start}_{\text{hit}}$

Veto detector hit: A particle hits one of the two veto detectors. This may happen if a reaction occurs in the start detector or the particle is scattered by the start detector. The information can be used to discard the corresponding events in the final analysis.
$\rightarrow \text{Veto}_{\text{hit}}$

Target hit: The primary proton impinges on the target and possibly triggers a nuclear reaction.
$\rightarrow \text{Target}_{\text{hit}}$

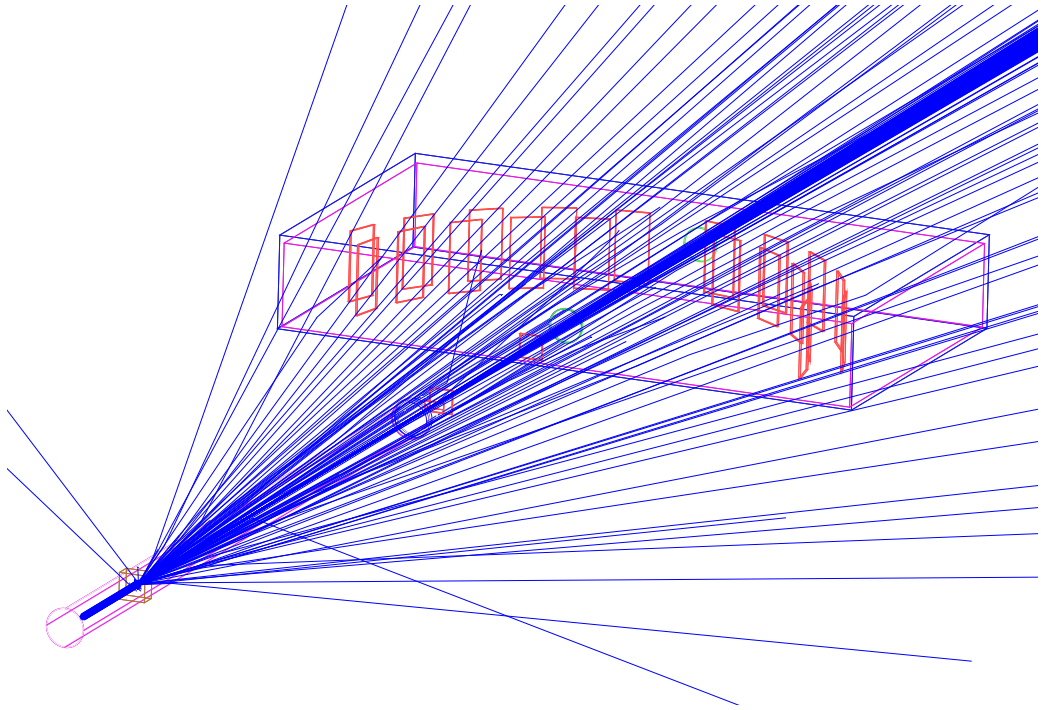

Fig. 6.2: Trajectories of 1000 primary protons and total view of the predecessor TOF spectrometer setup. Detectors are shown in red, the entry and exit windows of the chamber are drawn in green colour.

Stop detector hit: One of the 20 stop detectors in the detection chamber registers a particle hit and terminates the TOF measurement.
$\rightarrow \mathrm{Stop}_{\mathrm{hit}}$

These hit categories lead to the definition of unwanted and correct events:

- unwanted events are events with signals on start and stop detector(s), but no veto and no target hit:
  $\mathrm{Start}_{\mathrm{hit}} \wedge (\neg\mathrm{Veto}_{\mathrm{hit}}) \wedge (\neg\mathrm{Target}_{\mathrm{hit}}) \wedge \mathrm{Stop}_{\mathrm{hit}}$
- correct events are events with signals on start and stop detector(s) triggered by a target fragment, but no veto hit:
  $\mathrm{Start}_{\mathrm{hit}} \wedge (\neg\mathrm{Veto}_{\mathrm{hit}}) \wedge \mathrm{Target}_{\mathrm{hit}} \wedge \mathrm{Stop}_{\mathrm{hit}}$

Figure 6.3 provides examples for both cases.

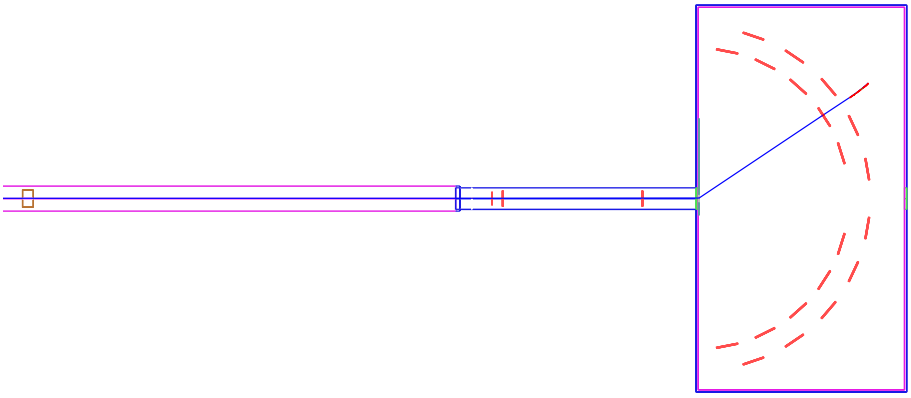

(a) correct event

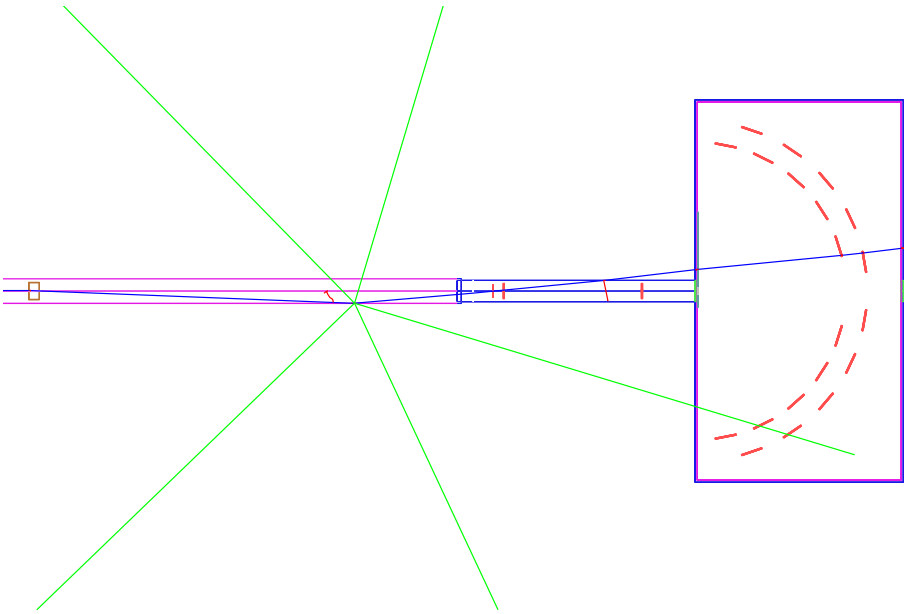

(b) unwanted event

Fig. 6.3: Detector visualizations showing a correct event (a) and an unwanted event (b). In the latter case, the primary proton was scattered by the collimator and the accelerator beam tube, hit the start detector and passed both vetos before crossing the vacuum tube and finally hitting two stop detectors.

Specific boolean data types implemented in the `SteppingAction` are switched (from *false* to *true*) once a particle hits a detection component. An analysis of these variables allows for a classification of events. In addition, the `G4Track` class provides a variety of member functions returning "current" information of the particle (e.g. momentum, position, kinetic energy, etc.), which can be used to classify an event. An example would be the query for the creation process of a particle via `GetCreator-Process()`, which returns a process name, e.g. "ionInelastic" in the case of a nuclear reaction.

Results

In figure 6.4 the abundances of different event classifications are shown. The total amount of simulated events is 10^7.

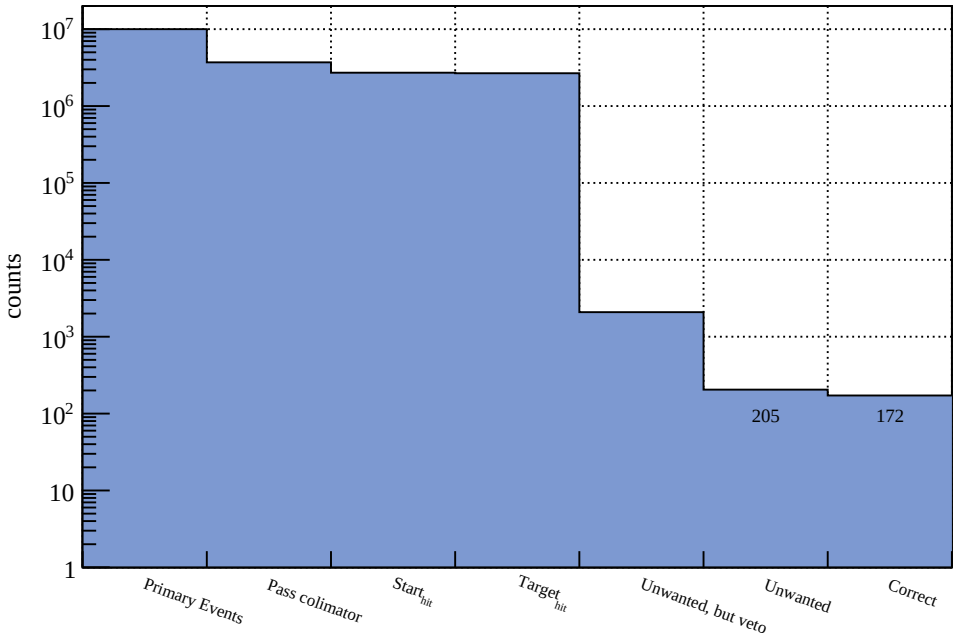

Fig. 6.4: Count rates of various event classifications. The rates for unwanted and correct events are explicitly written into the corresponding bin.

Only 27 % of generated primary particles hit the start detector. A large proportion (98 %) of these events hits the target as well. However, a very small number of these particles undergo a nuclear reaction in the target as can be estimated by the small number of correct events $n_{\mathrm{cor}} = 172 \pm 13$ compared to the number of primaries hitting the target. Most of the particles exit the detector chamber by passing the exit window on the back panel of the chamber (see figure 6.2). Compared to the

number of unwanted events $n_{\mathrm{unw}} = 205 \pm 14$, this finding strengthens the initial idea that the interaction of particles with the collimator material may lead to unwanted effects when no shielding is used.

The structure of the current TOF spectrometer concerning the positioning of start and veto detectors and the target is basically the same. As a result, a shielding for the current TOF spectrometer is definitely planned. The design and evaluation of several prototypes has already been addressed in the course of a bachelor thesis, for a detailed analysis see [GDR12].

6.2 Angular distribution of target fragments

The required size of the detection chamber and the solid angle to be covered by the detectors in the new setup can be estimated in advance by analyzing the angular distribution of target fragments. Therefore, the corresponding classes of the simulation of the predecessor setup are adjusted to inspect these quantities in the case of inverse kinematics.

Once a target fragment hits the vacuum chamber, its position and kinetic energy is stored in the `SimulatedData` class for post-simulation analysis and the track is immediately killed afterwards to save CPU time. For this analysis, the 20 stop scintillators (see figure A.1) are removed from the simulation.

Results

Figures 6.5(a)–6.5(d) show the correlation of azimuth angles (y-axis) and kinetic energies (x-axis) of selected particles, namely protons, alpha particles, ^{11}B-ions and ^{11}C-ions.

The angular distribution gets narrower the heavier the particles are, which can be seen by comparing the RMS values of the angular distributions: $\mathrm{RMS}_{\mathrm{proton}} = 9.422$, $\mathrm{RMS}_{\alpha} = 3.661$, $\mathrm{RMS}_{\mathrm{B11}} = 1.818$ and $\mathrm{RMS}_{\mathrm{C11}} = 1.894$. It is notable that the RMS for the fragments ^{11}B and ^{11}C is approximately the same. This is also true for the kinetic energies and their RMS.

A projection on the energy axis of the correlation plot 6.5(a) is shown in figure 6.6 showing a larger accumulation of protons carrying very small kinetic energies besides the peak centered around 175 MeV. The angular distribution flattens out and becomes wider towards lower energies, which is basically not the case for heavier fragments: For comparison, the projection of the correlation plot of ^{11}B-ions is shown in figure 6.7.

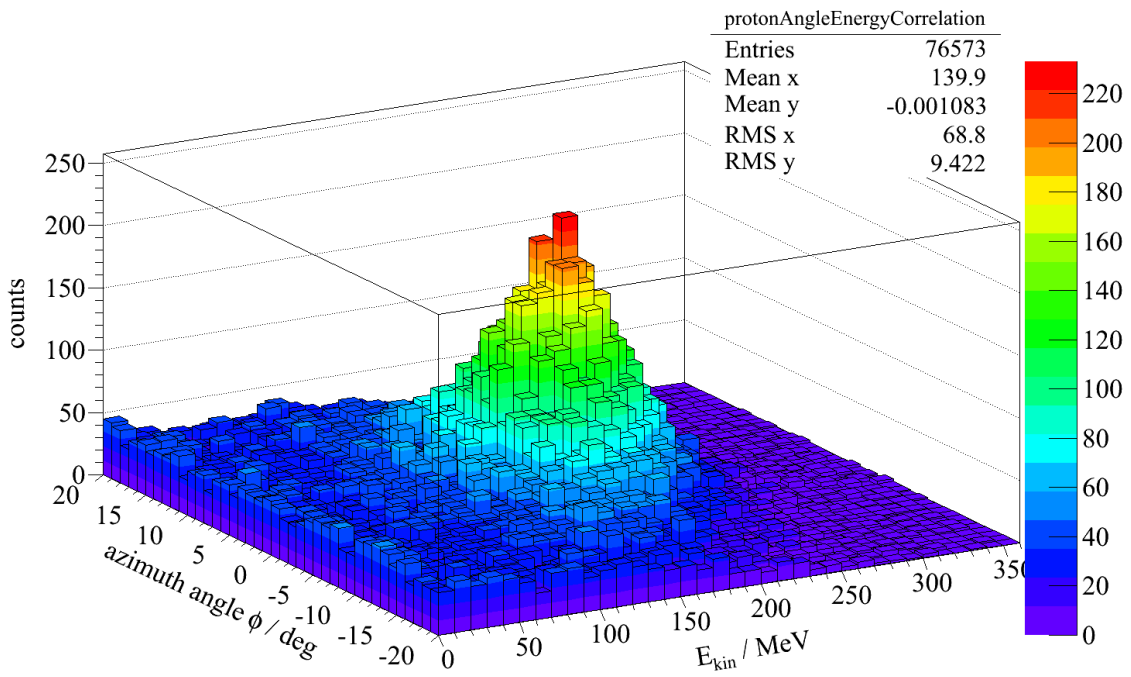

(a) protons

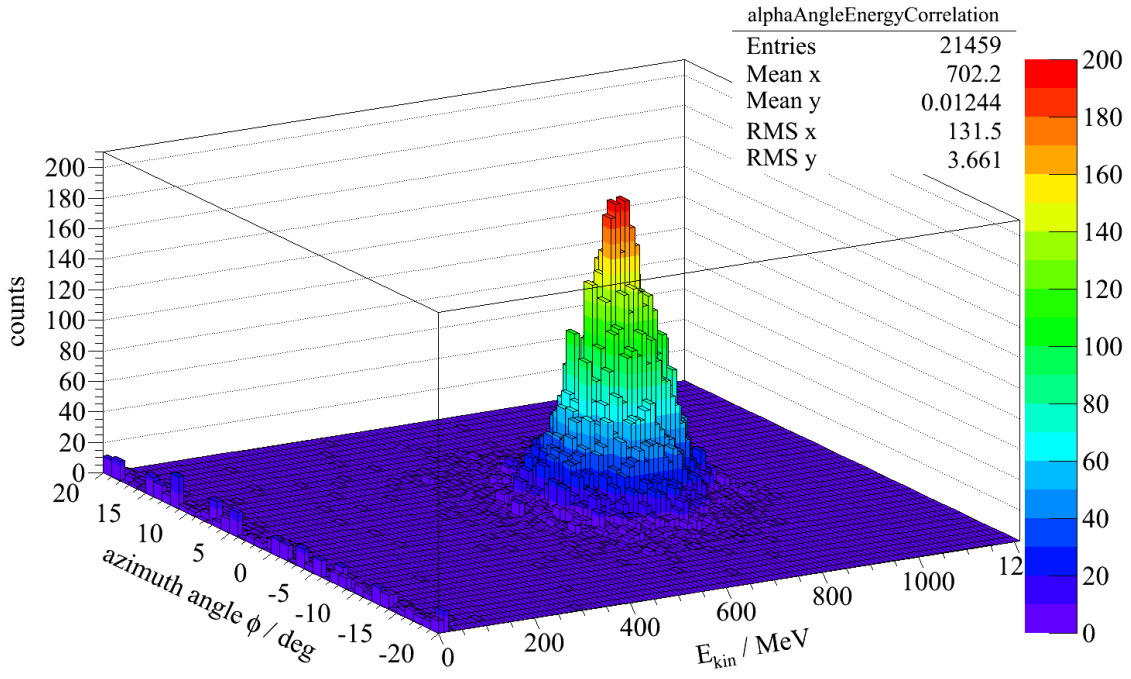

(b) alpha particles

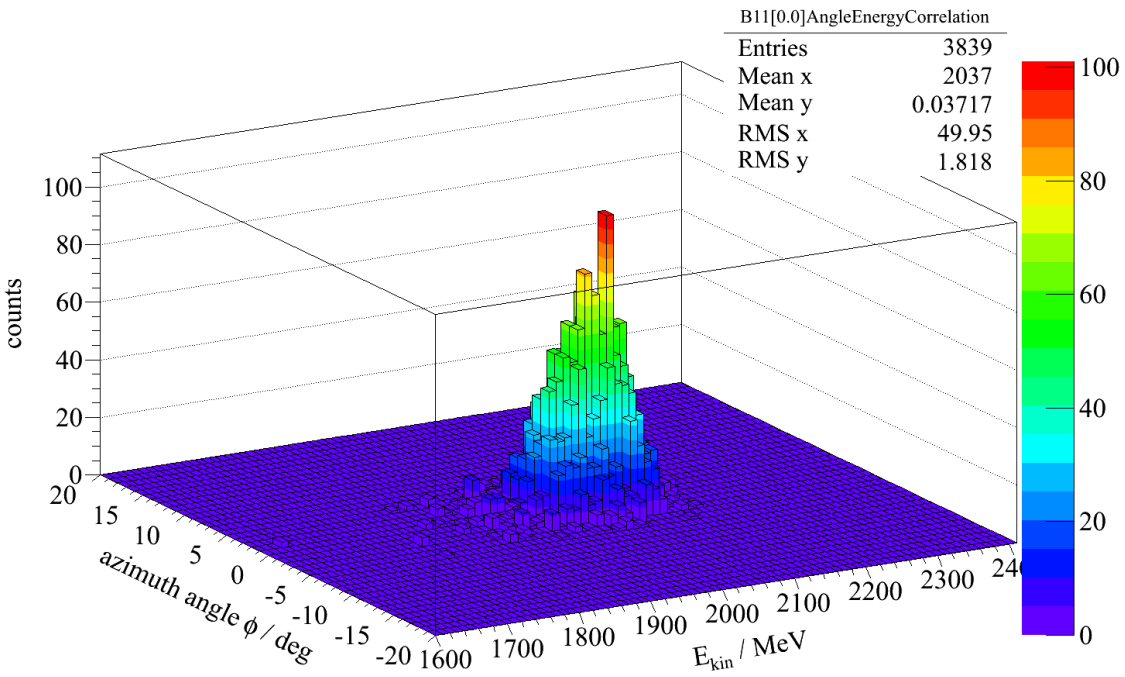

(c) ^{11}B-ions

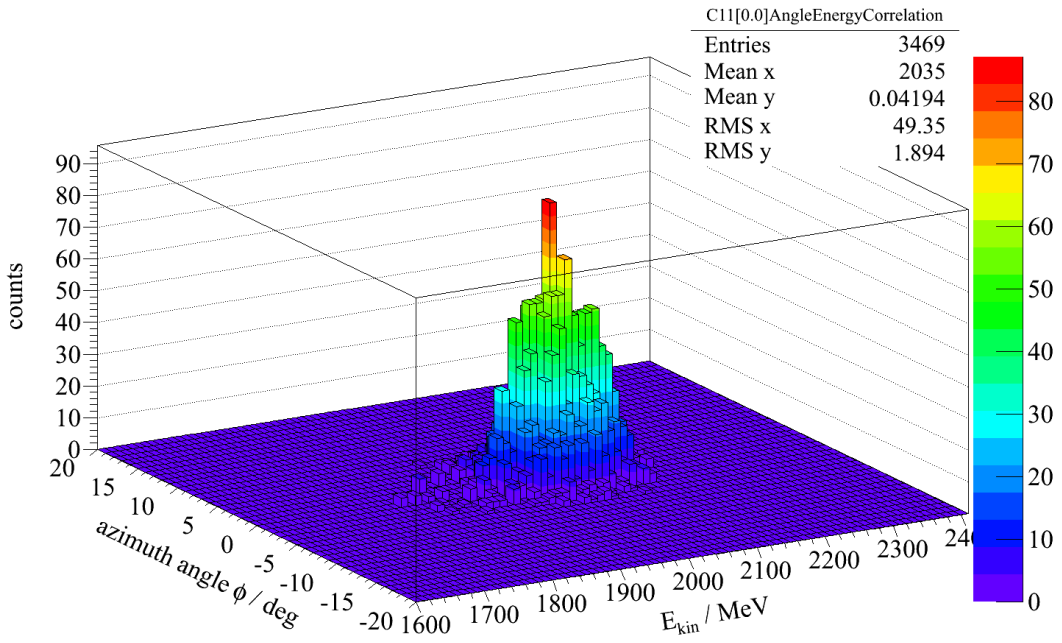

(d) ^{11}C-ions

Fig. 6.5: Correlation of azimuth angle ϕ and kinetic energy E_{kin} of target fragments.

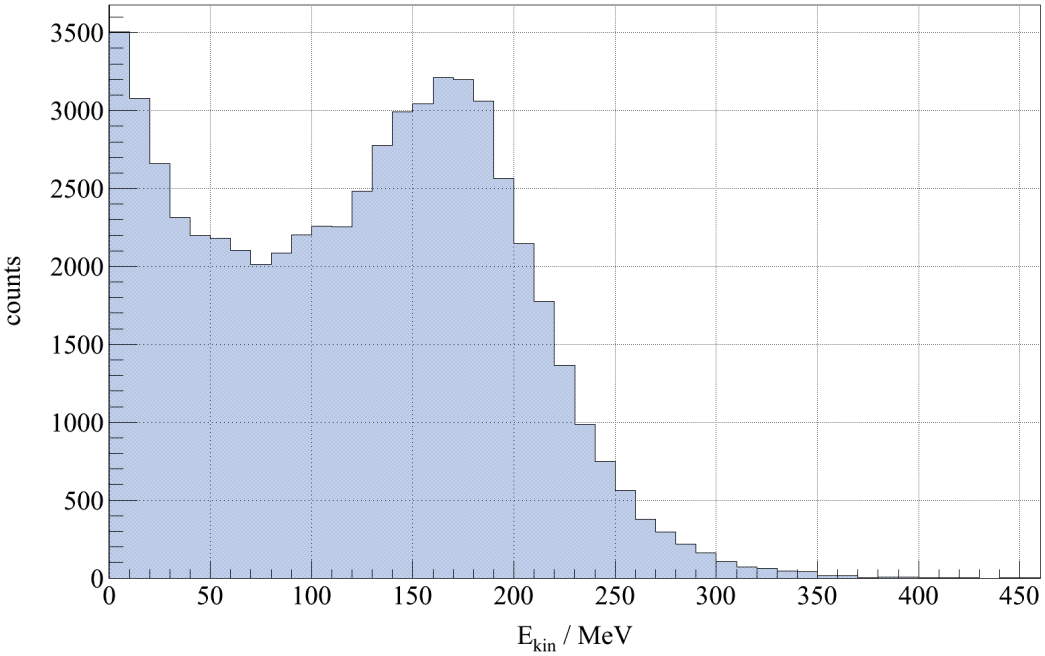

Fig. 6.6: Projection of azimuth angles on the energy axis of the proton correlation plot shown in figure 6.5(a).

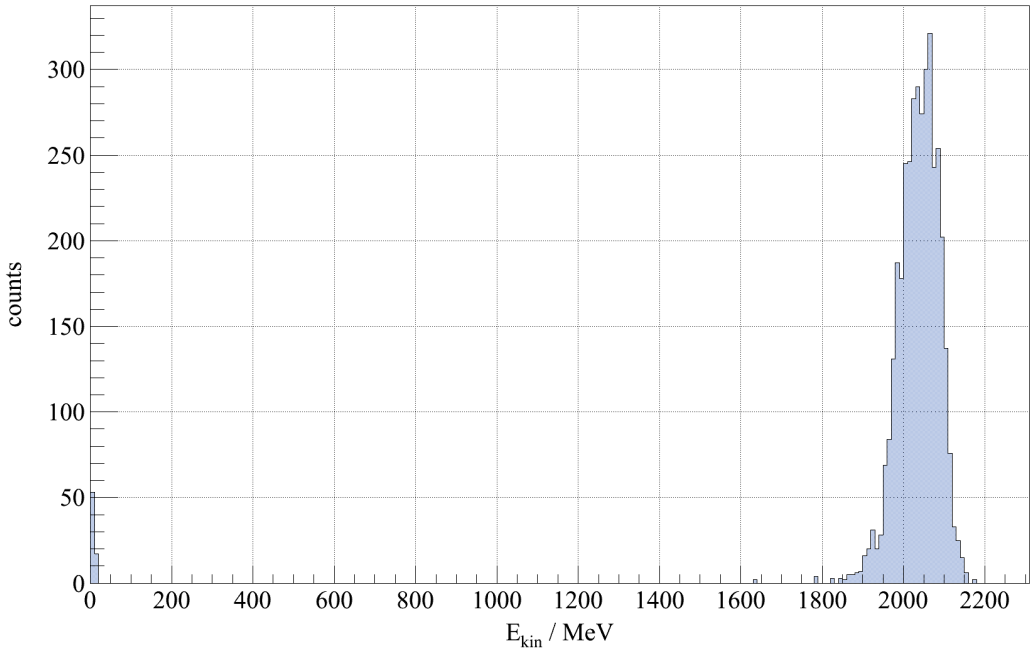

Fig. 6.7: Projection of azimuth angles on the energy axis of the ^{11}B correlation plot shown in figure 6.5 (c).

As a result, this circumstance raises the question to what extent a full event reconstruction is impaired by not detecting slow protons or other light particles. Nevertheless, the reconstruction of some reaction channels is not dependent on detecting light particles, for example the two most frequent reaction channels analyzed in section 7.9 and 7.10.

6.3 Influence of target thickness

A 0.075 mm thick target was used during last beam time in 2011 for the final measurement with the old detection layout. It is assumed that the influence of target thickness on momentum direction and energy loss of target fragments is less significant in inverse kinematics due to higher energies of primary particles. Nevertheless, this issue will be investigated for three different target thicknesses of 0.075 mm, 1 mm and 10 mm now using the simulation of the new detector layout (see figure 4.3).

6.3.1 Change of momentum direction

The momentum direction of each target fragment is saved to investigate the influence of target thickness for the different thicknesses mentioned above. In so doing, the angle $\Delta\theta$ between the vertex momentum direction vector $\boldsymbol{p}_{\text{vertex}}$ and the momentum direction vector at the exit of the target $\boldsymbol{p}_{\text{exit}}$ is calculated afterwards via

$$\Delta\theta = \arccos\left(\frac{\boldsymbol{p}_{\text{vertex}} \cdot \boldsymbol{p}_{\text{exit}}}{|\boldsymbol{p}_{\text{vertex}}| \cdot |\boldsymbol{p}_{\text{exit}}|}\right) \ . \tag{6.1}$$

Results

The angular deviations $\Delta\theta$ can be found in figure 6.8. On the x-axis, the angle $\Delta\theta$ is shown. The number of particles with angular deviations smaller than a specific $\Delta\theta$ normalized to the total amount of particles passing the target can be found on the y-axis.

As expected, the thicker targets have stronger influence on momentum direction. For example, a deviation of 0.5° or less is experienced by roughly 95 %, 90 % and 85 % of all fragments for corresponding target thicknesses of 0.075 mm, 1 mm and a 10 mm. This also means that only a slight amount of particles feature greater angular deviations between vertex and target exit points.

However, the deviations are smaller than in the predecessor setup (see [Grü11]) and it must be kept in mind that the present detector covers a much smaller solid

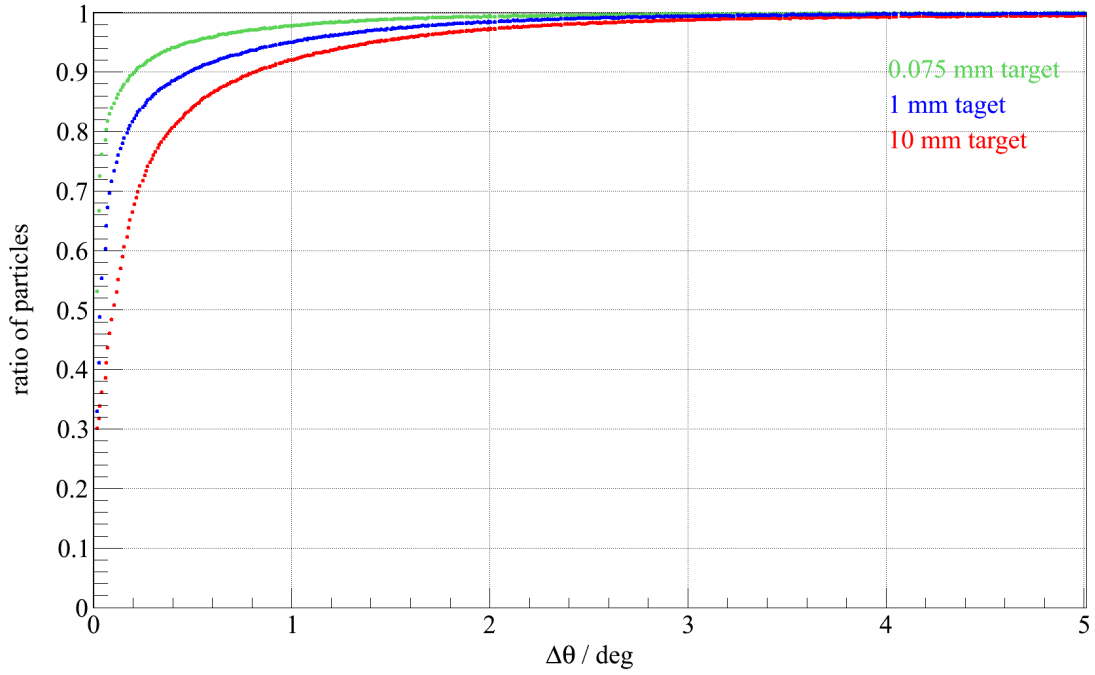

Fig. 6.8: Cumulative angular deviation of momentum direction between vertex and target exit position of target fragments for different target thicknesses. For a given deviation $\Delta\theta$, the fraction of particles with deviations smaller than $\Delta\theta$ are plotted against $\Delta\theta$. For example, 90 % of all particles deviate not more than 0.5° in the case of the 1 mm target.

angle and hence deviations have stronger effect on detection efficiencies.

6.3.2 Influence on energy loss

In order to study the influence of target thickness on energy loss, the difference of kinetic energies at vertex E_{vertex} and target exit E_{exit} normalised to the vertex kinetic energy

$$\Delta E = \frac{E_{\text{vertex}} - E_{\text{exit}}}{E_{\text{vertex}}} \tag{6.2}$$

is considered.

Results

The results are shown in figure 6.9, where the deviation ΔE is drawn on the x-axis. The number of particles with angular deviations smaller than a specific ΔE normalized to the total amount of particles passing the target can be found on the y-axis.

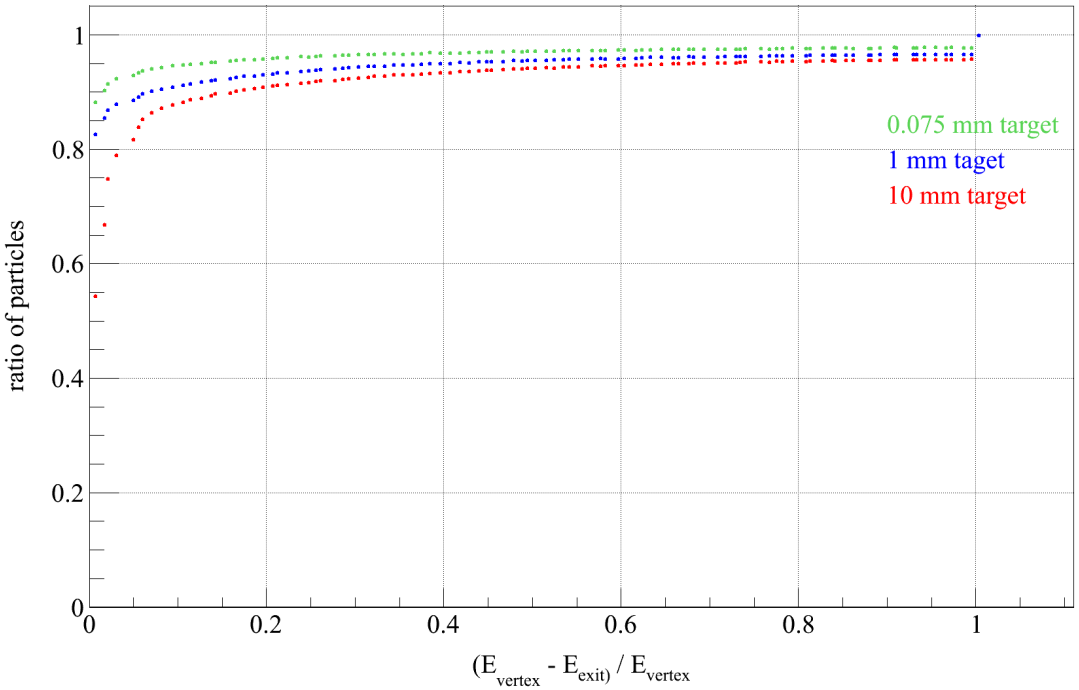

Fig. 6.9: Difference ΔE of vertex kinetic energy E_{vertex} and kinetic energy at target exit point E_{exit} of target fragments normalised to E_{vertex}. For a given ΔE the fraction of particles with differences smaller than ΔE are plotted against ΔE. For example, the kinetic energy E_{exit} of 90 % of all particles deviate by as much as 20 % from E_{vertex} in the case of the 10 mm target.

Also in the case of energy loss, thicker targets have stronger influence on energy loss of target fragments. A maximum deviation of 10 %, for example, is experienced by 95 %, 90 % and 87 % of all target fragments for the corresponding target thicknesses of 0.075 mm, 1 mm and a 10 mm. According to the Bethe formula (see equation 5.4), thicker targets lead to longer path lengths in the target material and hence more energy is lost.

From about 10 % of energy loss the gradient of each curve becomes less steep, which means that the majority of particles loses only a slight amount of their kinetic energy. Furthermore, the data points for highest values of ΔE of all three curves overlap after a value leap on the y-axis (only the blue dot for the 1 mm target can be seen). These overlapping data points belong to particles which finally lose all their energy within the target.

The influence on energy loss of the targets investigated in this analysis is in the same order of magnitude and hence comparable. The advantage of using a thicker target is a higher rate of target fragments, because the probability of nuclear reactions increases. It is therefore recommended to use thicker targets in inverse kinematics.

6.4 Energy loss in fiber tracker

Measurements with the fiber tracker provide information on the $\mathrm{d}E/\mathrm{d}x$ and TOF of particles. The minimum and maximum values of energy loss may also be used to gain information about the necessary pixel size of SiPM for the final setup, since the number of pixels on each SiPM determines the dynamic range[1] for the $\mathrm{d}E/\mathrm{d}x$ measurement.

Therefore, a simulation of an irradiation of the fiber tracker with a radioactive ^{90}Sr source is carried out and compared to measurements in section 6.4.1. To get an estimate of the maximum energy deposition in the fiber tracker, the $\mathrm{d}E/\mathrm{d}x$ of primary ^{12}C-ions is discussed subsequently in section 6.4.2. Section 6.4.3 finally compares the energy loss distribution in the fiber tracker to that in the bar tracker.

6.4.1 Energy loss of ^{90}Sr decay products

The radioactive ^{90}Sr source is simulated 2 cm in front of a fiber tracker module. The decaying ^{90}Sr nucleus is set as the primary particle in the `PrimaryGeneratorAction` class and the energy deposition of the decay products in the fiber tracker is saved for post-simulation analysis. This source is available for measurements in the physics institute and results were compared to the simulated energy spectra by Ronja Lewke [Lew12].

Results

Figure 6.10 shows the energy spectrum in the fiber tracker module. The endpoint energy of the energy spectrum is determined to approximately 2000 keV. It has to be considered that a small amount of energy is lost before the decay products hit the fiber tracker.

The daughter nucleus ^{90}Y is radioactive too and decays into the stable isotope ^{90}Zr, thus figure 6.10 is a superposition of energy spectra of the decay chain $^{90}\mathrm{Sr} \rightarrow {}^{90}\mathrm{Y} \rightarrow {}^{90}\mathrm{Zr}$. Endpoints of ^{90}Sr and ^{90}Y spectra were determined to take values of 546 keV and 2280 keV [Cha]. The endpoint in the spectrum shown in figure 6.10 is therefore most likely compatible with ^{90}Y, whereas the 546 keV of ^{90}Sr is unidentifiable due to the superposition of both spectra.

The endpoint energy in the energy spectrum of simulated ^{90}Sr decay products can now be compared to measurements by Ronja Lewke [Lew12]: The resulting maximum

[1] This is the range where the number of triggered pixels is proportional to the number of incident photons.

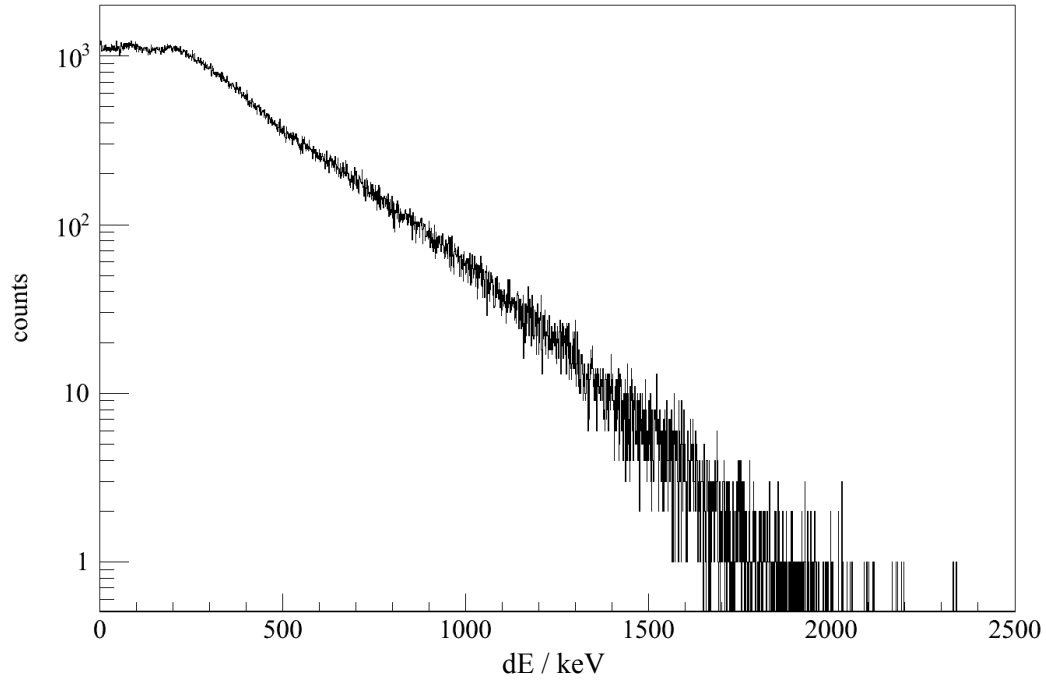

Fig. 6.10: Energy deposition in the fiber tracker originating from irradiation with a simulated ^{90}Sr source.

number of detected photons during irradiation with ^{90}Sr is 40 ± 2. On the other hand, the expected number of photons for the highest energy deposition of target fragments during beam time is needed in order to specify which pixel size is the most appropriate for the experiment.

6.4.2 Energy loss of target fragments

In this context, the energy deposition for each particle type is saved in separate histograms. Attention is given especially to protons and (primary) ^{12}C-ions, because these are the particles with smallest and highest energy deposition in the fiber tracker.

Results

The $\mathrm{d}E/\mathrm{d}x$ distribution for protons and ^{12}C-ions are shown in figures 6.11(a) and 6.11(b). The energy deposition ranges from about $(0.2-0.4)\,\mathrm{MeV}$ for protons to $(7.5-19.0)\,\mathrm{MeV}$ in the case of ^{12}C-ions. Especially heavier particles feature a broad energy distribution with three peaks. In figure 6.11(b), these peaks can be identified at energies of 8 MeV, 12.5 MeV and 17.5 MeV.

This is due to the fact that particles are crossing the fiber tracker on different path

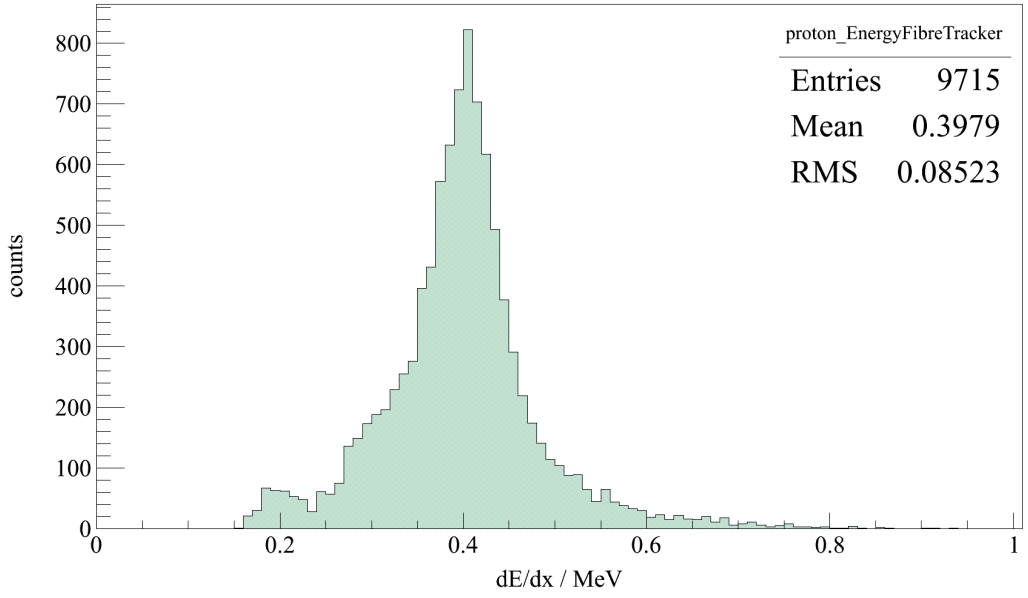

(a) protons

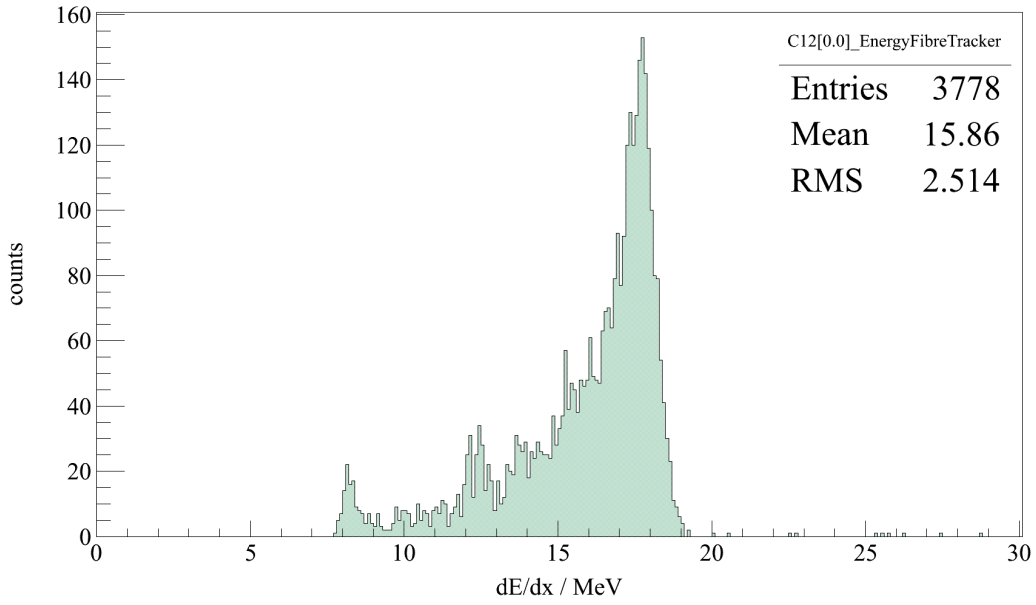

(b) ^{12}C-ions

Fig. 6.11: Energy deposition of protons (a) and ^{12}C-ions (b) in the fiber tracker.

lengths leading to a variable number of fibers that are hit. As depicted in figure 6.12, it may occur that a particle crosses only two fibers leading to a path length l_{X} and therefore to an energy deposition corresponding to the peak at lowest $\mathrm{d}E/\mathrm{d}x$ in figure 6.11(b). On the other hand, particles crossing three fibers deposit more energy

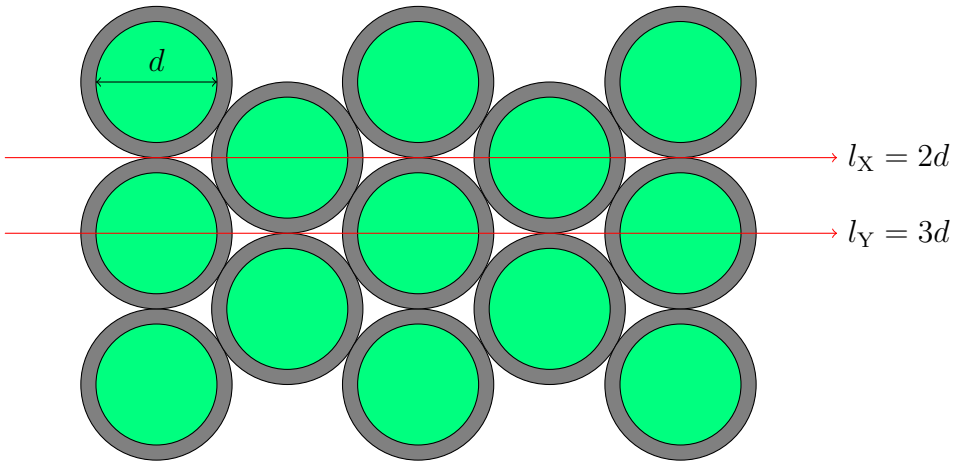

Fig. 6.12: Detailed view of the horizontal fiber tracker illustrating the path length dependence of energy deposition. For simplicity, two straight trajectories are shown hitting two or three fibers and thus leading to path lengths l_X and l_Y.

on their path length l_Y and thus giving rise to the formation of the middle peak. In between, a maximum path length is reached explaining the highest energy peak.

The results of this analysis and the one presented in the foregoing section allow to calculate the expected number of registered photons by linear scaling and taking the different photon detection efficiencies for various SiPM candidates into account to make an appropriate choice for the SiPM to be used for the fiber tracker. This was done by Ronja Lewke and SiPM of type S10362-11-025 manufactured by Hamamatsu were chosen [Lew12].

6.4.3 Test of detection devices of rectangular shape

A broad ($\mathrm{d}E/\mathrm{d}x$) distribution generally causes difficulties concerning the correct identification of particles, which is the topic of the next chapter. Besides the fiber tracker, one of the first approaches in the design of the current setup was to additionally use a bar tracker (see figure 4.5) for the $\mathrm{d}E/\mathrm{d}x$ and TOF measurement. Due to its rectangular shape, the bar tracker features the distinct advantage of better defined path lengths.

In order to compare the energy loss distributions of the fiber tracker to other detection devices, three simulations are carried out: (1) the fiber tracker as shown in figure 6.12, (2) the bar tracker and (3) a rectangular monolithic box with dimensions of fibre tracker, henceforth called “dummy” fiber tracker.

Results

The energy depositions of ^{12}C-ions in the fiber tracker and the dummy fiber tracker are shown in figure 6.13.

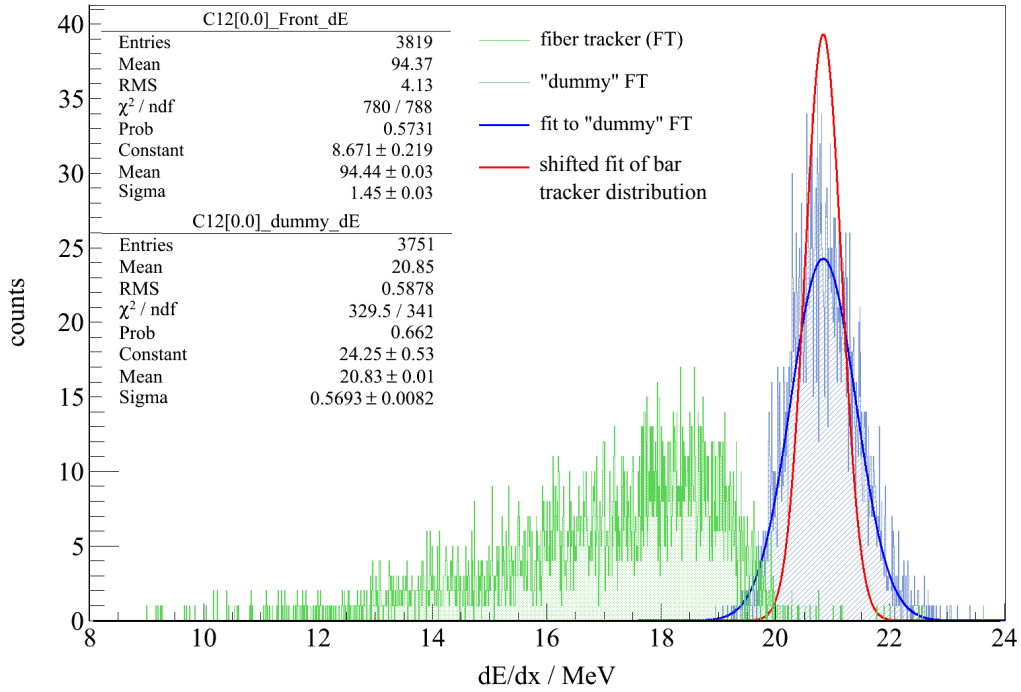

Fig. 6.13: Energy deposition $\mathrm{d}E/\mathrm{d}x$ of ^{12}C-ions in the fiber tracker and a 1 mm thick dummy volume. The gaussian fit to the dummy fiber tracker is compared to the shifted fit of the bar tracker distribution.

As might be expected, the energy deposition in the dummy fiber tracker is narrower and shifted towards higher energies due to longer path lengths. Its distribution can be described by a gaussian fit. The simulation of the bar tracker is used to compare its width and hence its resolution to that of the dummy fiber tracker. For reasons of clarity, its energy deposition is not shown in figure 6.13, because it is shifted to relatively high energies. Instead, the gaussian fit of its distribution is shifted to the position of the dummy fiber tracker keeping the relative width constant.

In conclusion, the bar tracker performs best due to higher energy depositions. Nevertheless, it has to be kept in mind that an edge length of 5 mm might be too thick for an adequate spatial resolution. Therefore, the fiber tracker is chosen as the detection device for $\mathrm{d}E/\mathrm{d}x$ and TOF measurements in the final analysis.

6.5 Calorimeter evaluation

The results discussed in section 6.2 led to the design of the current detection setup presented in section 4.3. As was concluded, especially lighter particles feature a broadened angular distribution when going to smaller kinetic energies. Basically, there is the option of extending the calorimeter by using more than 16 BGO crystals.

In order to study the effect of calorimeter expansion, the BGO crystals in the simulation are replaced by a circular dummy volume with a diameter of 30 cm, which narrowly fits into the detection chamber. The polar and azimuth angle of each particle originating from a nuclear interaction in the target and subsequently hitting the dummy calorimeter are stored.

Results

Figure 6.14 shows the results of 10^7 simulated events. The polar angle θ is plotted on the x-axis, whereas the azimuth angle ϕ can be found on the y-axis.

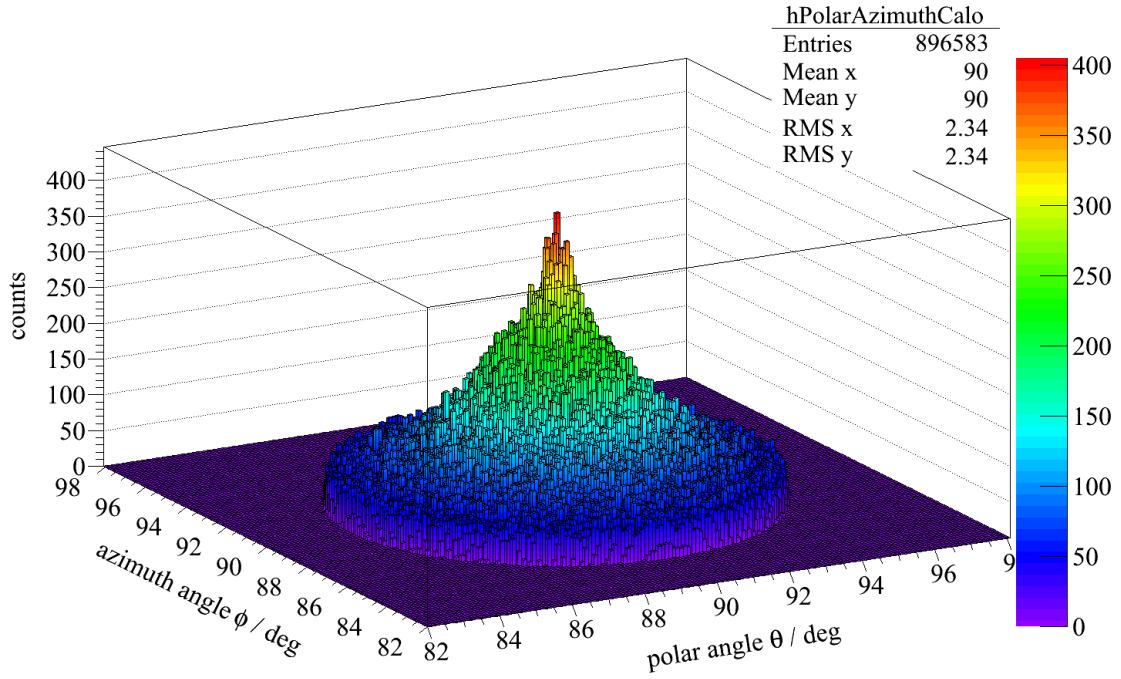

Fig. 6.14: Polar and azimuth angles of particles resulting from nuclear reactions in the target and hitting the dummy calorimeter volume.

The angular distribution of target fragments is isotropic around the beam axis (90° in both directions). In order to get an estimate of the angular range to be covered to detect a certain fraction of fragments, the number of particles within a specific

angular range has to be summed up. Figure 6.15 illustrates the fraction of fragments inside the angular range denoted on the abscissa. A second scale (pictured in blue) provides information about the ratio as a measure of a distance from the beam axis.

As can be seen from the figure, the ratio of particles on the dummy calorimeter volume is dependent on the particle type. Detecting lighter particles, especially protons, still remains problematic in the current TOF setup due to the broad angular distribution shown in figure 6.5(a). For the current setup, only 20 % of all protons can be detected. On the other side, the detection efficiencies for heavier particles are better than the overall fraction of 40 % shown in figure 6.15. For ^{11}B and ^{12}C-ions they are around 65 % and 75 %.

In conclusion, the current setup with 16 BGO crystals is capable of detecting roughly 40 % of all target fragments. To detect 90 % of all target fragments, for example, an angle of 4.5° has to be covered. This means to create a structure of BGO crystals with a diameter of roughly 24 cm.

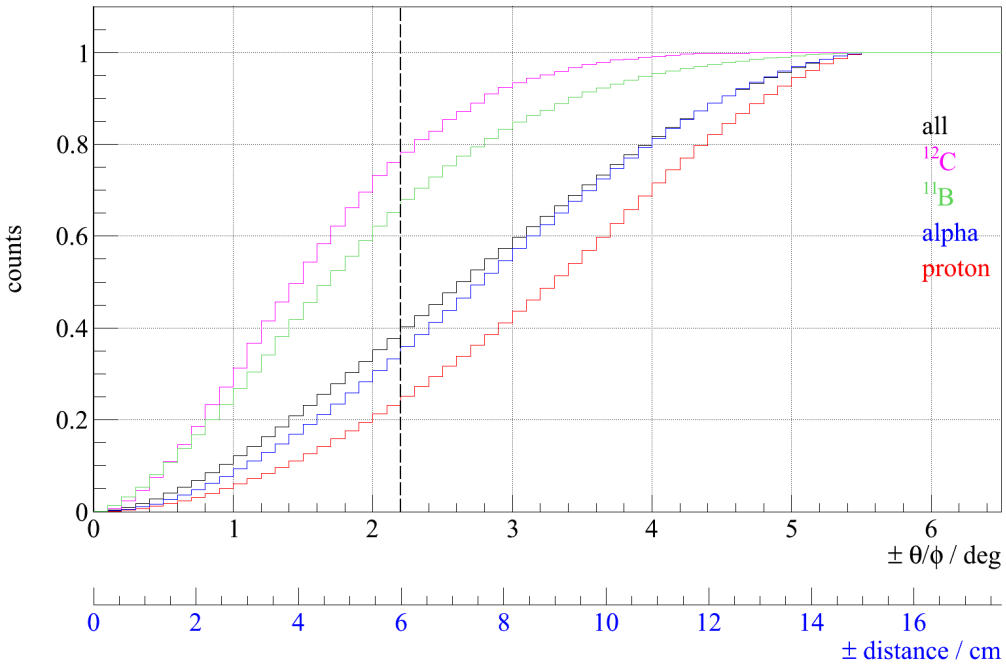

Fig. 6.15: Cumulative fraction of the number of particles within a certain angular range or distance to the center, respectively, to the total number of fragments detectable with the dummy calorimeter. The dashed line illustrates the current situation with 16 BGO crystals assuming an edge length of 2.4 cm for each crystal.

Chapter 7

Event identification results

One of the main tasks of this thesis is the development and validation of a reconstruction framework, which can be used either with simulation data or with measured data from one of the future beam times. In this context, the simulation data can be smeared, for example with a gaussian distribution, to take detector resolutions into account. The reconstruction code tries to correctly identify the target fragments which eventually enables full event reconstruction. The code is developed using the simulation data with the MC truth to verify particle identification. It is planned that the algorithm is used in the future to analyze measured data. The class philosophy of the newly designed reconstruction code is discussed in section 7.1.

The detection components already introduced in section 4.3 provide the required set of kinematic variables for a possible fragment identification, namely the measurement of the time-of-flight, the specific energy loss per path length $\mathrm{d}E/\mathrm{d}x$ and the total energy loss E_{tot}. These quantities are linked to the reconstructed kinematic variables introduced in section 7.2 in a way that a good match between them leads to the most likely particle type. Once all fragments, i.e. the event is reconstructed, a determination of a cross section is the final goal. Due to the lack of measured data, this can not be accomplished yet.

Before analyzing target fragments, a reconstruction of their trajectories has to be realized. The verification of track reconstruction, that means a comparison between reconstructed track position and true track position known from MC truth, can be found in section 7.3.

In view of the final evaluation of specific reaction channels to be discussed in section 7.9 and 7.10 (namely $^{12}\mathrm{C}(\mathrm{p},2\mathrm{p})^{11}\mathrm{B}$ and $^{12}\mathrm{C}(\mathrm{p},\mathrm{pn})^{11}\mathrm{C}$), preparatory analyses without target simulation and data smearing (section 7.5), without target simulation but data smearing (section 7.6 and 7.7) and the evaluation of final uncertainties (section 7.8) are realized.

The benefit of analyzing simulated data is the capability of checking the analysis results via MC truth and in this way developing an optimal set of cut parameters. The resolutions of each quantity entering the analysis must therefore closely reflect the real detector components.

7.1 Class philosophy

The structure of the reconstruction code is based upon the principle of object-oriented programming. Every subtask in the flow of the analysis is implemented in its own class. The basic scheme is shown in figure 7.1.

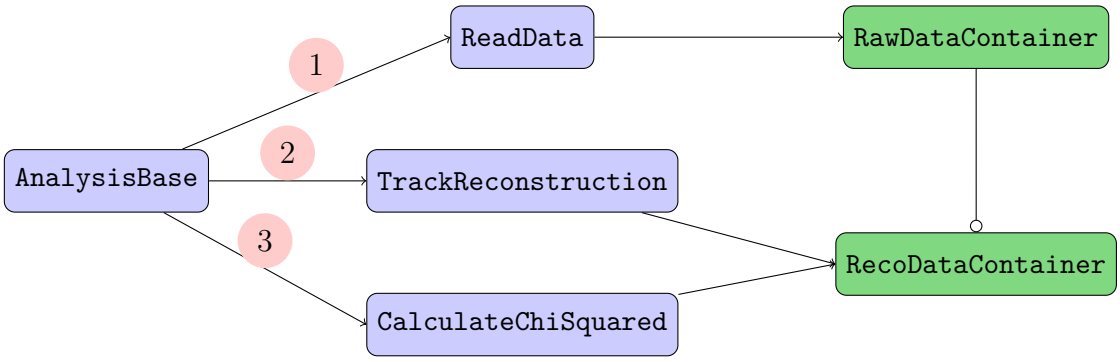

Fig. 7.1: Schematic illustration of the analysis and its flow towards χ^2-calculation showing analysis classes and dictionary classes.

The base class `AnalysisBase` steers the invocation of all other classes and finally fills the ROOT Tree storing the reconstruction results.

In the first step, the data, for example the energy depositions of all detectors, is read by the `ReadData` class and stored in the abovementioned tree. A ROOT dictionary class to the tree is needed in order to access tree objects within the C++ context. The dictionary contains the definition of tree variables and functions for Set/Get-interactions with the tree. This class is called `RawDataContainer`. The encapsulation of the `ReadData` class has the advantage that it can easily be modified for future data without affecting other parts of the code.

The task of the `TrackReconstruction` class is to find clusters of energy deposition in the fiber tracker and utilize the spatial information to extrapolate the particle's trajectory to the calorimeter to reconstruct full tracks.

Definition 1 (Full track) *A track is considered a full track, when the quantities* $\mathrm{d}E/\mathrm{d}x_\mathrm{h}$, $\mathrm{d}E/\mathrm{d}x_\mathrm{v}$, TOF_h, TOF_v *and* E_tot *are attributed to it and there is no other reconstructed track pointing to the same calorimeter crystal.*

The abbreviations “h” and “v” are used to distinguish between the “horizontal” and “vertical” fiber tracker modules.

After track reconstruction, each full track enters the χ^2-calculation in the `CalculateChiSquared` class, where the most likely particle type has to be found for each reconstructed track (the definition of χ^2 is introduced in equation (7.4)). Before χ^2-calculation, the tracks may be smeared taking detection resolutions into account. Every information generated for reconstruction purposes (for example full tracks and corresponding reconstructed Z and A) is stored in a separate branch of the tree. Its dictionary is the `RecoDataContainer` class, which inherits from `RawDataContainer` and facilitates a distinction between raw data and reconstructed data.

7.2 Determination of identification variables

Target fragments are characterized by their atomic number Z, mass A and kinetic energy E. As was explained in section 4.2, it needs three kinematic variables to enable particle identification. As a result, the time-of-flight, the specific energy loss per path length $\mathrm{d}E/\mathrm{d}x$ and the total energy loss E_{tot} are calculated and compared to their measured or simulated counterpart for each combination of Z, A and E in order to find the most likely particle.

In the reconstruction code, this is achieved by using nested C++ loops iterating over the loop variables Z, A and E. The kinematic variables are then calculated in the innermost loop. It should be stressed that the iteration is performed over physically meaningful pairs of Z and A only to save CPU time. In the following, the calculated variables are labeled by an index “calc”, whereas measured (or simulated) values can be identified by their index “meas”[1].

Total energy $\mathbf{E_{tot}}$ The value of the reconstructed total energy deposition $E_{\mathrm{tot,calc}}$ is set to the value of the loop variable E minus the energy loss in the fiber tracker, because the kinetic energy E of target fragments is lowered when they traverse the fiber tracker material. This means that $E_{\mathrm{tot,calc}}$ is basically dependent on E.

$$E_{\mathrm{tot,calc}}(E) \ . \tag{7.1}$$

Time-of-flight TOF The time-of-flight is calculated via $\mathrm{TOF}_{\mathrm{calc}} = d/v$, where $d = 1.5\,\mathrm{m}$ is the distance from the target to the fiber tracker and v is the velocity of

[1] In view of a future use with measured data, the index is called “meas” here. Until now, only simulated data is used to test the reconstruction code.

the particle determined using the relation $E = (\gamma - 1)mc^2$. This implies that $\mathrm{TOF}_{\mathrm{calc}}$ is dependent on A and E, since m is the mass of the target fragment:

$$\mathrm{TOF}_{\mathrm{calc}}(A,\, E)\ . \tag{7.2}$$

Energy loss dE/dx The restricted Bethe energy loss formula in equation (5.4) is applied to calculate the energy deposition within the fiber tracker. Because $\mathrm{d}E/\mathrm{d}x$ is proportional to $1/v$ and Z^2, it is dependent on Z, A and E:

$$\mathrm{d}E/\mathrm{d}x_{\mathrm{calc}}(Z,\, A,\, E)\ . \tag{7.3}$$

At the end of each iteration step the χ^2 for the current set of loop parameters is calculated according to

$$\chi^2 = \left(\frac{E_{\mathrm{tot,calc}} - E_{\mathrm{tot,meas}}}{\sigma_E}\right)^2 + \left(\frac{\mathrm{TOF}_{\mathrm{calc}} - \mathrm{TOF}_{\mathrm{meas}}}{\sigma_{\mathrm{TOF}}}\right)^2 + \left(\frac{\frac{\mathrm{d}E}{\mathrm{d}x}_{\mathrm{calc}} - \frac{\mathrm{d}E}{\mathrm{d}x}_{\mathrm{meas}}}{\sigma_{\frac{\mathrm{d}E}{\mathrm{d}x}}}\right)^2 . \tag{7.4}$$

The minimal χ^2-value finally leads to the most likely particle type.

Verification of kinematic variable reconstruction

In order to get a sense of whether the calculated kinematic variables are in good agreement with simulated or measured data, figure 7.2 shows the correlation of $\mathrm{d}E/\mathrm{d}x$ and TOF. According to equations (7.2) and (7.3), a correlation of TOF and $\mathrm{d}E/\mathrm{d}x$ should give information about the particle's charge Z, because it is the only free parameter.

As can be seen from the plot, theoretical predictions and data fit together very well and a distinction between particles with different Z seems possible. The horizontal line near 13.5 ns can be explained and originates from nuclear reactions in the detector itself. These fragments will subsequently hit a neighbouring detector and generate an event with $\mathrm{d}E/\mathrm{d}x$ and a TOF, which is approximately the same as the TOF of primary ions from start detector to the detector where the interaction occurred.

7.3 Track reconstruction

To verify the effectiveness of the track reconstruction code, the reconstructed tracks pointing to one of the BGO crystals are validated with the help of the MC truth.

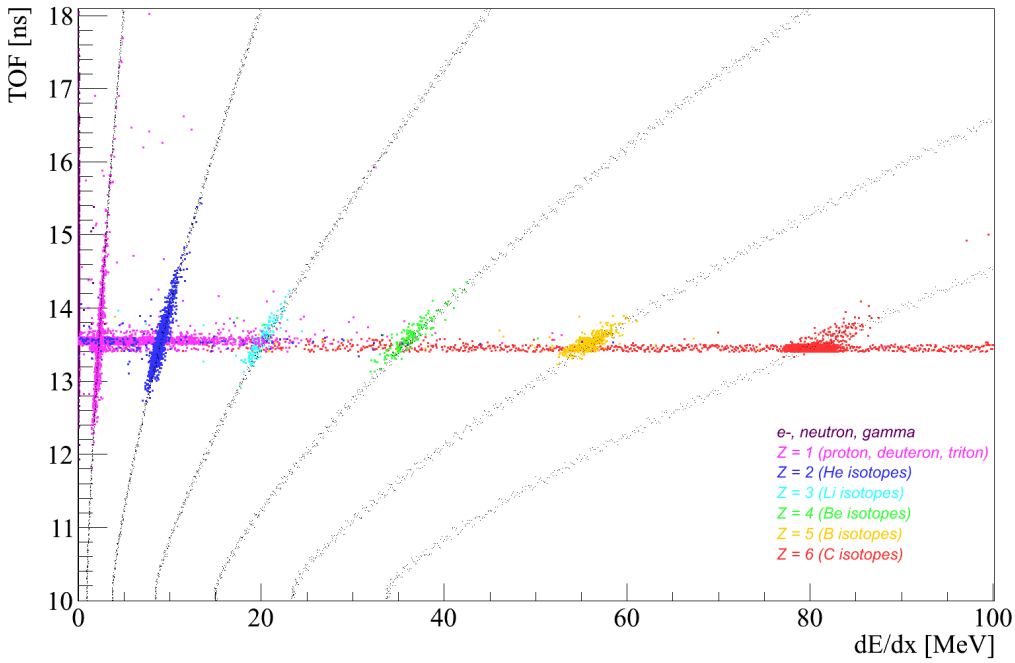

Fig. 7.2: Correlation of simulated TOF and $\mathrm{d}E/\mathrm{d}x$ for the bar tracker (coloured dots) and the corresponding theoretical predictions calculated analytically and used in the reconstruction code (black dots). The true identity of particle species is retrieved from MC truth.

First, the principle of track identification via reconstruction of energy clusters in the fiber tracker modules is presented in section 7.3.1. The spatial coordinates obtained in this way are used for a linear extrapolation to the calorimeter assuming a starting point in the center of the target in order to identify the crystals that are hit. Results of this position reconstruction are compared to the true impact points known from MC truth in section 7.3.2. Subsequently, the verification of crystal identification is presented in section 7.3.3.

7.3.1 Cluster reconstruction

A particle crossing the fiber tracker deposits a specific amount of its energy according to the Bethe formula (equation (5.4)) in a certain number of fibers. The information of which fibers or, in a further step, which SiPM are hit are used to reconstruct the particle's trajectory. On simulation level, the energy deposition per fiber is stored in specific STL containers. The `TrackReconstruction` class uses this information to reconstruct a cluster of fibers that are hit for each trajectory.

Assuming an event with several particles crossing a fiber tracker module, the fiber with the highest energy deposition (● in figure 7.3) is selected for the first cluster

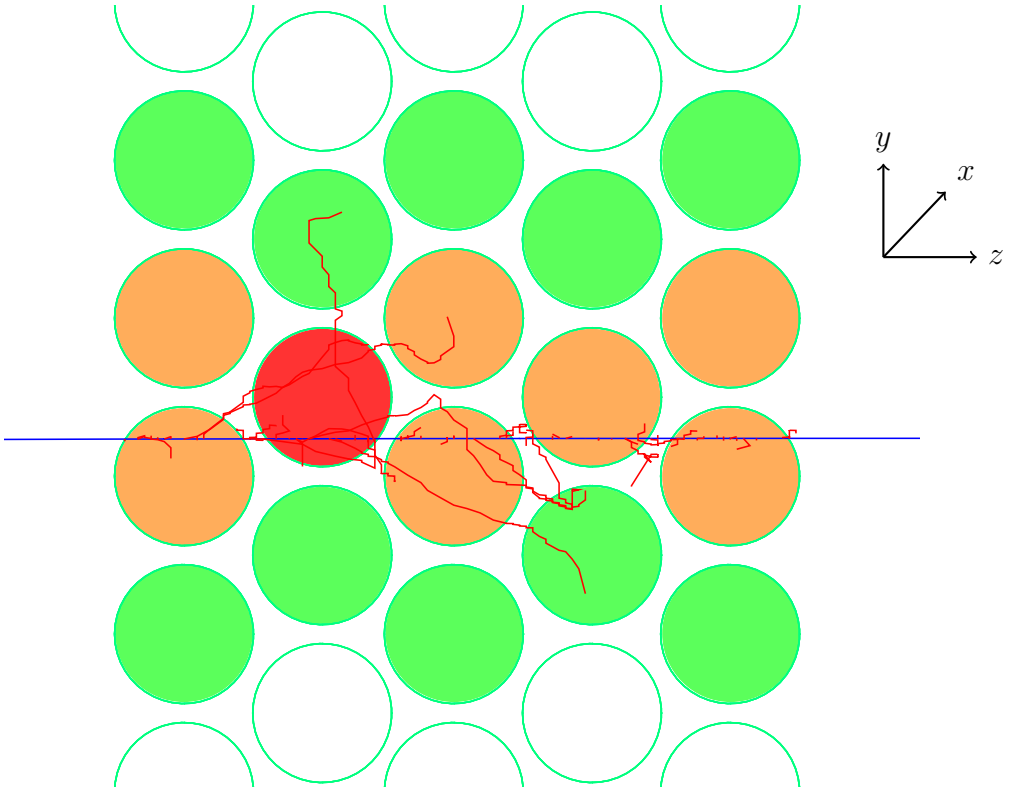

Fig. 7.3: Schematic representation of cluster reconstruction in the `TrackReconstruction class`. The fiber with highest energy deposition and its corresponding "slice" s_{max} defined by all fibers on the same position in y direction plus all fibers shifted by a fiber's radius upwards or downwards are identified. Subsequently all neighbouring layers $s_{max,\pm n}$ above and below are checked for energy deposition.

to be reconstructed. The energies in the fibers of its corresponding "slice" s_{max} (in figure 7.3) are added to the cluster energy. After definition of s_{max}, fibers of subsequent slices $s_{max,\pm n}$ above and below are requested for energy deposition (in figure 7.3). This procedure is followed until a slice without any energy deposition is found. The cluster energy derived by this process has to be larger than 0.2 MeV, otherwise the cluster is discarded. Further clusters are reconstructed in the same manner on condition that fibers already assigned to a cluster are skipped.

Particular attention has to be paid to the fact that each fiber tracker module gives information on only one spatial direction due to its geoemtry. In the simulation, where the positions of the fibers are known, a spatial coordinate in x direction (horizontal) and y direction (vertical) can be attributed to each cluster for track reconstruction. In this case, the median of all fiber positions of a specific cluster is

calculated. The median is used due to its robustness against outliers. One can for example think of a single secondary electron travelling relatively long distances in the fiber tracker before it is stopped. The average value of all spatial coordinates would be shifted towards fibers only hit by that electron, which does not coincide with the fragments trajectory.

Once all clusters are identified, the spatial information is extrapolated to the calorimeter region in order to find the corresponding energy deposition E_{tot} in one of the crystals. Each possible combination of horizontal and vertical clusters pointing to a BGO crystal with energy deposition is stored in a full track container (see definition 1 on page 84). In real measurements, the information of the 32 SiPM of each fiber tracker module must be used to identify the correct BGO crystal.

7.3.2 Verification of cluster reconstruction

In order to verify the correctness of the position reconstruction of each cluster explained in the last section, the spatial coordinates of any particle hitting a BGO crystal are saved in the simulation as MC truth and compared to the reconstructed cluster positions.

A simulation of 10^5 primary ^{12}C-ions is conducted and data is not smeared for this initial test of the track reconstruction code. In order to gain statistics, the target is not simulated so that the generated primary particles directly hit the fiber tracker modules and generate clusters.

Results

The differences of true and reconstructed calorimeter positions $x_{\mathrm{true}} - x_{\mathrm{reco}}$ and $y_{\mathrm{true}} - y_{\mathrm{reco}}$ shown in figure 7.4 are small compared to the dimensions of the BGO crystals with an edge length of $20-30\,\mathrm{mm}$. A 2D gaussian fit leads to standard deviations of $\sigma_{\mathrm{x}} = 0.16\,\mathrm{mm}$ and $\sigma_{\mathrm{y}} = 0.15\,\mathrm{mm}$. 90% of all reconstructed trajectories lie in a range of $(0.04 \pm 0.26)\,\mathrm{mm}$ for the x direction and $(0.05 \pm 0.25)\,\mathrm{mm}$ for the x direction, respectively.

Therefore it can be concluded that nuclear reactions taking place in the fiber tracker are irrelevant and the assumption of straight trajectories and their extrapolation to the calorimeter region can be performed as explained above. Nevertheless, a validation of the crystal identification of the `TrackReconstruction` class is realized in the next section.

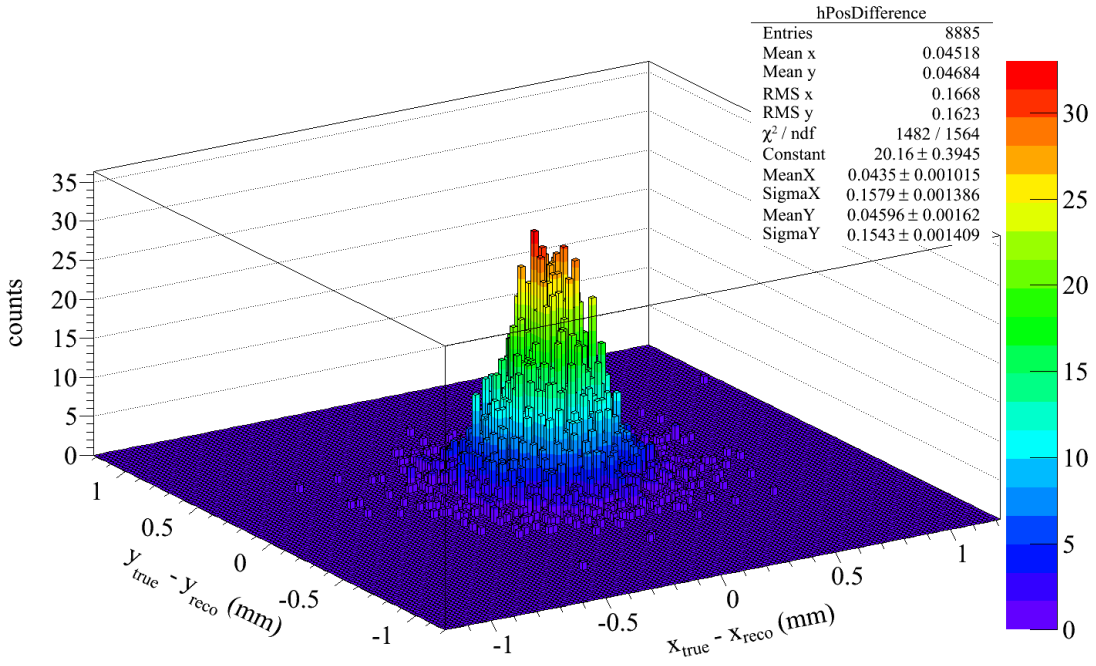

Fig. 7.4: Difference of true and reconstructed cluster positions in x and y direction. The results of a 2D gaussian fit can be found in the statistics box.

7.3.3 Verification of calorimeter crystal identification

As mentioned above, a reconstructed position is linked to one of the BGO crystals. The MC truth is used in this analysis to verify the correctness of predicted BGO crystals.

Results

The accuracy of the crystal identification is illustrated in figure 7.5.

On the right plane, a schematic drawing of the calorimeter assembly is shown, in which the the crystals are numbered consecutively (only the nine "inner" BGO crystals and the centered plastic scintillator are considered here).

The left panel finally includes a correlation plot of the reconstructed crystal hits and the true crystal hits, with which it is possible to give a reliable indication of the quality of the identification. For example, there are 44 misidentifications of the centered crystal a in contrast to 7113 correct identifications leading to a ratio of $n_{a,\,\mathrm{false}}/n_{a,\,\mathrm{total}} \approx 99.4\,\%$. Similar results are achieved for the crystals $b-e$, which are directly adjacent to the centered plastic scintillator. However, the situation is different for crystals $f-i$ situated further away, where the identification rates lie in

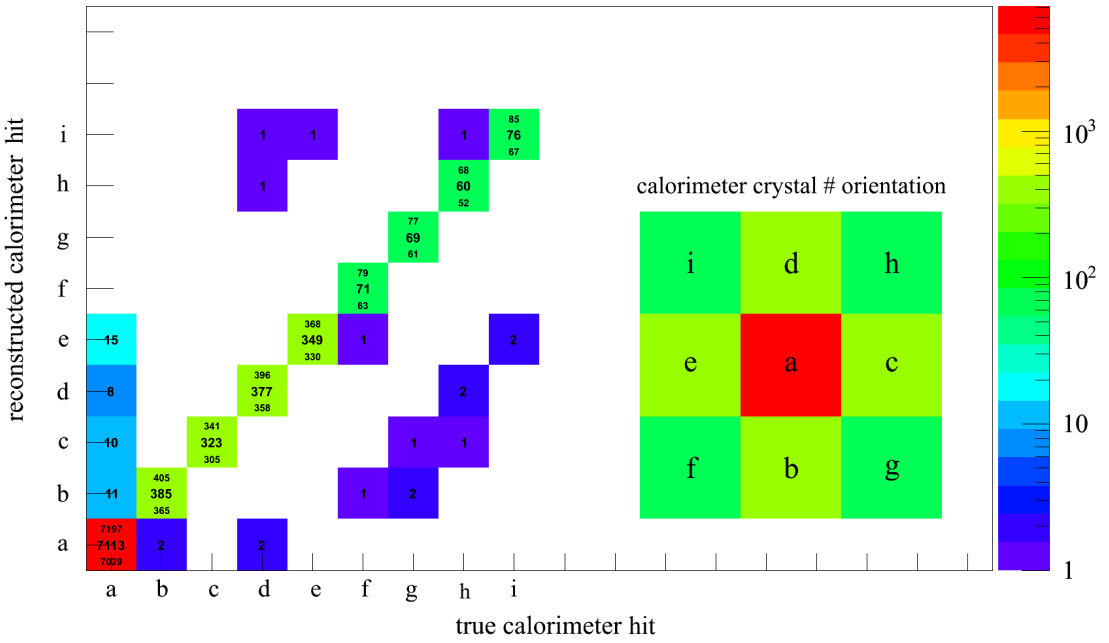

Fig. 7.5: Correlation of reconstructed calorimeter crystal hits and true calorimeter crystal hits. For orientation purposes, a schmematic drawing of the calorimeter is shown on the right side of the plot. The individual entries n in the correlation plot are displayed in the corresponding bin. The numbers $n_{\pm}$ above and below are a measure for the uncertainty calculated via $n_{\pm} = n \pm \sqrt{n}$.

the range of $95,2\,\%$ for crystal h to $97.4\,\%$ for crystal i.

The calorimeter identification confirms the rather good behaviour of the track reconstruction so that it is reasonable to suppose that the particle's trajectories are correctly reconstructed and the correct crystal is identified. As mentioned above, data smearing is not taken into account yet. Results with more realistic data will therefore become more inexact. Nevertheless, it is assumed that crystal identification will still produce satisfying results, since the differences of true and reconstructed cluster positions is very small compared to the dimensions of the BGO crystals.

7.4 Analytical calculation of correlation curves concerning TOF and E

According to equations (7.1) and (7.2), the mass of a particle is determined by measuring TOF and E. To get a first rough estimate and in regard to the analysis presented in the following section, the correlation of TOF and E is examined for isotopes with $Z = 1$ and $Z = 6$.

It should be noted that the correlations are not from simulated or measured data.

Instead, the total energy depositions are calculated analytically for different given TOF in order to provide a first overview. Both quantities are smeared in this analysis to take the intrinsic uncertainties into account. Timing resolutions of 1 ns and 0.3 ns are compared and the resolution of E_{tot} is set to $\sigma_{E_{\mathrm{tot}}} = \sqrt{\alpha + \beta E_{\mathrm{tot}}}/E_{\mathrm{tot}}$ with constants α and β according to [Mat+99].

Results

Figure 7.6 illustrates the correlations of TOF and E for protons, deuterons and tritons on the one hand and for different carbon isotopes on the other hand.

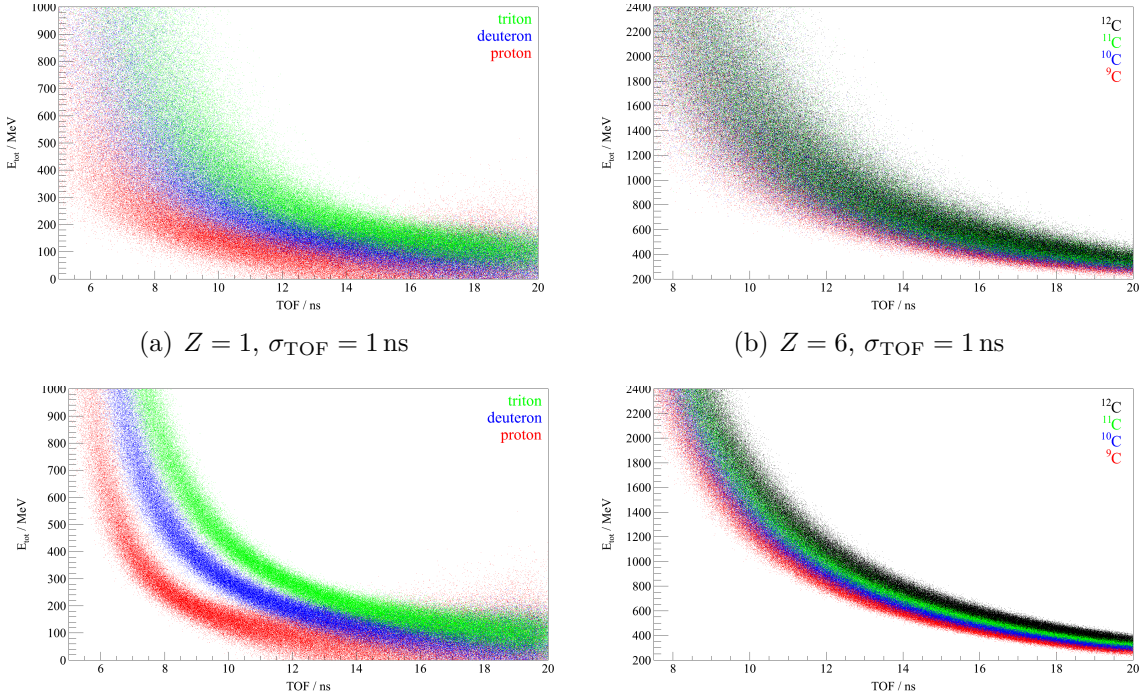

(a) $Z = 1$, $\sigma_{\mathrm{TOF}} = 1\,\mathrm{ns}$

(b) $Z = 6$, $\sigma_{\mathrm{TOF}} = 1\,\mathrm{ns}$

(c) $Z = 1$, $\sigma_{\mathrm{TOF}} = 0.3\,\mathrm{ns}$

(d) $Z = 6$, $\sigma_{\mathrm{TOF}} = 0.3\,\mathrm{ns}$

Fig. 7.6: Comparison of the correlation of TOF and E_{tot} for protons, deuterons and tritons and for different carbon isotopes for TOF resolutions of 1 ns and 0.3 ns. The flight distance is set to 1.5 m, which is the distance from the target to the fiber tracker.

As the mass differences between the carbon isotopes are small compared to the mass difference of protons and tritons, for example, a distinction of these isotopes is more difficult. In the case of $\sigma_{\mathrm{TOF}} = 1\,\mathrm{ns}$, data points of the different carbon isotopes are strongly overlapping and an identification seems to be difficult.

In conclusion, a time resolution of $\sigma_{\mathrm{TOF}} = 1\,\mathrm{ns}$ is not sufficient to facilitate mass identification in the final setup.

7.5 Identification of primary ions without target simulation and data smearing

After track reconstruction, each full track enters the χ^2-calculation for particle identification. For initial investigations of the particle identification, the target is not simulated and the kinematic variables are not smeared. Instead, different types of ions are set as primary particles in order to imitate target fragments. This has the advantage that a sufficient amount of data is collected rapidly.

In order to compare the results for the bar tracker and the fibre tracker, separate simulations are performed and, in addition, a further simulation with both detection systems is conducted. 10^5 primary ions are simulated for each detection device and subsequently analyzed, whereby their initial kinetic energy is selected in such a way that it is comparable to the vertex kinetic energies of the corresponding target fragment (see section 6.2).

Because there is only one particle traversal, namely that of the primary ion, the energy deposition in the $\mathrm{d}E/\mathrm{d}x$-devices and in the BGO crystal is directly allocated to the primary ion. Concerning the reconstruction, no χ^2-cut is applied at the end of the χ^2-calculation.

Results

The results for all three configurations are shown in figure 7.7.

The bar tracker allows for higher identification ratios compared to the fiber tracker, especially for heavier target fragments. A combination of both devices performs best, which is due to the cumulated statistics for $\mathrm{d}E/\mathrm{d}x$ and TOF measurement. Again, the problem already mentioned in section 6.4.2 comes into play here: The energy deposition of traversing particles in the fiber tracker is defined by their path length, which varies according to the crossing position and cannot be determined in experiment. In principle, the reconstruction algorithm assumes an average path length for each particle crossing the fiber tracker.

As explained above, the mass differences between the carbon isotopes is rather small compared to particles with $Z = 1$. A distinction of these isotopes is more difficult and hence identification rates are rather small.

It is notable that the decrease in identification ratios from protons to tritons is significant. The majority of misidentifications for particles with $Z = 1$ comes from protons (in the case of primary deuterons) and from protons and deuterons (in the case of primary tritons). Having a look at the total energy deposition in figure 7.8,

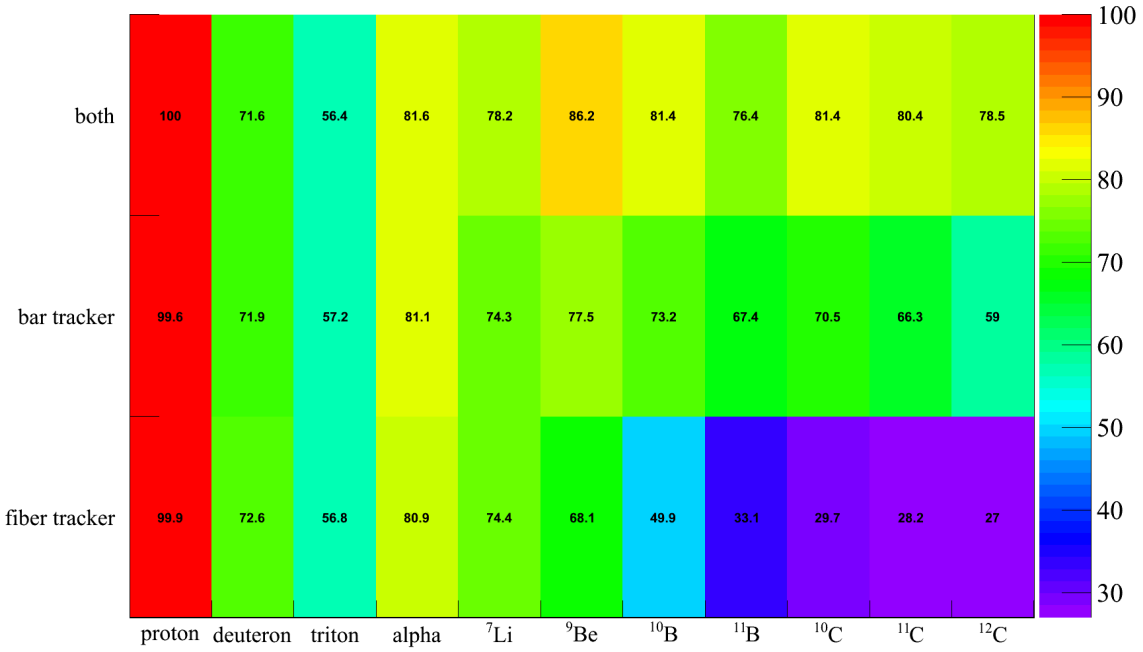

Fig. 7.7: Ratios of correctly identified events to the number of incident events for each particle type and detection device. The number in each bin belongs to the corresponding percentage.

one may easily identify the vertex kinetic energy peaks. In addition, there is a wide range of smaller energy depositions down to 0 MeV. These are responsible for the misidentifications, what can be explained with figure 7.6(c): The calculated total energy $E_{\mathrm{tot,calc}}$ is matched to one of the lighter fragments below a certain value of $E_{\mathrm{tot,meas}}$. For a TOF of 10 ns, for example, it is more likely that a triton is identified as a deuteron, if E falls in the range of ≈ 300 MeV.

7.6 Identification of primary ions with separate smearing of kinematic variables

Since the general behaviour of particle identification (PID) is understood, the kinematic variables are separately smeared in the next step to take detector resolutions in the simulation into account. This is achieved using the ROOT random generator TRandom3 taking a given uncertainty σ (σ_{TOF}, $\sigma_{\mathrm{d}E/\mathrm{d}x}$ or σ_E) as input parameter to smear the corresponding quantity. The same σ is subsequently used during χ^2-calculation.

In this analysis, only a single kinematic variable is smeared. The remaining two quantities have a fixed uncertainty of $\sigma_{\mathrm{TOF}} = 0.5$ ns, $\sigma_{\mathrm{d}E/\mathrm{d}x} = 0.5$ MeV and $\sigma_E =$

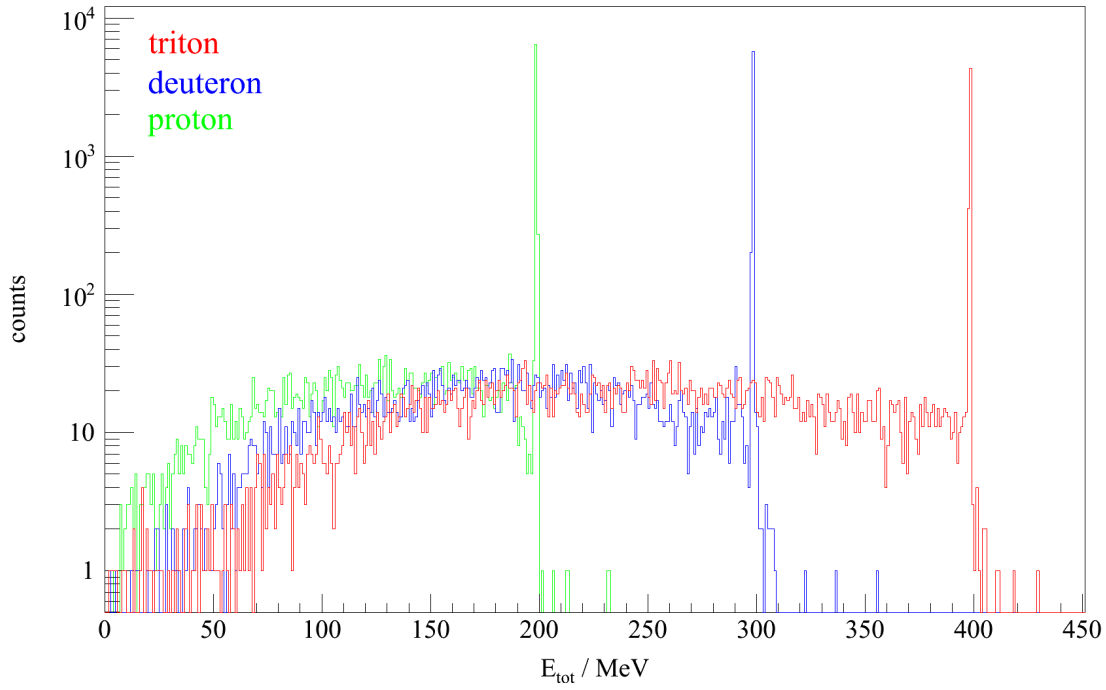

Fig. 7.8: Total energy deposition E_{tot} in the calorimeter of 10^5 simulated protons, deuterons and tritons each. The vertex kinetic energies of $SI200MeV$, 300 MeV and 400 MeV are clearly recognizable.

50 MeV, which are solely used in the χ^2-calculation.

The two measurements of $\mathrm{d}E/\mathrm{d}x$ and TOF in both fibre tracker modules are not averaged. Instead, they enter χ^2-calculation as separate quantities. In this section, three different types of ions are used as primary particles, namely protons, ^{9}Be-ions and ^{12}C-ions with energies of 200, 1200 and 2000 MeV.

7.6.1 TOF smearing

Concerning the smearing of time-of-flight, σ_{TOF} is varied between 0.001 ns and 1 ns. The first-mentioned resolution is not realistic, but used for comparison purposes to non-smeared data.

Results

Figure 7.9 shows the resulting PID rates after TOF smearing for the aforementioned primary ion beams.

As expected, the PID rates are smaller for large σ_{TOF}. In addition, the basic behaviour of decreasing PID rates with increasing particle mass can be observed again.

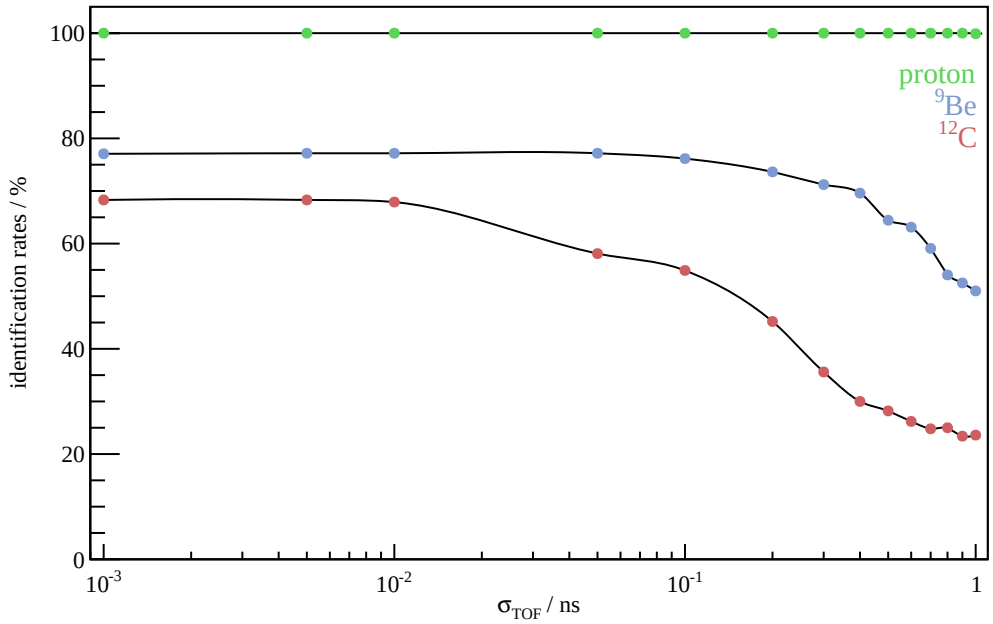

Fig. 7.9: PID rates of primary protons, ^{9}Be-ions and ^{12}C-ions for smeared TOF and fixed $\sigma_{\mathrm{d}E/\mathrm{d}x} = 0.5\,\mathrm{MeV}$ and $\sigma_E = 50\,\mathrm{MeV}$.

In particular, the excellent PID rate for protons extends to the whole resolution range considered here. The PID rate for ^{12}C-ions is rather low and starts to increase significantly at values below 0.4 ns.

7.6.2 dE/dx smearing

The uncertainty $\sigma_{\mathrm{d}E/\mathrm{d}x}$ of energy loss measurements in both fiber tracker modules is varied between 0.001 MeV and 10 MeV, whereas the detection setup and statistics are the same as in the previous section.

Results

The analysis results are presented in figure 7.10.

It is striking that both ^{9}Be and ^{12}C curves feature a peak at $1^{+1}_{-0.1}\,\mathrm{MeV}$ and $(2 \pm 1)\,\mathrm{MeV}$. The width of the broadened energy deposition due to differing path lengths discussed in section 6.4.2 can be characterized by a RMS value describing the uncertainty of measuring $\mathrm{d}E/\mathrm{d}x$. As it will be shown in section 7.8.2, it is possible to find a linear relation between RMS / $\sigma_{\mathrm{d}E/\mathrm{d}x}$ and the corresponding $\mathrm{d}E/\mathrm{d}x$.

Using smaller $\sigma_{\mathrm{d}E/\mathrm{d}x}$ would imply that the (broadly distributed) energy depositions in the fiber tracker are considered to be precise and thus leading to false identifications. Here again, PID rates decrease when going to higher uncertainties $\sigma_{\mathrm{d}E/\mathrm{d}x}$

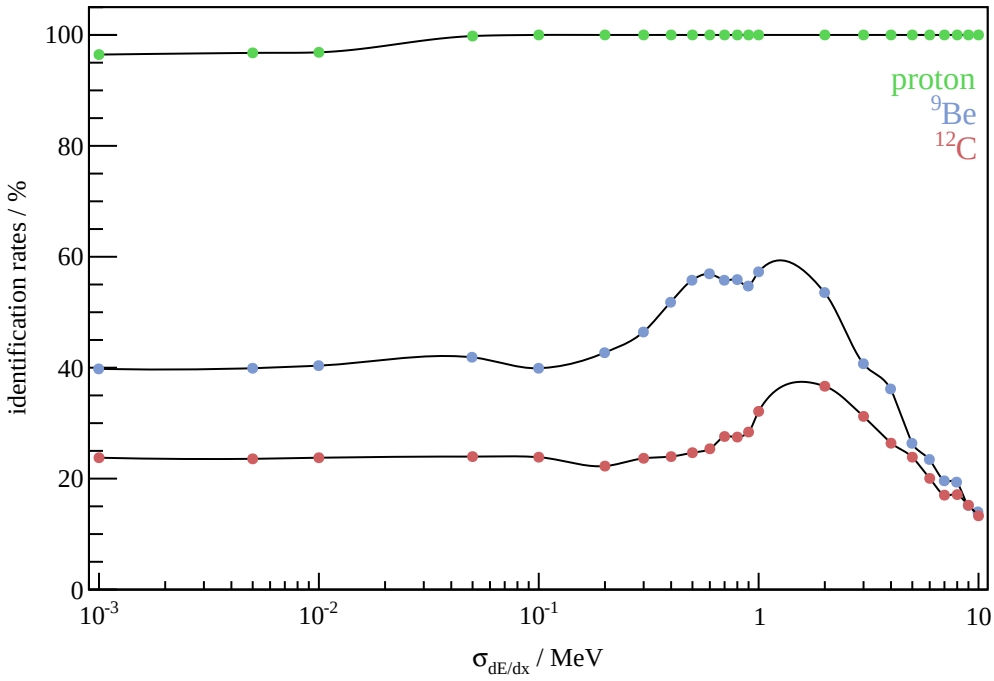

Fig. 7.10: PID rates of primary protons, ^{9}Be-ions and ^{12}C-ions for smeared $\sigma_{\mathrm{d}E/\mathrm{d}x}$ and fixed $\sigma_{\mathrm{TOF}} = 0.5\,\mathrm{ns}$ and $\sigma_E = 50\,\mathrm{MeV}$.

behind the peak region.

7.6.3 E_{tot} smearing

The total energy deposition E_{tot} is smeared in the range from $\sigma_E = 1\,\mathrm{MeV}$ to $\sigma_E = 100\,\mathrm{MeV}$.

Results

The results are depicted in figure 7.11.

The general trend of decreasing PID rates for increasing uncertainties σ_E can be found again. PID rates for protons and ^{9}Be-ions feature a steeper decrease for increasing σ_E, whereas ^{12}C-ions are identified on a rather low but constant level.

This can be explained by the fact that a fixed resolution of $\sigma_{\mathrm{TOF}} = 0.5\,\mathrm{ns}$ is too large concerning the distinction of carbon isotopes and hence the identification of ^{12}C (see section 7.4).

In conclusion, further combinations of σ_{TOF} and $\sigma_{\mathrm{d}E/\mathrm{d}x}$ have to be taken into account in order to investigate a possible variation in the identification of ^{12}C, which is subject of the following section.

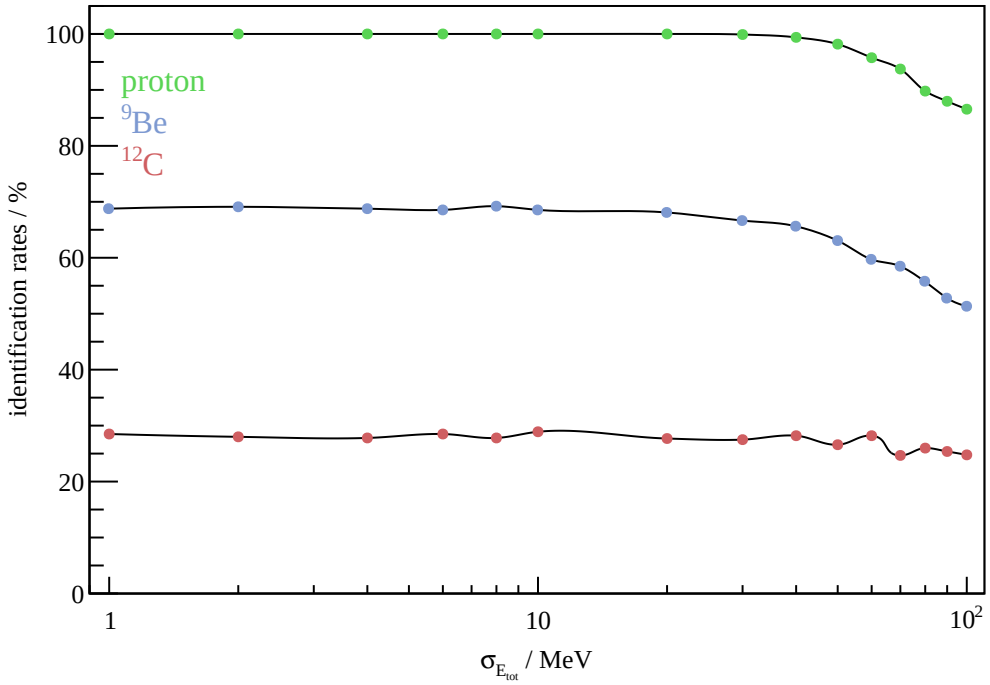

Fig. 7.11: PID rates of primary protons, ^{9}Be-ions and ^{12}C-ions for smeared E and $\sigma_{\mathrm{TOF}} = 0.5\,\mathrm{ns}$ and $\sigma_{\mathrm{d}E/\mathrm{d}x} = 0.5\,\mathrm{MeV}$.

7.7 Analysis of carbon ions with combined smearing of kinematic variables

In contrast to the previous section, the kinematic variables TOF, $\mathrm{d}E/\mathrm{d}x$ and E_{tot} are simultaneously smeared in this section to investigate the variation of identification of ^{12}C-ions.

The uncertainties σ_{TOF} and $\sigma_{\mathrm{d}E/\mathrm{d}x}$ are varied in the range from 0.1 ns to 1 ns and from 0.1 MeV to 1 MeV in steps of 1 ns and 1 MeV, respectively, resulting in 100 possible combinations. These combinations are realized for $\sigma_E = 10\,\mathrm{MeV}$, $\sigma_E = 50\,\mathrm{MeV}$ and $\sigma_E = 100\,\mathrm{MeV}$ each.

Results

For each value of σ_E, a 3D histogram displaying the PID rates dependent on σ_{TOF} and $\sigma_{\mathrm{d}E/\mathrm{d}x}$ is shown in figures 7.12(a) to 7.12(c). In contrast to the results presented in figure 7.11 a much larger variation of PID rates is observed.

The general trend of increasing PID rates for decreasing σ_{TOF}, as depicted in figure 7.9, can be found again for all σ_E. This increase becomes apparent from about 0.5 ns, which coincides with the results presented in figure 7.9.

As was expected, the smaller the σ_E, the higher is the PID rate: From maximum PID values of 35 % in the case of $\sigma_E = 100\,\mathrm{MeV}$ the rate increases to 49 % in the case of $\sigma_E = 10\,\mathrm{MeV}$. Nevertheless, these PID rates seem rather low, but it should be kept in mind that no cuts, neither on χ^2 nor on kinematic variables are applied yet.

Here again, the peak structure mentioned in section 7.6.2 in the context of $\mathrm{d}E/\mathrm{d}x$-smearing can be found. Because all quantities are smeared in this analysis, the peak position does not necessarily correspond with those shown in figure 7.11 for the same $\sigma_{\mathrm{d}E/\mathrm{d}x}$. For larger TOF resolutions, the bin of maximum PID rate moves to larger $\sigma_{\mathrm{d}E/\mathrm{d}x}$.

The results of this section reveal, that a TOF resolution of $\sigma_{\mathrm{TOF}} \approx 0.5\,\mathrm{ns}$ or better should be reached in the final setup to enable identification of carbon ions.

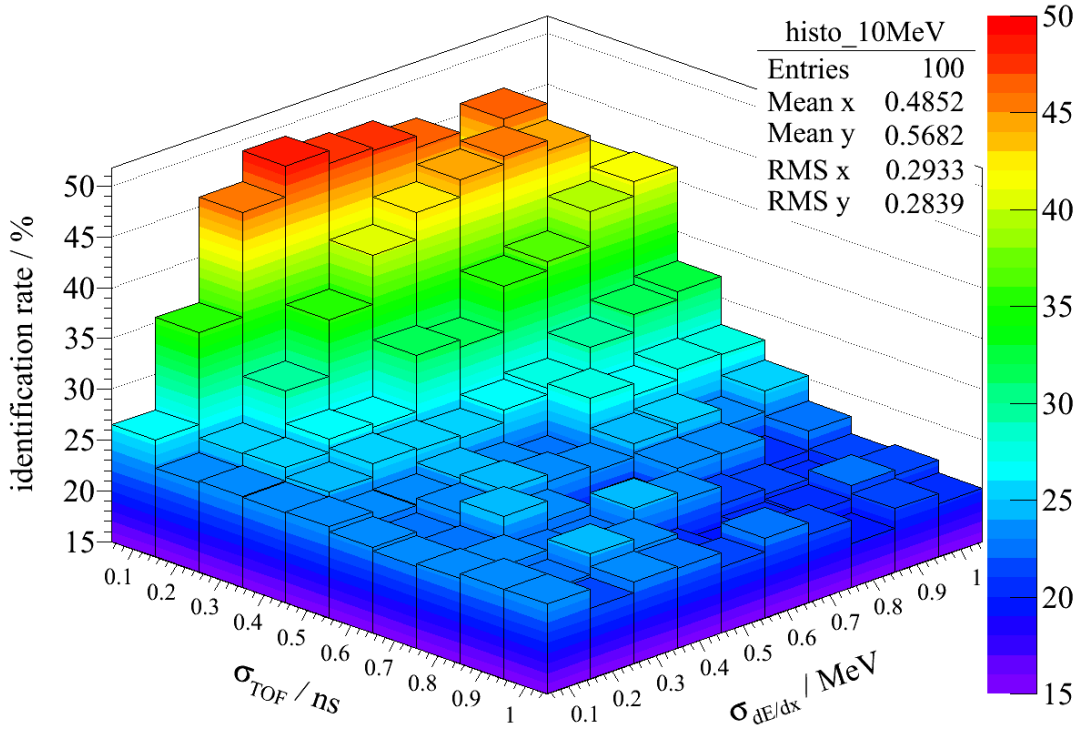

(a) $\sigma_E = 10\,\mathrm{MeV}$

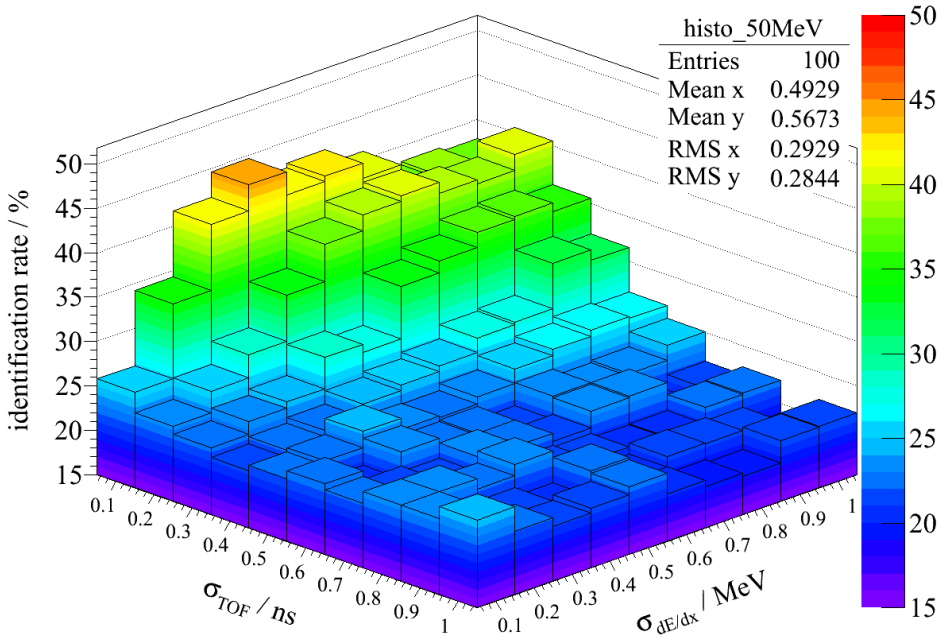

(b) $\sigma_E = 50\,\mathrm{MeV}$

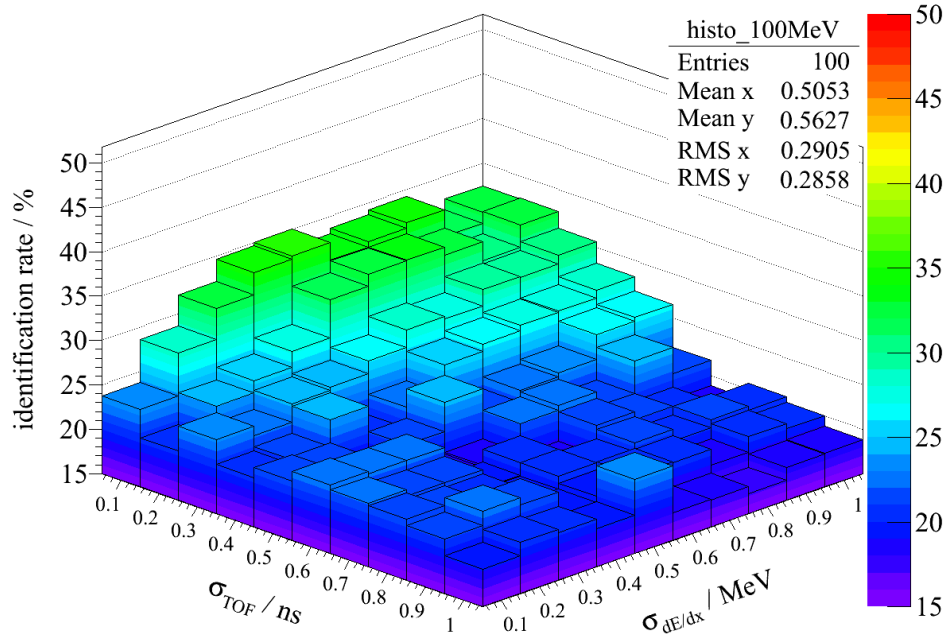

(c) $\sigma_E = 100\,\mathrm{MeV}$

Fig. 7.12: PID rates of ^{12}C-ions for different uncertainties σ_E dependent on diverse combinations of σ_{TOF} and $\sigma_{\mathrm{d}E/\mathrm{d}x}$.

7.8 Selection of uncertainties for the final analysis

So far, the uncertainties σ_{TOF}, $\sigma_{\mathrm{d}E/\mathrm{d}x}$ and σ_E were extensively varied to examine effect on particle identification. For the final analysis of the two most abundant reaction channels (see table 4.1), these uncertainties have to be adjusted to realistic conditions.

7.8.1 Adjusting σ_{TOF}

The timing resolution of the fiber tracker was investigated in detail by Ronja Lewke in her master thesis [Lew12]. This was done using a laser to irradiate fibers pointing onto a single SiPM, which generates the stop signal of the time measurement. A start signal was triggered by a detector integrated into the laser system, which generates a signal each time the laser is fired. Laser pulse energies of approximately 0.2 MeV, 0.8 MeV and 2 MeV were used during measurement. The uncertainties σ_{TOF} and their errors were obtained from a gaussian fit to the time spectra [Lew12]:

$$\sigma_{\mathrm{TOF}}(0.2\,\mathrm{MeV}) = (1.582 \pm 0.200)\,\mathrm{ns} \tag{7.5}$$

$$\sigma_{\mathrm{TOF}}(0.8\,\mathrm{MeV}) = (1.033 \pm 0.058)\,\mathrm{ns} \tag{7.6}$$

$$\sigma_{\mathrm{TOF}}(2\,\mathrm{MeV}) = (0.630 \pm 0.005)\,\mathrm{ns}\ . \tag{7.7}$$

The number of photons detected by the SiPM is a measure for the energy deposition of the particle. The timing resolution increases the more photons are impinging on the SiPM cells. In order to obtain timing resolutions dependent on energy deposition in the fiber tracker for different energies than the three values above, a fit of the form

$$f(\Delta E) = \frac{p_0}{\sqrt{\Delta E}} \tag{7.8}$$

is applied, where p_0 is a fit parameter and ΔE is the energy deposition. It is expected that the timing resolution scales with the inverse of the square root of the number of detected photons [Lew12]. The number of detected photons is again proportional to the energy deposition in the fiber tracker.

Results

Figure 7.13 shows the result of the fit procedure.

As was expected, the time resolution σ_{TOF} gets better with increasing energy deposition in the fiber tracker, which is well described by the fit curve. The targeted

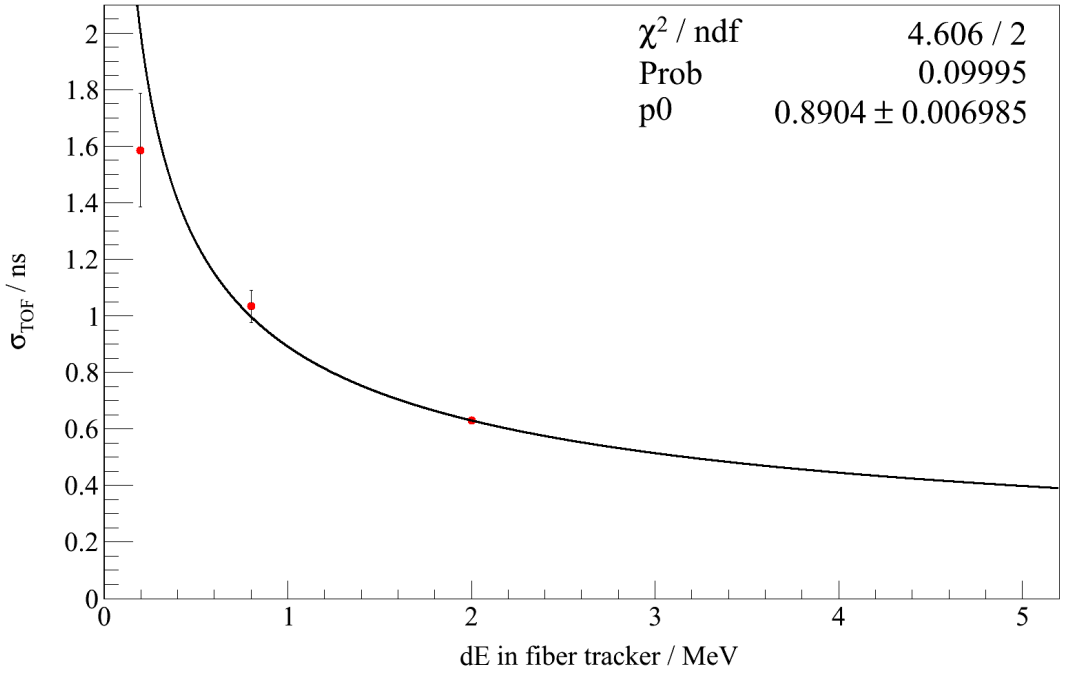

Fig. 7.13: TOF resolution σ_{TOF} of measured data and the corresponding fit dependent on the energy deposition in a single fiber tracker module.

value of 300 ps is hard to achieve, especially for light particles with small energy depositions. For example, a TOF resolution of $\sigma_{\mathrm{TOF}} = 500\,\mathrm{ps}$ is achieved for energy depositions roughly above 3 MeV. In addition, the time resolution of the start detector has to be taken into account.

In the final analysis, σ_{TOF} is calculated with the parameters determined from the fit according to equation (7.8) for each full track. A constant time resolution of $\sigma_{\mathrm{TOF,\,Start}} = 0.2\,\mathrm{ns}$ is added quadratically to the value of σ_{TOF} to take the effect of the start scintillator into account.

7.8.2 Adjusting $\sigma_{\mathrm{dE/dx}}$

The energy resolution

$$\frac{\Delta E}{E} = (25 \pm 1)\,\% \tag{7.9}$$

determined in [Lew12] was measured by irradiating the fiber tracker with laser light, which is absorbed in the top layer of fibers only. A particle in the final experiment will cross the fiber tracker and continuously deposit energy along its path. Therefore, it is assumed that the energy resolution $\sigma_{\mathrm{d}E/\mathrm{d}x}$ in the final experiment will be better

and thus the question of how $\sigma_{\mathrm{d}E/\mathrm{d}x}$ should be set in the reconstruction code arises.

The RMS value of $\mathrm{d}E/\mathrm{d}x$ distributions in the fiber tracker presented in section 6.4.2 reflects the width of energy depositions of each ion species for a fixed vertex kinetic energy. In order to have access to different mean energy depositions, a further simulation is carried out simulating ^{7}Li, ^{9}Be, ^{11}B and ^{12}C-ions with different vertex kinetic energies ranging from 100 MeV to 2000 MeV.

Results

Plotting all RMS values against the mean of their distribution leads to the results shown in figure 7.14.

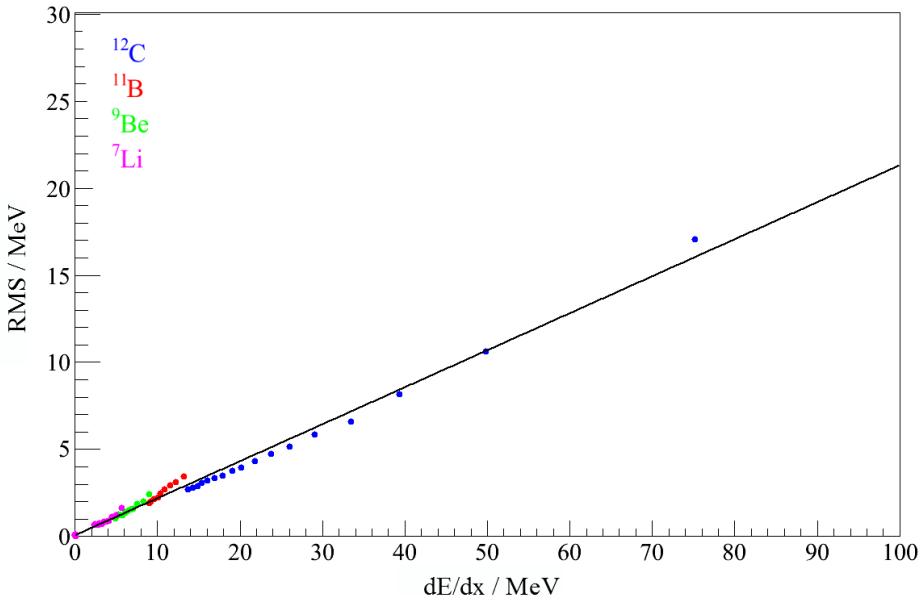

Fig. 7.14: RMS of $\mathrm{d}E/\mathrm{d}x$ distribution of several primary ions plotted against the corresponding mean for diverse vertex kinetic energies and a linear fit to the data points.

A linear relationship between the energy deposition $\mathrm{d}E/\mathrm{d}x$ and the corresponding RMS can be stated. Thus a linear fit to the data points seems reasonable and is applied.

The RMS value of any set of values predicted by a model is calculated in the ROOT framework according to

$$\mathrm{RMS} = \sqrt{\frac{1}{n}\sum_{i=1}^{n}(x_i - x_{\mathrm{mean}})^2}\ , \tag{7.10}$$

where n is the sample size of samples $\{x_i\}$ with mean x_{mean}. This is exactly the standard deviation of the distribution (see the definition of the function `GetRMS()` of ROOT's TH1 histogram class, for example). As can be seen from equation (7.10), the RMS is proportional to x_{mean} or the $\mathrm{d}E/\mathrm{d}x$ in the present case. Hence, the linear fit of the data points determines the energy resolution $\sigma_{\mathrm{d}E/\mathrm{d}x}$ for any energy deposition in the fiber tracker used in the reconstruction step.

7.8.3 Adjusting σ_E

A relative energy resolution of 8 % at 15 MeV energy deposition in the BGO crystals was measured by Benjamin Koska in his diploma thesis [Kos13]. This is used as input for the calculation of σ_E for different values of E via

$$\frac{\sigma_E}{E} = \frac{c}{\sqrt{E}} \,, \tag{7.11}$$

where c is a constant determined with the values listed above.

7.9 Analysis of reaction channels producing ^{11}B

Now that a reliable estimate of the uncertainties σ_{TOF}, $\sigma_{\mathrm{d}E/\mathrm{d}x}$ and σ_E has been established, the final analysis of specific reaction channels can be conducted. In the following, the two most important reaction channels according to table 4.1 are investigated in more detail:

- the production of ^{11}B in the reaction channel $^{12}\mathrm{C}(\mathrm{p},2\mathrm{p})^{11}\mathrm{B}$ discussed in this section and
- the production of ^{11}C in $^{12}\mathrm{C}(\mathrm{p},\mathrm{pn})^{11}\mathrm{C}$ analyzed in section 7.10.

Cuts on kinematic variables or the χ^2 itself are applied to achieve a gain in PID rates. In this context, the purity and efficiency (see section 2.10) are able to make a quantitative statement. They can be derived from the MC truth of simulated data, because a comparison of reconstructed and true particle types is possible.

As was shown in section 6.3, target thickness is less critical in the context of deviation of momentum direction and energy deposition than in the predecessor setup. Therefore, the two thicker targets with thicknesses of 1 mm and 10 mm are simulated for the final analysis of the abovementioned reaction channels.

Because $^{12}\mathrm{C}(\mathrm{p},2\mathrm{p})^{11}\mathrm{B}$ and $^{12}\mathrm{C}(\mathrm{p},\mathrm{pn})^{11}\mathrm{C}$ are the only reactions with the target protons in which the isotopes ^{11}B and ^{11}C are generated, it is sufficient to identify

the ^{11}B and ^{11}C. With regard to other reaction channels, this is not longer valid and further fragments need to be identified to allow for event reconstruction.

A simulation of 10^7 events for both target thicknesses has been conducted to investigate the reaction channel $^{12}\mathrm{C}(\mathrm{p}, 2\mathrm{p})^{11}\mathrm{B}$. A possible background reaction is the interaction of primary ^{12}C-ions with the carbon isotopes of the polyethylene target leading to $^{12}\mathrm{C}(\mathrm{p}, \mathrm{X})^{11}\mathrm{B}$, where X denotes all possible reaction products besides ^{11}B. This channel has to be distinguished from the reactions with the target protons leading to the reaction of interest. Further background originates from the reaction with target protons that lead to events which are reconstructed as $^{12}\mathrm{C}(\mathrm{p}, 2\mathrm{p})^{11}\mathrm{B}$.

In order to improve PID rates and hence keeping the impact of background reactions as small as possible, cuts on the kinematic variables are applied which are now evaluated and discussed.

7.9.1 Total energy

The cut on E_{tot} serves two purposes: Firstly, to avoid background from ^{11}B-like reactions mentioned above and secondly, to separate the reaction $^{12}\mathrm{C}(\mathrm{p}, 2\mathrm{p})^{11}\mathrm{B}$ from the reaction $^{12}\mathrm{C}(\mathrm{p}, \mathrm{X})^{11}\mathrm{B}$.

Results

Figure 7.15(a) and 7.15(b) show the total energy deposition of reconstructed ^{11}B-ions, which are really of that type.

As one might expect, the reaction rates obtained by using the thinner target are low compared to the ones of the thicker target. In either case the distinction between reactions with protons and carbon ions of the target material is possible, since the peak of E_{tot}-distribution of $^{12}\mathrm{C}(\mathrm{p}, \mathrm{X})^{11}\mathrm{B}$ is rather narrow. The use of a polyethylene target appears to be noncritical, at least for the reaction channel investigated in this section.

Figures 7.15(c) and 7.15(d) display the total energy depositions of all reconstructed ^{11}B-events. One can clearly see the huge background from primary ^{12}C-ions, whose peak has been cropped here. The rates of other reaction channels is comparable or even less.

The rate of ^{12}C-ions is not growing quite as vigorously as the ^{11}B distribution when using the thicker target. This may be explained by the fact that the majority of ^{12}C events can be assigned to primary ions, whose occurrence should not vary with target thickness.

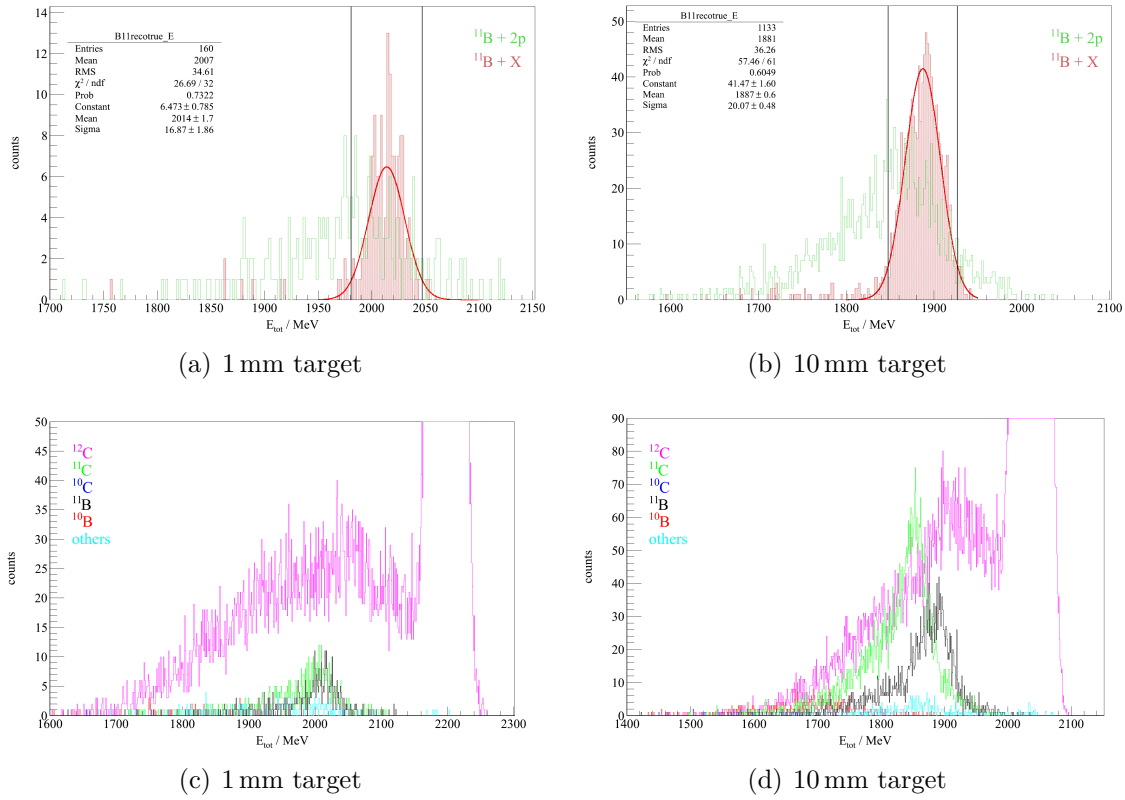

(a) 1 mm target

(b) 10 mm target

(c) 1 mm target

(d) 10 mm target

Fig. 7.15: Total energy depositions E_{tot} of correctly reconstructed ^{11}B-ions (a), (b). The reactions on target protons is denoted by "^{11}B+2p", the one on target carbon nuclei by "^{11}B+X". The vertical black lines denote the cuts applied in the final analysis. Total energy depositions of all reconstructed ^{11}B-ions are shown in (c) and (d).

Cut definition

The two reactions $^{12}\text{C}(\text{p}, 2\text{p})^{11}\text{B}$ and $^{12}\text{C}(\text{p}, \text{X})^{11}\text{B}$ are colour-coded differently in figures 7.15(a) and 7.15(b) to define suitable cut values in the following way: The σ and mean μ from the gaussian fit are used to define an interval $[\mu - 1.96\sigma, \mu + 1.96\sigma]$ holding 95 % of all values to exclude the background reaction. This interval is represented by the vertical lines in that figures and used as cut values in the final analysis leading to values of:

- 1 mm target: lower cut 1980.92 MeV, higher cut 2047.05 MeV,
- 1 cm target: lower cut 1847.93 MeV, higher cut 1926.62 MeV.

Figures 7.15(c) and 7.15(d) reveal that a clear distinction of ^{11}B-events from background reactions is not possible to a desired extent by applying cuts on E. Instead, the distributions are used only to exclude the peak of primary carbon ions. In the course of this thesis, a more detailed cut analysis could not be carried out. A future

analysis could lead to a more systematic implementation of cut sequences concerning the E_{tot}-distribution.

7.9.2 Time-of-flight

Figure 7.16 displays the TOF distribution of reconstructed ^{11}B-events. True ^{11}B-events are shown in shaded black colour.

As can be seen in figure 7.16, the TOF distributions of reconstructed ^{11}B-events strongly overlap and thus the separation from background reactions is expected to be poor. The slightly smaller time-of-flight of particles in the case of the 1 mm target may be explained by the additional energy loss of particles in the thicker target leading to decreased kinetic energies and hence smaller TOF.

Cut definition

Here again, the cuts obtained from a gaussian fit are are denoted by two vertical black lines to define an interval $[\mu - 1.96\sigma,\ \mu + 1.96\sigma]$ holding 95 % of true ^{11}B-events:

- 1 mm target: lower cut 14.13 ns, higher cut 15.62 ns,
- 1 cm target: lower cut 14.40 ns, higher cut 15.69 ns.

7.9.3 Specific energy loss

The $\mathrm{d}E/\mathrm{d}x$-distribution of reconstructed ^{11}B-events is shown in figure 7.17 for both target thicknesses.

As can be seen in figure 7.17, the $\mathrm{d}E/\mathrm{d}x$-distribution of true ^{11}B-events should allow to cut off background especially from ^{11}C and ^{12}C-events while losing only a small proportion of correct events, because the distributions of both carbon isotopes are broader and shifted towards higher energies compared to the ^{11}B-distribution.

Cut definition

A gaussian fit is applied to the the right slope of true ^{11}B-events to define a cut value of $\mu + 1.96\sigma$ to avoid background from higher $\mathrm{d}E/\mathrm{d}x$ of incorrect identified events. Here, too, the cut value is chosen to exclude 5 % of the gaussian distribution leading to the following cut values:

- 1 mm target: 11.05 MeV,
- 1 cm target: 11.58 MeV.

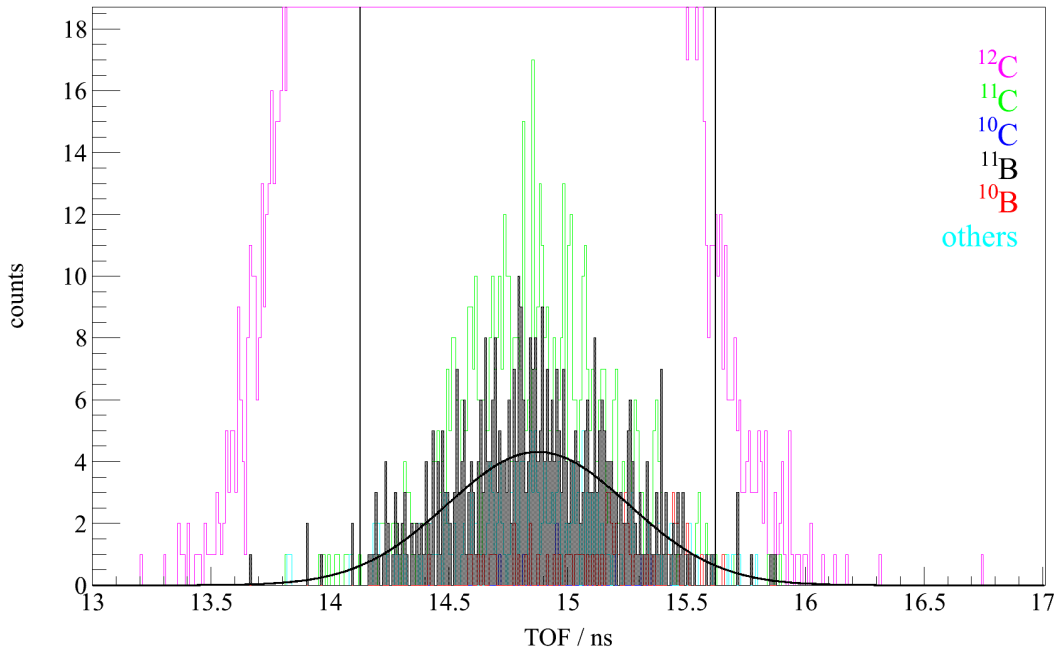

(a) 1 mm target

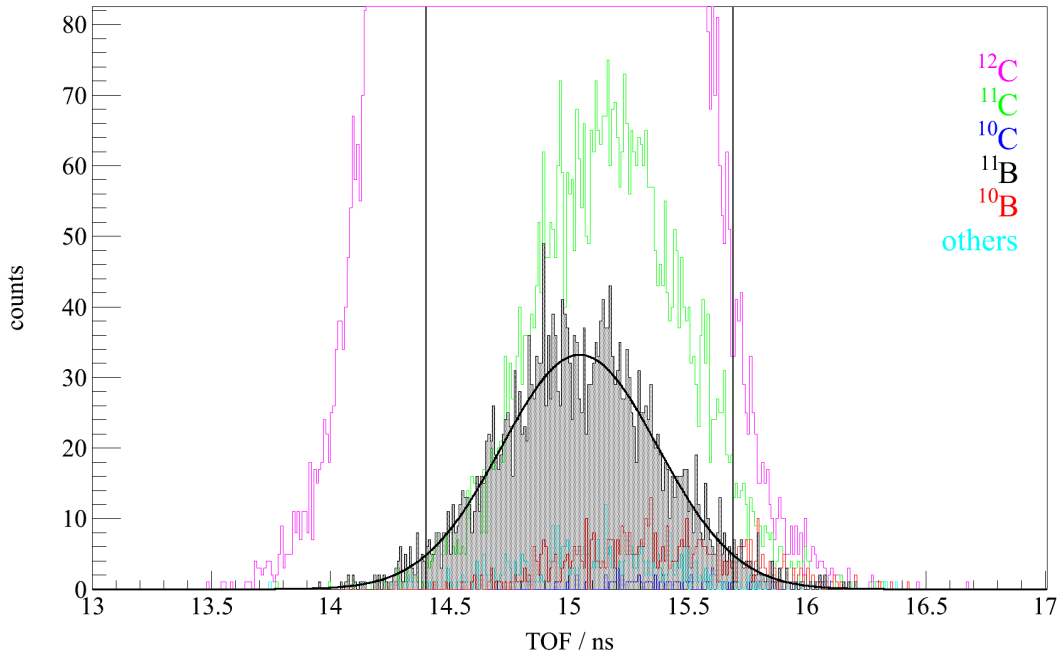

(b) 10 mm target

Fig. 7.16: TOF distribution of reconstructed ^{11}B-events. The primary peak is omitted for the sake of clarity. The vertical black lines denote the cuts applied in the final analysis.

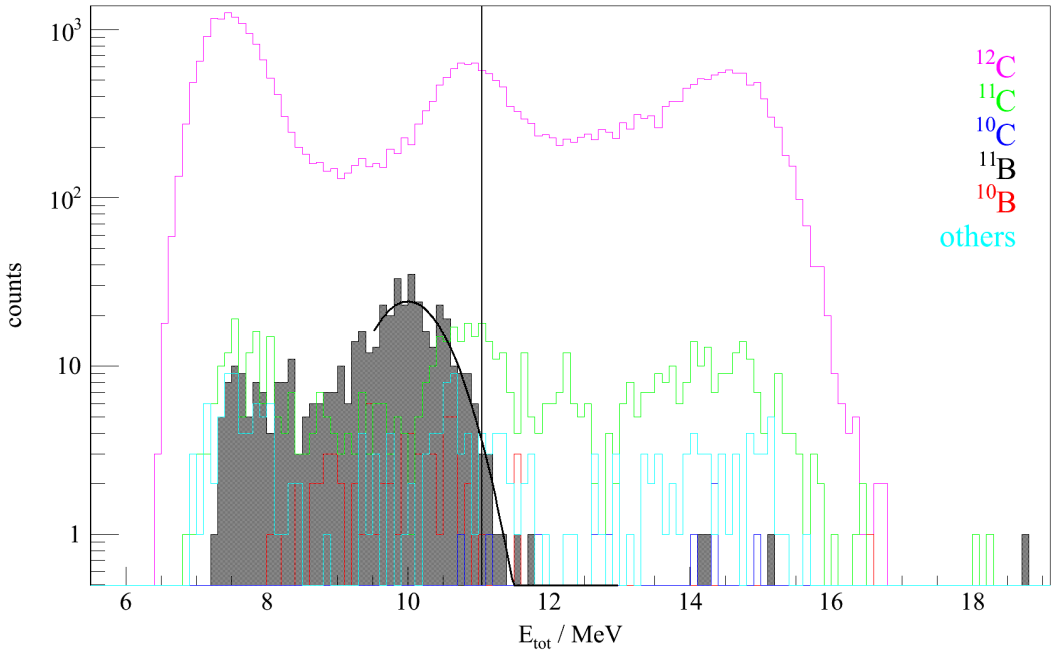

(a) 1 mm target

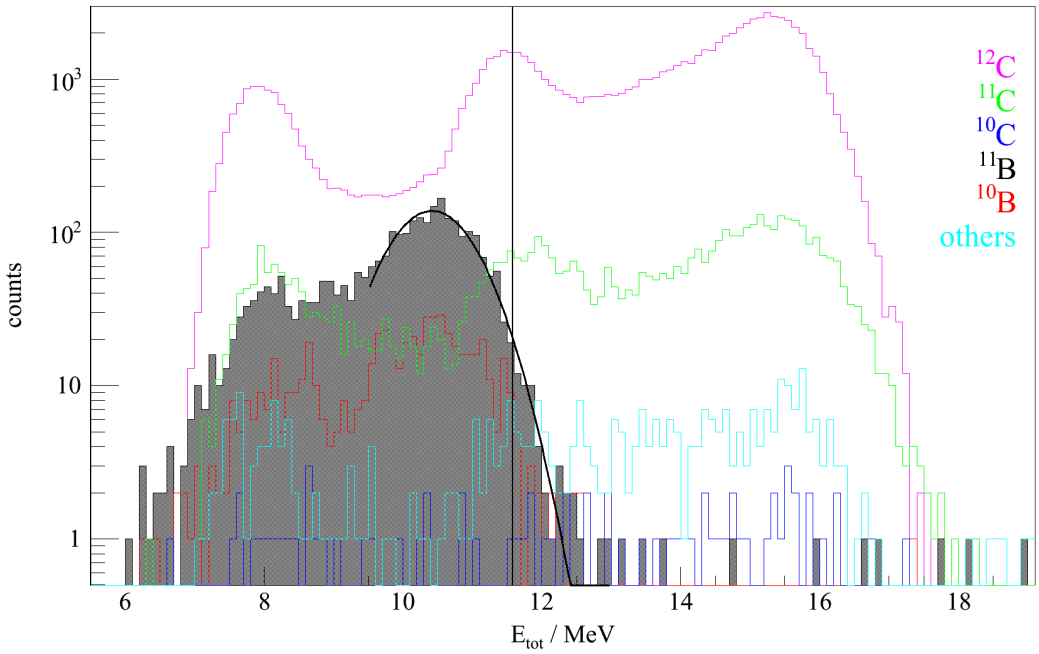

(b) 10 mm target

Fig. 7.17: dE/dx-distribution of reconstructed ^{11}B-events. The vertical black line denotes the upper limit of the cut applied in the final analysis.

7.9.4 Purity and efficiency

Now that all cut values of kinematic variables are derived, the essential results of purity and efficiency of the reaction channel $^{12}C(p, 2p)^{11}B$ can be retrieved. The final analysis is applied to the restricted data set due to the application of cuts. The definitions of purity and efficiency in equations (2.23) and (2.24) help to visualize the behaviour of cut dependency concerning the final cut on χ^2.

Results

In figure 7.18, purity and efficiency are plotted against different χ^2-cuts for both target thicknesses.

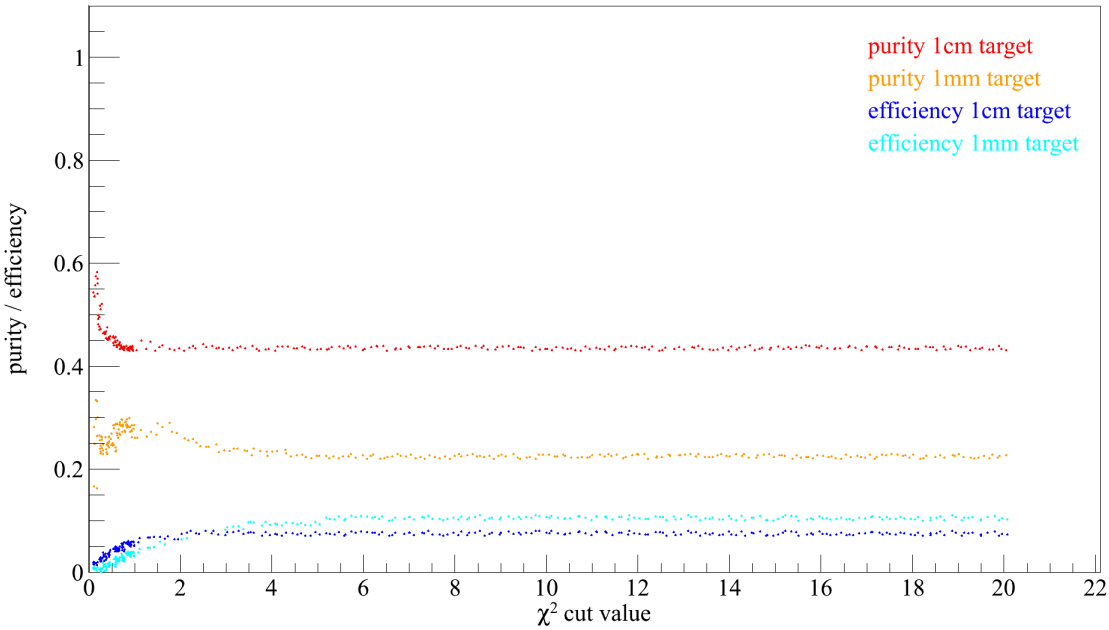

Fig. 7.18: Purity and efficiency of the analysis for the reaction channel $^{12}C(p, 2p)^{11}B$ as a function of the χ^2 value.

As can be seen in the plot, the use of thicker targets leads to an overall increase in purity to approximately 43 % compared to 22 % in the case of the 1 mm target. For thicker targets, the rate of nuclear reactions to the total number of events increases and as a result the signal-to-noise ratio improves. Only at small values of χ^2, the purity for each simulation increases significantly at the expense of efficiency.

Both efficiency curves are close together between 5 % and 10 %. Evidently, the amount of detectable correct events, which correlates with the distribution of momentum direction, varies only slightly with target thickness. This is in good agree-

ment with the results presented in section 6.3 and in conclusion, the use of thicker targets is recommended. Nevertheless, efficiencies are rather small and an extension of the detection area as proposed in section 6.5 seems reasonable.

7.10 Analysis of reaction channels producing ^{11}C

The analysis of the reaction channel $^{12}\mathrm{C}(\mathrm{p},\mathrm{pn})^{11}\mathrm{C}$ basically follows the concept introduced in section 7.9. In contrast to the reaction $^{12}\mathrm{C}(\mathrm{p},\mathrm{2p})^{11}\mathrm{B}$, a neutron is produced together with a proton and the ion. Due to the lack of neutron-sensitive detection devices, the neutron will escape without being detected by the TOF spectrometer. But as indicated above, it is sufficient to identify the ^{11}C-ion assuming that the reaction with the target protons can be distinguished from the one occurring on target carbon nuclei.

7.10.1 Results

In this context, the distribution of E_{tot} of correctly reconstructed ^{11}C-ions is shown in figure 7.20(a) and figure 7.20(b). Here again, the different colour-coding is applied to distinguish between reactions on protons and carbon nuclei. The kinematic variables E_{tot}, TOF and $\mathrm{d}E/\mathrm{d}x$ of all reconstructed ^{11}C-events can be found in in figures 7.20(c) – 7.22(b).

Also in the reaction considered here, the distinction between reactions with protons and carbon nuclei of the target material is possible. However, the distributions of kinematic variables of true ^{11}C-ions are superimposed by misinterpreted events mostly due to ^{12}C. As was demonstrated in section 7.5, the rather slight difference in mass between carbon isotopes complicates a clear separation.

Here again, a gaussian fit to the TOF and E_{tot} spectra is applied to determine the cut sequence. The resulting values are specified in table 7.1.

7.10.2 Purity and efficiency

The final plots containing purity and efficiency of ^{11}C-events can be found in figure 7.19 including results for both target thicknesses.

As can be seen, the purity and efficiency are rather low, which was to be expected after studying the kinematic variables in the last section. A better performance is can be achieved with the thicker target; a purity of just above 20 % is reached. In contrast, the purity in the case of the 1 mm target is approximately 5 %.

Tab. 7.1: Cut values for the reaction $^{12}C(p, pn)^{11}C$.

E_{tot}		
target	lower cut	higher cut
1 mm	1968.70 MeV	2034.88 MeV
1 cm	1821.18 MeV	1882.95 MeV
TOF		
1 mm	14.23 ns	15.47 ns
1 cm	14.49 ns	15.45 ns

The efficiency is about 10 % in both cases. As stated above, the influence of target thickness on momentum direction is comparable for both targets, so that the number of particle hits on the calorimeter crystals should be comparable too. Here again, the use of a thicker target is recommended.

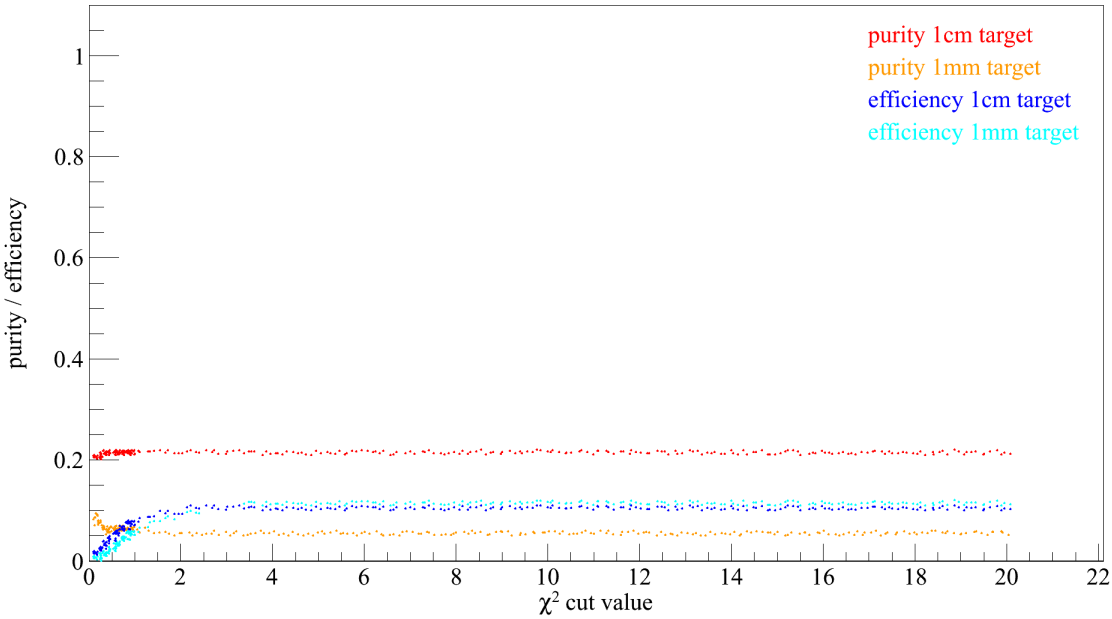

Fig. 7.19: Purity and efficiency of the reaction channel $^{12}C(p, pn)^{11}C$ as a function of the χ^2 value.

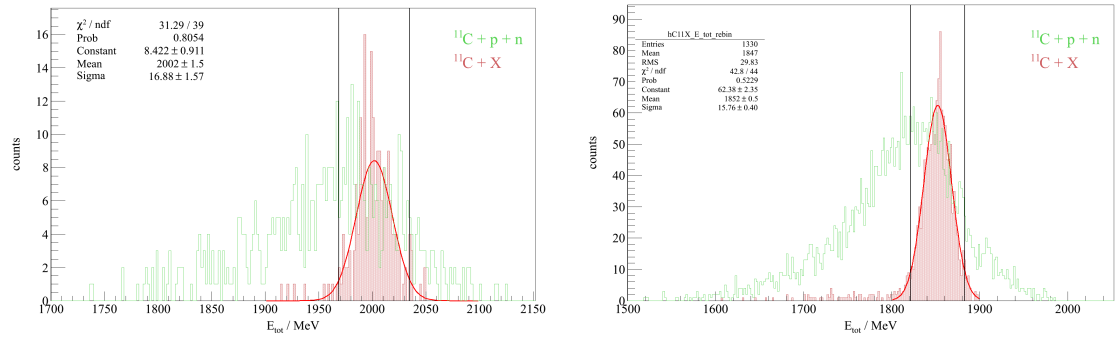

(a) 1 mm target (b) 10 mm target

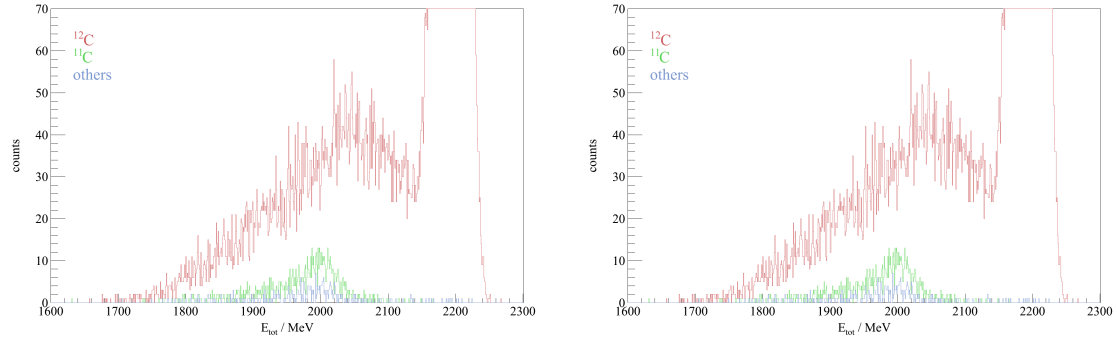

(c) 1 mm target (d) 10 mm target

Fig. 7.20: Total energy depositions E_{tot} of reconstructed ^{11}C-ions, which are really of that type (a), (b). The reactions on target protons is denoted by "$^{11}\mathrm{C} + \mathrm{p} + \mathrm{n}$", the one on target carbon nuclei by "$^{11}\mathrm{C} + \mathrm{X}$". E_{tot}-distribution of all reconstructed ^{11}C-ions (c) – (d).

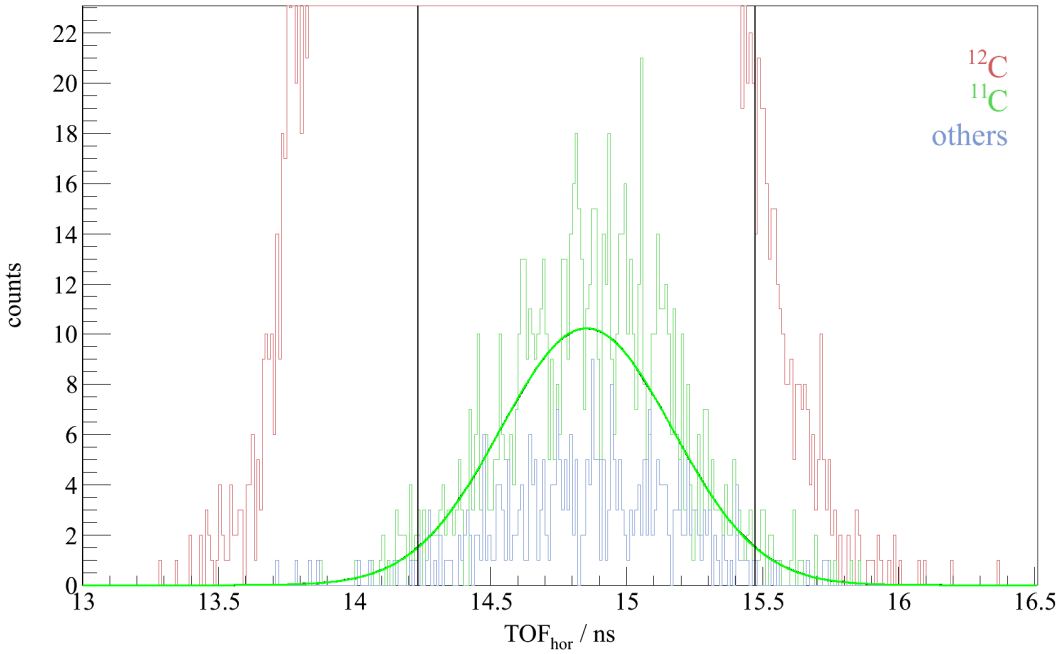

(a) 1 mm target

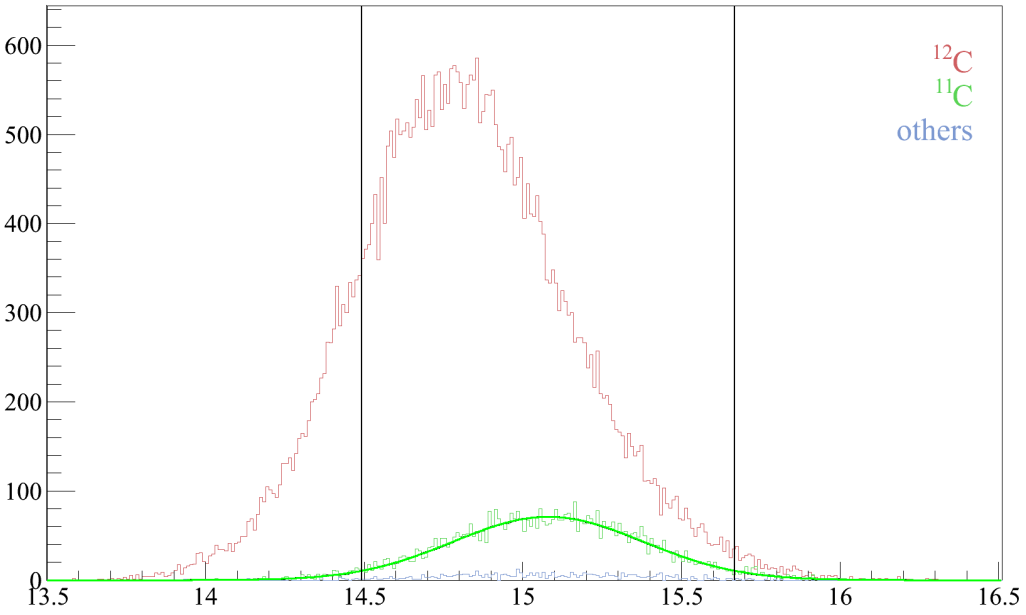

(b) 10 mm target

Fig. 7.21: TOF distribution of reconstructed ^{11}C-ions. The vertical black lines denote the cuts applied in the final analysis.

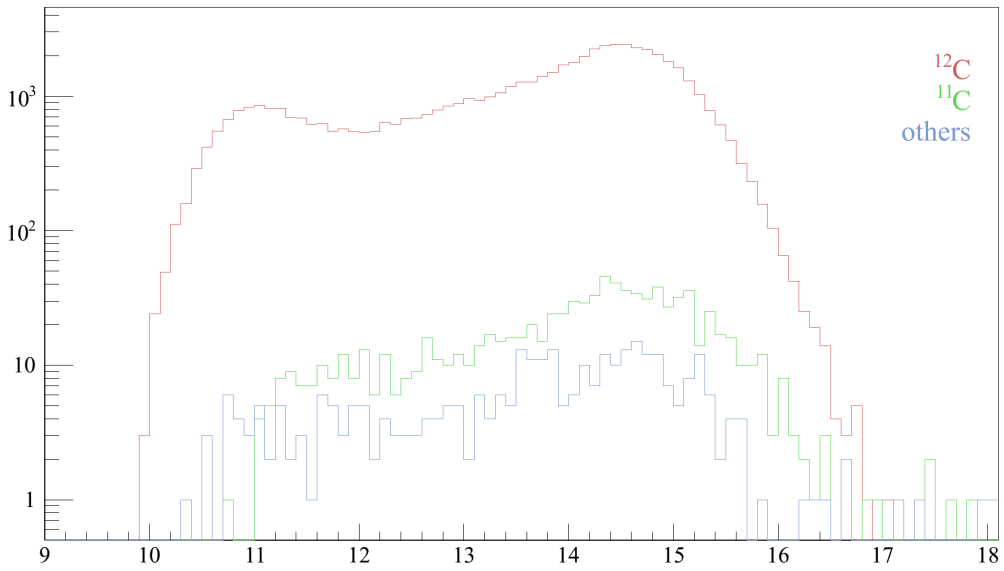

(a) 1 mm target

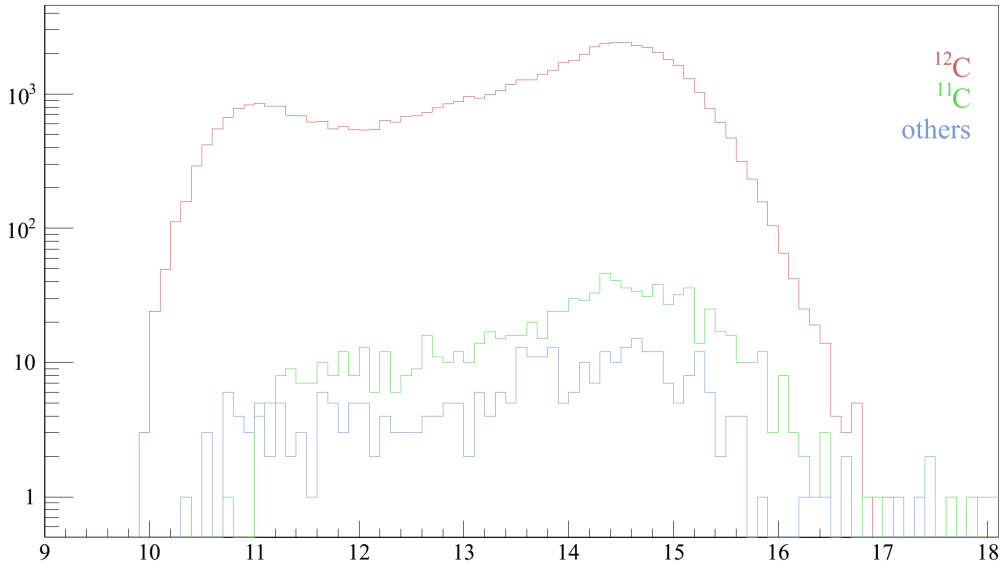

(b) 10 mm target

Fig. 7.22: $\mathrm{d}E/\mathrm{d}x$ distribution of reconstructed ^{11}C-ions.

Chapter 8

Conclusion and outlook

The aim of this thesis was to simulate the newly designed time-of-flight spectrometer of the medical physics group of Physics Institute 3B at RWTH Aachen within the Geant4 framework and to develop a reconstruction mechanism to identify target fragments for event reconstruction.

Prior to the simulation of the present setup, the simulation of the predecessor layout was extended by implementing the beam collimator to study its effects on detector hits. The results have shown that a large proportion of approximately 54 % of detector hits is caused by particles scattered by the collimator material without subsequently hitting the target. Therefore, a shielding is planned to be used for the new spectrometer to increase the ratio of correct to unwanted events.

In order to get an estimate of the solid angle required to be covered by the new detection setup, the angular distribution of target fragments was investigated. The broad distribution of very light fragments (e.g. for protons) with small kinetic energies led to the assumption that event reconstruction could be impaired by not detecting light target fragments. The current assembly of 16 crystals is capable of detecting roughly 40 % of fragments, whereas the fragment rates vary between 25 % for protons and 75 % for ^{12}C-ions. In a subsequent analysis, the calorimeter volume was extended to the diameter of the detection chamber to determine the number of specific target fragment species detectable with a larger number of BGO crystals. A structure of BGO crystals with a diameter of roughly 24 cm is able to detect 90 % of all target fragments.

The evaluation of the energy deposition in the fiber tracker was performed by simulating an irradiation with a radioactive ^{90}Sr source and by analyzing the energy distribution of target fragments. In the former case, the endpoint energy of the energy spectrum could be clearly assigned to the endpoint energy of 2280 keV of the decay product ^{90}Y. The maximum energy deposition on the other hand was estimated to

be roughly 19 MeV for ^{12}C-ions, which led to a proper choice of SiPM for the fiber tracker, namely SiPM of type S10362-11-025 manufactured by Hamamatsu. Finally, the characteristic triple peak structure of $\mathrm{d}E/\mathrm{d}x$ distributions could be explained by different path lengths of fragments when traversing the fiber layers.

The effect of target thickness on momentum direction and energy loss was observed to be smaller than in the predecessor setup due to higher energies of primary particles and thus of target fragments. A deviation of 0.5° or less was observed for roughly 95 %, 90 % and 85 % of target fragments for three different thicknesses of 0.075 mm, 0.1 mm and 10 mm. It was therefore recommended to use thicker targets in the final setup

Concerning the reconstruction framework, the verification of track reconstruction showed overall satisfying results: Standard deviations of $\sigma_{\mathrm{x}} = 0.16\,\mathrm{mm}$ and $\sigma_{\mathrm{y}} = 0.15\,\mathrm{mm}$ for the distribution of differences of true and reconstructed calorimeter positions were observed. Because the size of BGO crystals is much larger, the correct crystal is identified in $95,2\,\%$ to $99.4\,\%$ of all cases depending on which crystal was hit.

Two different detection devices for $\mathrm{d}E/\mathrm{d}x$ and TOF measurement were compared with regard to particle identification. The scintillation bar tracker performed better due to a well-defined path length compared to the round fibers of the fiber tracker. The spatial resolution, however, is inferior to the fiber tracker due to the larger dimensions of the bar tracker stripes.

The analysis of various primary ions with separate smearing of each kinematic variable served as preparation of the final analysis and helped understanding the behavior of PID variation. Especially heavier fragments like carbon ions feature insufficient PID ratios for specific combinations of σ_{TOF}, $\sigma_{\mathrm{d}E/\mathrm{d}x}$ and σ_E. In conclusion, the uncertainty of total energy deposition in the calorimeter plays a minor role compared to σ_{TOF} and $\sigma_{\mathrm{d}E/\mathrm{d}x}$. The uncertainty $\sigma_{\mathrm{d}E/\mathrm{d}x}$ has to be chosen according to the RMS of energy distribution of target fragments. A functional relation between the RMS and the mean of the distribution was established, which was used to calculate $\sigma_{\mathrm{d}E/\mathrm{d}x}$. In the case of TOF, the energy deposition is used to adjust σ_{TOF} and measurements are in good agreement with the theoretical prediction. A timing resolution of 500 ps seems to be reachable for carbon ions as demanded in an earlier analysis.

The final exemplary analysis of the two most frequent reaction channels was realized for target thicknesses of 1 mm and 1 cm. The purity was overall higher for the thicker target. In the case of $^{12}\mathrm{C}(\mathrm{p},2\mathrm{p})^{11}\mathrm{B}$, up to 60 % could be reached for very small χ^2 cut values. The efficiencies were in the range of 5 % to 10 % for small χ^2

cut values before decreasing at a threshold of $\chi^2 \approx 1$. As was expected, the purity of $^{12}\mathrm{C}(\mathrm{p},\mathrm{pn})^{11}\mathrm{C}$ was observed to be lower and led to values of 20 % and 5 %, respectively. The efficiencies were about 10 % for both target thicknesses.

Since the reconstruction framework was applied solely to smeared simulation data, a further test with measured data from a future beam time would be necessary. A more detailed estimation of uncertainties of kinematic variables could be accomplished in addition.

The final analysis of the two most important reaction channels was intended to give a first estimate concerning efficiency and purity. An application of more complex analysis methods or multidimensional cut sequences could be carried out in the future.

Appendix A

Predecessor detection layout

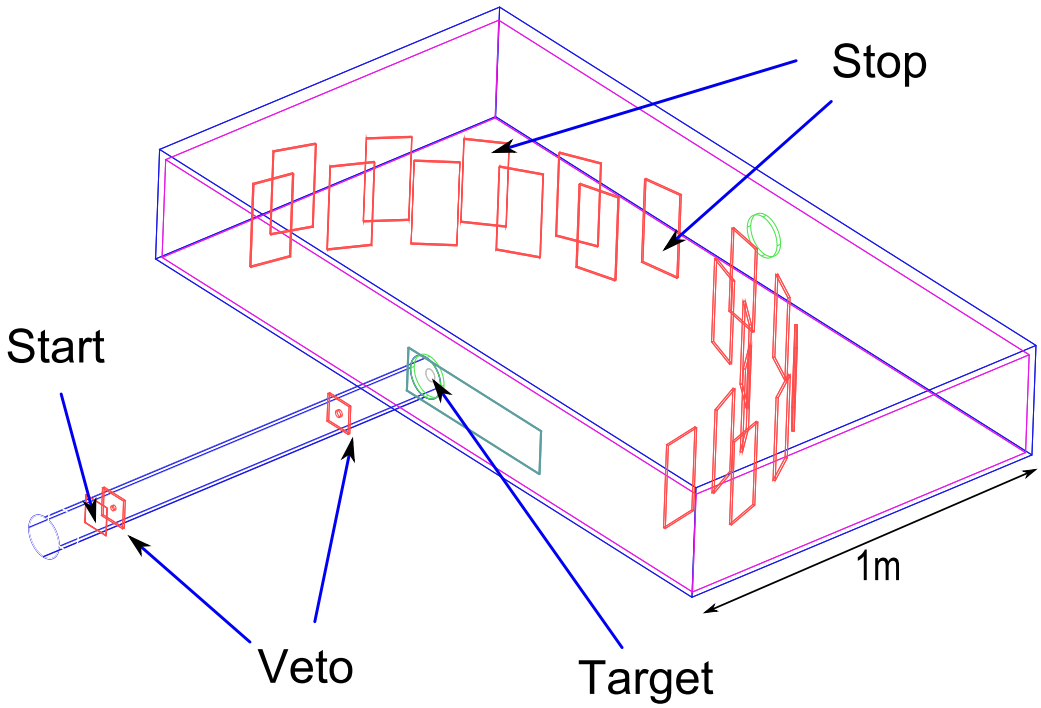

Fig. A.1: Predecessor concept of the TOF spectrometer. The proton beam enters from the left and first hits the start detector to initiate the time measurement. After the beam hits the target, the fragments stemming from nuclear reactions travel towards the stop scintillators to stop the time measurement. The energy loss in the scintillators is further used for $\mathrm{d}E/\mathrm{d}x$ measurement.

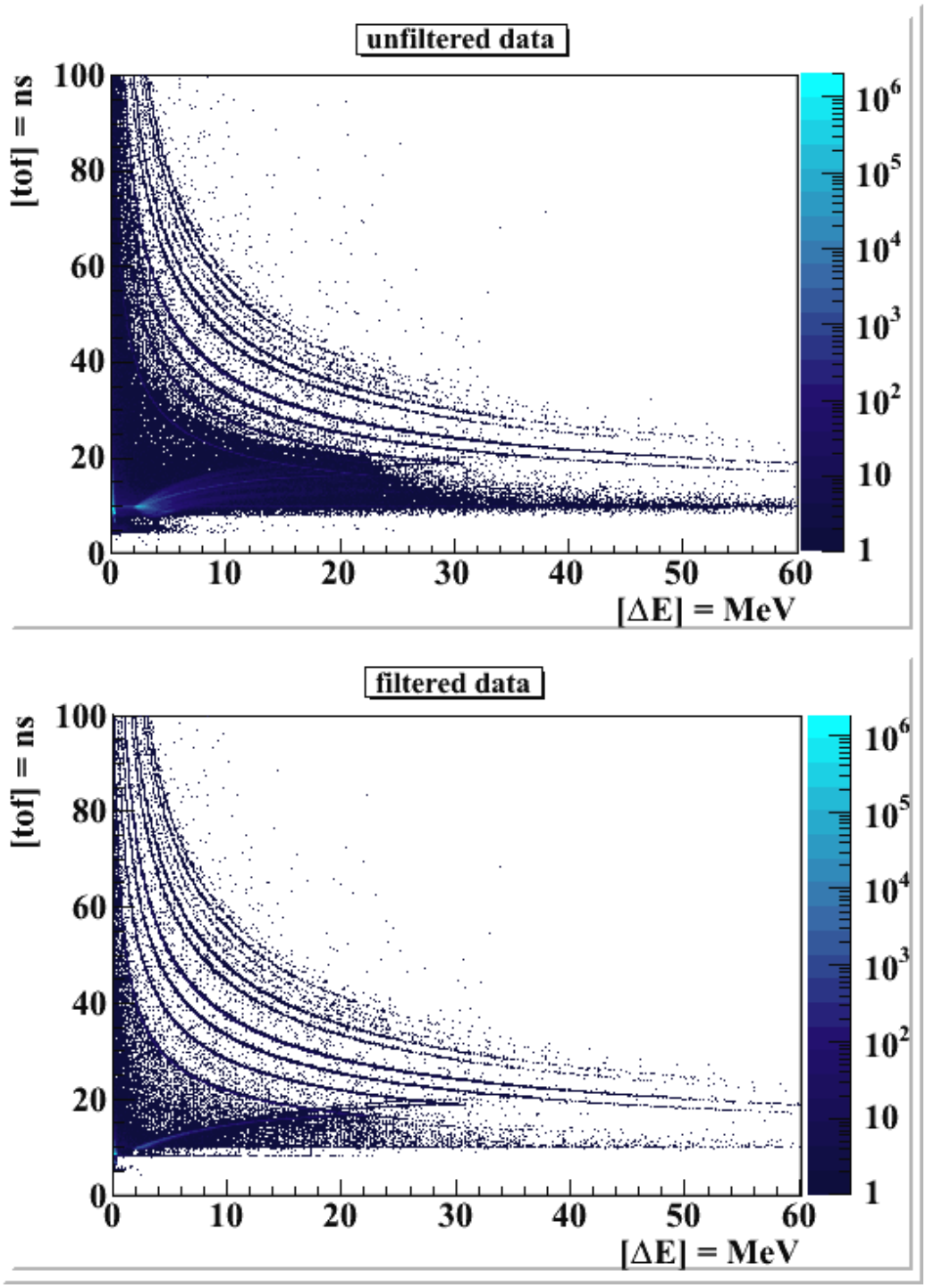

Fig. A.2: Background elimination by the veto system consisting of two veto detectors: Original correlation plot of TOF and dE/dx (top) and a plot after discarding all veto events (bottom) [Grü11].

Appendix B

Photos of detector components

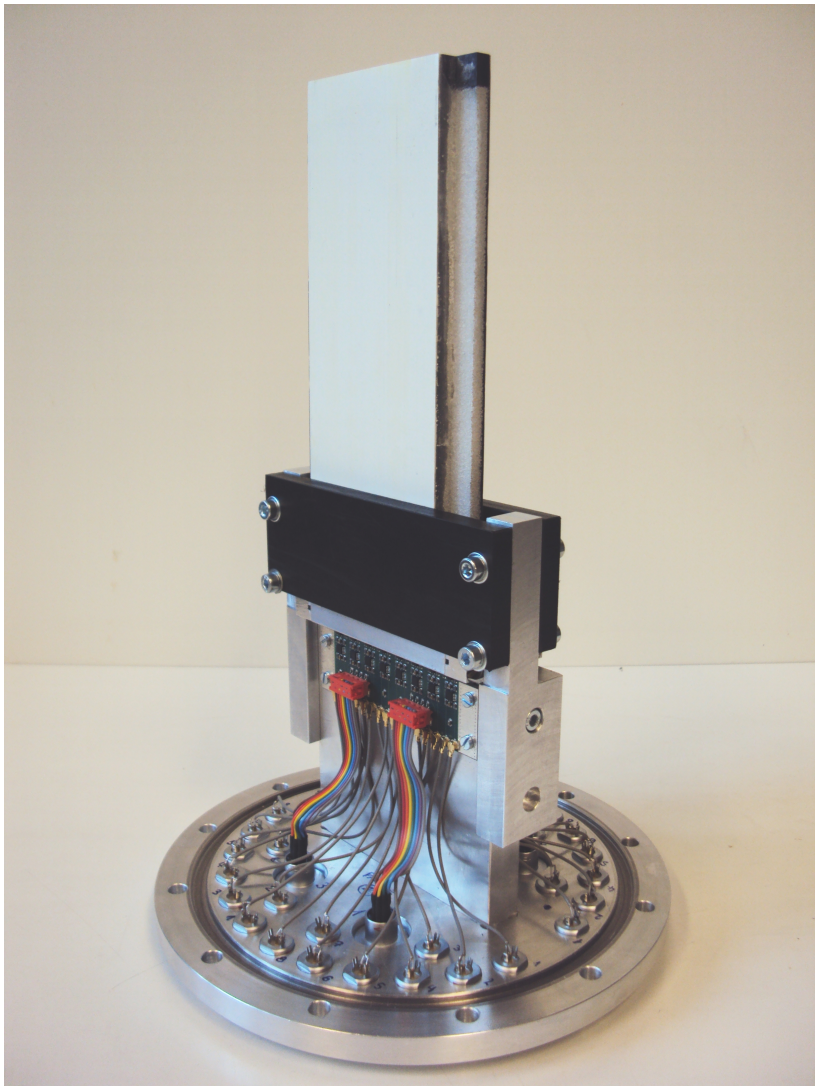

Fig. B.1: Fiber tracker module connected to the flange with a holding clamp and mounted to the preamplifier board.

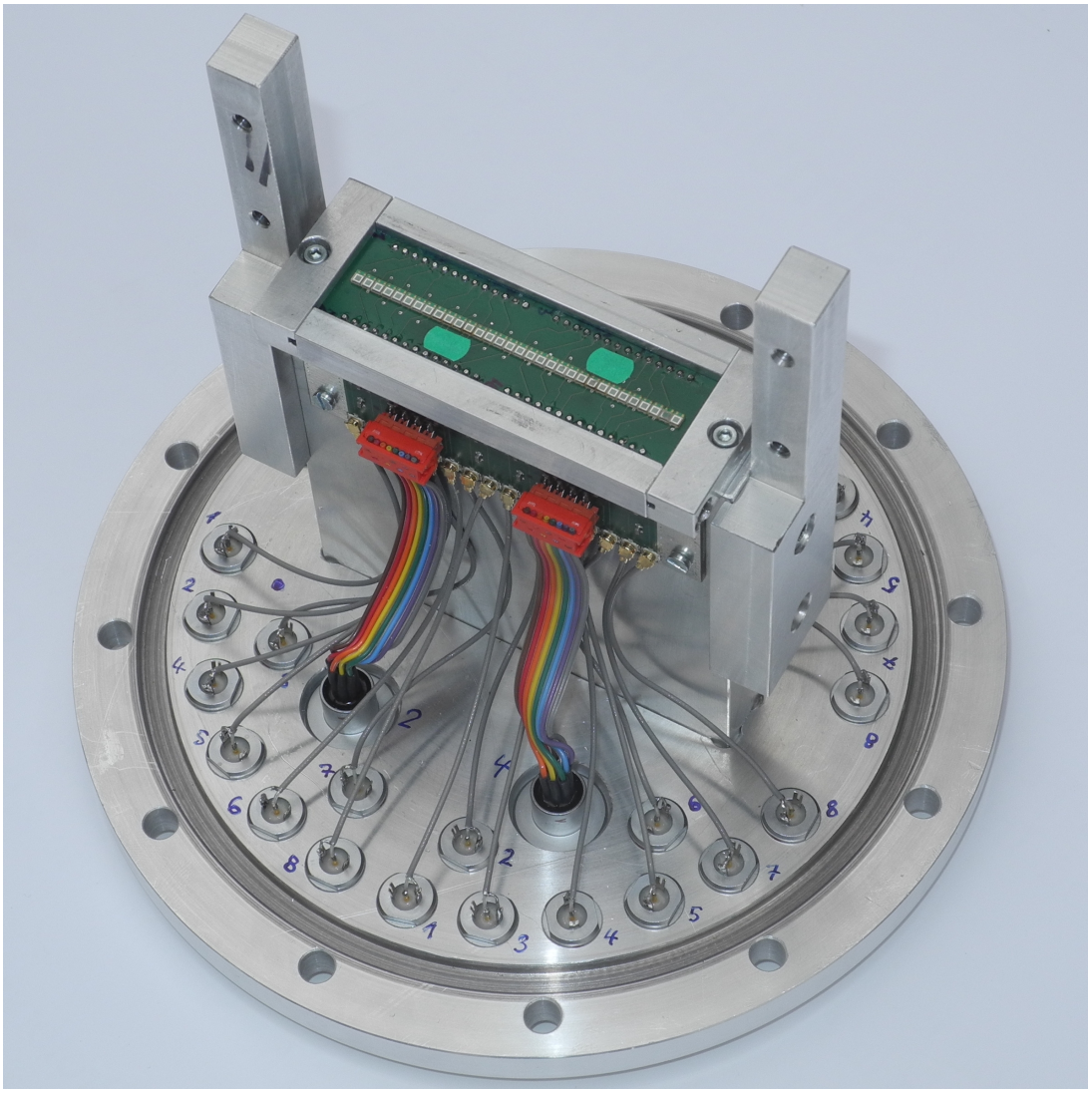

Fig. B.2: Fiber tracker flange with unrigged fiber tracker and the electronics board. On top the 32 SiPM can be seen.

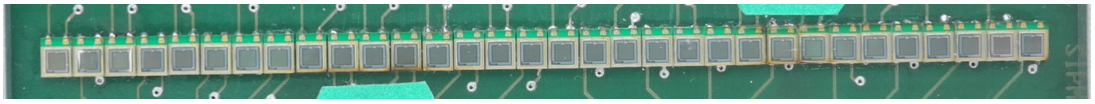

Fig. B.3: Detailed view of the 32 SiPM of a fiber tracker module.

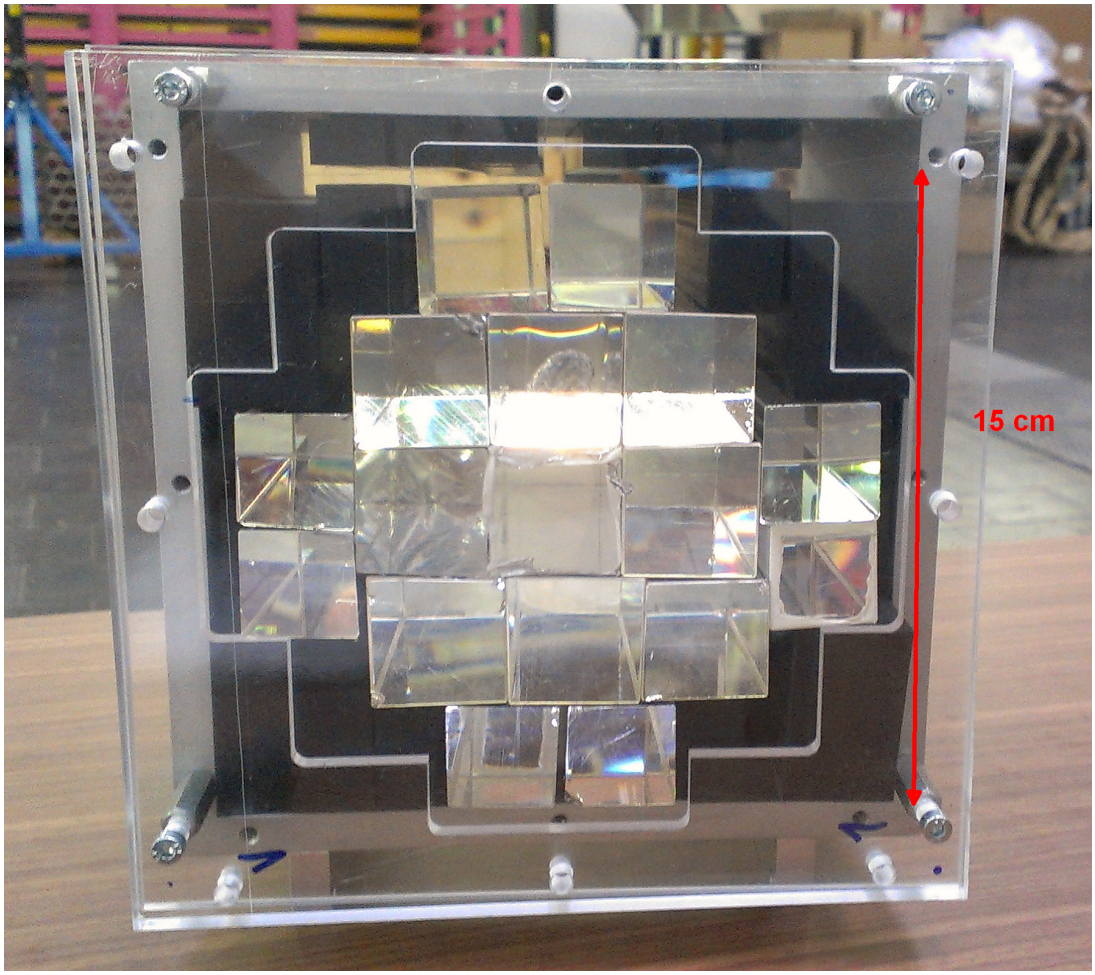

Fig. B.4: Final assembly and orientation of BGO crystals in an aluminium frame viewed against beam direction.

Index

Bibliography

[Ago+98] S. Agosteo et al. “Secondary neutron and photon dose in proton therapy”. In: *Radiother. Oncol.* 48 (1998), pp. 293–305. URL: http://www.biomedsearch.com/nih/Secondary-neutron-photon-dose-in/9925249.html.

[Ago+03] S. Agostinelli et al. “Geant4—a simulation toolkit”. In: *Nucl. Instrum. Meth.* A.506 (2003), pp. 250–303.

[Bac11] F. Bachmair. “Verbesserung eines Flugzeitspektrometers zur Identifikation von Targetfragmenten für die Hadronentherapie”. MA thesis. RWTH Aachen, 2011.

[Bar+66] G. W. Barendsen et al. “The effect of oxygen on impairment of the proliferative capacity of human cells in culture by ionizing radiations of different LET”. In: *International journal of radiation biology and related studies in physics, chemistry, and medicine* 10.4 (1966), pp. 317–327. URL: http://www.biomedsearch.com/nih/effect-oxygen-impairment-proliferative-capacity/5297012.html.

[Bas+12] N. Bassler et al. *SHIELD-HIT12A - User's Guide*. 2012.

[Ber+12] J. Beringer et al. “Review of Particle Physics”. In: *Phys. Rev. D* 86 (2012), pp. 1+. URL: http://link.aps.org/doi/10.1103/PhysRevD.86.010001.

[BWW07] K. Bethge, G. Walter, and B. Wiedemann. *Kernphysik: Eine Einfuhrung*. Springer-Lehrbuch. Springer London, Limited, 2007. URL: http://books.google.de/books?id=1U-OEqsOYykC.

[Bew68] D. K. Bewley. “A comparison of the response of mammalian cells to fast neutrons and charged particle beams”. In: *Radiat. Res.* 34.2 (1968), pp. 446–458. URL: http://www.biomedsearch.com/nih/comparison-response-mammalian-cells-to/5647803.html.

[Boh36] N. Bohr. "Neutron Capture and Nuclear Constitution". In: *Nature* 137 (1936), pp. 344–348, 351. URL: http://www.nature.com/nature/journal/v137/n3461/pdf/137344a0.pdf.

[Boo04] G. Booch. *Object-Oriented Analysis and Design with Applications (3rd Edition)*. Addison Wesley Longman Publishing Co., Inc., 2004.

[Bot+87] A. S. Botvina et al. "Statistical simulation of the break-up of highly excited nuclei". In: *Nuclear Physics A* 475 (1987), pp. 663–686. URL: http://www.sciencedirect.com/science/article/pii/0375947487902326.

[BK05] W. H. Bragg and R. Kleeman. "On the α-particles of radium and their loss of range in passing through various atoms and molecules". In: *Philos. Mag.* 10 (1905), pp. 318–340.

[Bur+04] H. Burkhardt et al. "Geant4 standard electromagnetic package for HEP applications". In: *Proc. Conf. Rec. 2004 IEEE Nuclear Science Symp.* (2004), pp. 1907–1910.

[Cha] J. Chang. *Table of Nuclides*. Available online at http://atom.kaeri.re.kr/ton/; visited on April 12th 2013. KAERI (Korea Atomic Energy Research Institute).

[Cha+01] S. Chauvie et al. "Geant4 low energy electromagnetic physics". In: *Proc. Computing in High Energy and Nuclear Physics* (2001), pp. 337–340.

[Cha+04] S. Chauvie et al. "Geant4 low energy electromagnetic physics". In: *Nuclear Science Symposium Conference Record, 2004 IEEE*. 2004, pp. 1881–1885.

[CTDL99] C. Cohen-Tannoudji, B. Diu, and F. Laloë. *Quantenmechanik*. 2nd ed. Quantenmechanik. De Gruyter, 1999. URL: http://books.google.de/books?id=YL1v77iHXgEC.

[Exf] *Experimental Nuclear Reaction Data (EXFOR)*. Available online at http://www-nds.iaea.org/exfor/exfor.htm; visited on Feb 24th 2013.

[Fer+10] J. Ferlay et al. "Estimates of worldwide burden of cancer in 2008: GLOBOCAN 2008". In: *Int. J. Cancer* 127.12 (2010), pp. 2893–2917. URL: http://dx.doi.org/10.1002/ijc.25516.

[Fer50] E. Fermi. "High Energy Nuclear Events". In: *Progress of Theoretical Physics* 5 (1950), pp. 570–583.

[Fer26] E. Fermi. "Zur Quantelung des idealen einatomigen Gases". In: *Zeitschrift für Physik A Hadrons and Nuclei* 36.11 (1926), pp. 902–912. URL: http://dx.doi.org/10.1007/BF01400221.

[Fer+05] A. Ferrari et al. *Fluka: a multi-particle transport code*. CERN-2005-010, INFN TC 05/11, SLAC-R-773. 2005.

[Fie+06] F. Fiedler et al. "The Feasibility of In-Beam PET for Therapeutic Beams of He". In: *IEEE Transactions on Nuclear Science* 53 (4 2006), pp. 2252–2259.

[Fow89] J. F. Fowler. "The Linear Quadratic Formula and Progress in Fractionated Radiotherapy". In: *British Journal of Radiology* 62 (1989), pp. 679–694.

[Fri72] E. Frieden. "The chemical elements of life." In: *Scientific American* 227 (1972), pp. 52–60. URL: http://www.biomedsearch.com/nih/chemical-elements-life/5044408.html.

[Fur+00] Y. Furusawa et al. "Inactivation of aerobic and hypoxic cells from three different cell lines by accelerated (3)He-, (12)C- and (20)Ne-ion beams". In: *Radiat. Res.* 154.5 (2000), pp. 485–496. URL: http://www.biomedsearch.com/nih/Inactivation-aerobic-hypoxic-cells-from/11025645.html.

[Geaa] Geant4 Collaboration. Website. Available online at http://geant4.cern.ch/support/proc_mod_catalog/models/hadronic/BinaryCascade.html; visited on March 1st 2013.

[Gea12] Geant4 Collaboration. *Geant4 User's Guide for Application Developers*. 2012. URL: http://geant4.web.cern.ch/geant4/UserDocumentation/UsersGuides/ForApplicationDeveloper/html/index.html.

[Geab] Geant4 Collaboration. *Physics Lists EM constructors in Geant4 9.4*. Available online at https://geant4.cern.ch/collaboration/working_groups/electromagnetic/physlist9.4.shtml; visited on January 23th 2013.

[Gea10] Geant4 Collaboration. *Physics Reference Manual*. version 9.4. 2010. URL: http://geant4.web.cern.ch/geant4/UserDocumentation/UsersGuides/PhysicsReferenceManual/BackupVersions/V9.4/fo/PhysicsReferenceManual.pdf.

[Ges08] K. Gester. “Aufbau und Simulation eines Flugzeitspektrometers zur Messung von Targetfragmenten für die Strahlentherapie”. MA thesis. RWTH Aachen, 2008.

[GM49] M. Goeppert-Mayer. “On Closed Shells in Nuclei. II”. In: *Phys. Rev.* 75 (12 1949), pp. 1969–1970. URL: http://link.aps.org/doi/10.1103/PhysRev.75.1969.

[Gre+10] L. Grevillot et al. “Optimization of GEANT4 settings for Proton Pencil Beam Scanning simulations using GATE”. In: *Nuclear Instruments and Methods in Physics Research Section B: Beam Interactions with Materials and Atoms* (2010). URL: http://dx.doi.org/10.1016/j.nimb.2010.07.011.

[Gri66] J. J. Griffin. “Statistical Model of Intermediate Structure”. In: *Phys. Rev. Lett.* 17 (1966), pp. 478–481. URL: http://link.aps.org/doi/10.1103/PhysRevLett.17.478.

[GDR12] B. Grimm and A. De Rose. “Design und Simulation einer Abschirmung für ein Flugzeitspektrometer”. Bachelor’s Thesis. RWTH Aachen, 2012.

[Grü11] O. Grünwald. “GEANT4 simulation and evaluation of a time-of-flight spectrometer for nuclear cross section measurements in particle therapy”. PhD thesis. RWTH Aachen, 2011.

[Con] *HTCondor Version 7.8.8 Manual*. Center for High Throughput Computing, University of Wisconsin–Madison, 2013. URL: http://research.cs.wisc.edu/htcondor/manual/v7.8/index.html.

[HJS49] O. Haxel, J. H. D. Jensen, and H. E. Suess. “On the "Magic Numbers" in Nuclear Structure”. In: *Phys. Rev.* 75 (11 1949), pp. 1766–1766. URL: http://link.aps.org/doi/10.1103/PhysRev.75.1766.2.

[Hei] Heidelberg Ion-Beam Therapy Center (HIT). Website. Available online at http://www.klinikum.uni-heidelberg.de/index.php?id=112987&L=1; visited on March 21st 2013.

[Hol05] N. E. Holden. *A Short History of CSISRS*. Report BNL-75288-2005-IR. Brookhaven National Laboratory. 2005.

[Hüf85] J. Hüfner. *Heavy Fragments Produced in Proton-nucleus and Nucleus-nucleus Collisions at Relativistic Energies*. Physics reports. North-Holland, 1985.

[II93] International Commission on Radiation Units and Measurements and International Commission on Radiological Units and Measurements. *ICRU Report*. ICRU Report Nr. 51. International Commission on Radioation Units and Measurements, 1993.

[Iva11] V. Ivantchenko. private communication. Geant4 Training Event on Calorimetry in HEP. 2011.

[JP08] C. Z. Jarlskog and H. Paganetti. "Physics Settings for Using the Geant4 Toolkit in Proton Therapy". In: *Nuclear Science, IEEE Transactions on* 55 (2008), pp. 1018–1025.

[Kos13] B. Koska. "Assembly of a BGO-Calorimeter for Nuclear Cross Section Measurements for Particle Therapy". Diploma Thesis. RWTH Aachen, 2013.

[KV07] G. Kraft and Vereinigung zur Förderung der Tumortherapie mit schweren Ionen. *Tumor Therapy with Heavy Ions: Physical and Biological Basis, Technical Realization at GSI, Clinical Results*. Association for the Promotion of Tumor Therapy with Heavy Ions, 2007. ISBN: 9783981129823.

[KM10] E. Kreysing and A. Mantz. "Bau und Test eines Startdetektors mit SiPM-Auslese für ein Flugzeitspektrometer". Bachelor's Thesis. RWTH Aachen, 2010.

[Kur] Kuraray. Website. Available online at `http://kuraraypsf.jp/psf/sf.html`; visited on March 1st 2013.

[LW00] *Pre-equilibrium and equilibrium decays in Geant4*. International Conference on Computing in High Energy and Nuclear Physics. Padua, Italy, 2000, pp. 52–55.

[Lew12] R. K. Lewke. "Integration of a Fiber Tracker into a Time-of-Flight Spectrometer for Nuclear Cross Section Measurements for Particle Therapy". MA thesis. RWTH Aachen, 2012.

[Mat+99] N. Matsufuji et al. "The response of a BGO scintillator to relativistic heavy ions". In: *Nucl. Instrum. Methods Phys. Res., A* 430.1 (1999), pp. 60–68.

[MN98] M. Matsumoto and T. Nishimura. "Mersenne twister: a 623-dimensionally equidistributed uniform pseudo-random number generator". In: *ACM Trans. Model. Comput. Simul.* 8 (1998), pp. 3–30. URL: http://doi.acm.org/10.1145/272991.272995.

[MK94] T. Mayer-Kuckuk. *Kernphysik*. Stuttgart: Teubner, 1994.

[Met87] N. Metropolis. "The beginning of the Monte Carlo method". In: *Los Alamos Science* (1987). URL: http://jackman.stanford.edu/mcmc/metropolis1.pdf.

[MU49] N. Metropolis and S. Ulam. "The Monte Carlo method". In: *Journal of the American statistical Association* 44.247 (1949), pp. 335–341.

[New+07] W. Newhauser et al. "Monte Carlo simulations for configuring and testing an analytical proton dose-calculation algorithm". In: *Physics in Medicine and Biology* 52 (2007), p. 4569. URL: http://stacks.iop.org/0031-9155/52/i=15/a=014.

[PTC] PTCOG: Particle Therapy Co-Operative Group. Website. Available online at http://ptcog.web.psi.ch/ptcentres.html; visited on November 14th 2012.

[Pag+02] H. Paganetti et al. "Relative biological effectiveness (RBE) values for proton beam therapy". In: *International Journal of Radiation Oncology * Biology * Physics* 53.2 (2002), pp. 407–421. URL: http://www.biomedsearch.com/nih/Relative-biological-effectiveness-RBE-values/12023146.html.

[PEH02] K. Parodi, W. Enghardt, and T. Haberer. "In-beam PET measurements of β^+ + radioactivity induced by proton beams". In: *Phys. Med. Biol* 47 (2002), pp. 21–36. URL: http://stacks.iop.org/0031-9155/47/i=1/a=302.

[PPE04] K. Parodi, F. PÄ¶nisch, and W. Enghardt. "The Feasibility of In-Beam PET for Accurate Monitoring of Proton Therapy: Results of a Comprehensive Experimental Study". In: *Nuclear Science Symposium Conference Record, 2004 IEEE*. Vol. 4. 2004, pp. 2160–2164.

[Pia+10] M. G. Pia et al. "Physics-related epistemic uncertainties in proton depth dose simulation". In: *IEEE Trans. Nucl. Sci.* 57 (2010), pp. 2805–2830.

[Raj+78] M. R. Raju et al. "A heavy particle comparative study". In: *Br. J. Radiol.* 51 (1978), pp. 699–703.

[RG12] Robert Koch-Institut and Gesellschaft der epidemiologischen Krebsregister in Deutschland e.V. “Krebs in Deutschland 2007/2008”. In: (2012).

[Roh] Rohm and Haas Company. Website. Available online at `http://www.rohmhaas.com/history/ourstory/innovation_plexiglastriumphs.htm`; visited on November 28th 2012.

[Saia] Saint-Gobain Crystals. Website. Available online at `http://www.detectors.saint-gobain.com/BGO.aspx`; visited on March 1st 2013.

[Saib] Saint-Gobain Crystals. *BC-418, BC-420, BC-422 Premium Plastic Scintillator Product Data Sheet*. Website. Available online at `http://www.detectors.saint-gobain.com/uploadedFiles/SGdetectors/Documents/Product_Data_Sheets/BC418-420-422-Data-Sheet.pdf`; visited on March 1st 2013.

[Sau10] R. Sauer. *Strahlentherapie und Onkologie*. 5th ed. Urban und Fischer, 2010.

[Saw03] S. S. Sawilowsky. “You think you’ve got trivials?” In: *J. Mod. Appl. Stat. Methods.* 2 (2003), pp. 218–225.

[SESE10] D. Schardt, T. Elsässer, and D. Schulz-Ertner. “Heavy-ion tumor therapy: Physical and radiobiological benefits”. In: *Rev. Mod. Phys.* 82 (1 2010), pp. 383–425. URL: `http://link.aps.org/doi/10.1103/RevModPhys.82.383`.

[SBG06] W. Schlegel, T. Bortfeld, and A. L. Grosu. *New technologies in Radiation Oncology*. Medical radiology. Springer, 2006. URL: `http://books.google.de/books?id=Ao5rAAAAMAAJ`.

[Sch09] L. L. Schlömer. “Planung und Aufbau eines Flugzeitspektrometers zur Messung von inelastischen Kernreaktionen für die Teilchentherapie”. MA thesis. RWTH Aachen, 2009.

[Sch+02] U. Schneider et al. “Secondary neutron dose during proton therapy using spot scanning”. In: *International Journal of Radiation Oncology*Biology*Physics* 53 (2002), pp. 244–251. URL: `http://www.sciencedirect.com/science/article/B6T7X-45SJ6XK-15/2/55d89bdc0b5a81aa1502d7c4beab7928`.

[Ser47] R. Serber. “Nuclear Reactions at High Energies”. In: *Phys. Rev.* 72 (11 1947), pp. 1114–1115. URL: `http://link.aps.org/doi/10.1103/PhysRev.72.1114`.

[Sta+04] A. Staab et al. “Response of Chinese hamster v79 multicellular spheroids exposed to high-energy carbon ions”. In: *Radiat. Res.* 161.2 (2004), pp. 219–227. URL: http://www.biomedsearch.com/nih/Response-Chinese-hamster-v79-multicellular/14731067.html.

[The] The ROOT team. Website. Available online at http://root.cern.ch/root/htmldoc/TRandom3.html; visited on December 19th 2012.

[The07] The ROOT team. *ROOT User's Guide*. Ed. by R. Brun and F. Rademakers. 5.26. CERN. 2007. URL: http://root.cern.ch/drupal/content/users-guide.

[VSS12] J. M. Verburg, H. A. Shih, and J. Seco. “Simulation of prompt gamma-ray emission during proton radiotherapy”. In: *Physics in Medicine and Biology* 57.17 (2012), p. 5459. URL: http://stacks.iop.org/0031-9155/57/i=17/a=5459.

[Wat02] L. S. Waters. *MCNPX USER'S MANUAL, Version 2.3.0*. Report LA-UR-02-2607. Los Alamos National Library. 2002.

[WE40] V. F. Weisskopf and D. H. Ewing. “On the Yield of Nuclear Reactions with Heavy Elements”. In: *Phys. Rev.* 57 (6 1940), pp. 472–485. DOI: 10.1103/PhysRev.57.472. URL: http://link.aps.org/doi/10.1103/PhysRev.57.472.

[Wey04] W. K. Weyrather. “Medical Applications of Accelerated Ions”. In: *The Euroschool Lectures on Physics with Exotic Beams, Vol. I*. Vol. 651. Lecture Notes in Physics. Springer Berlin Heidelberg, 2004, pp. 469–490. URL: http://dx.doi.org/10.1007/978-3-540-44490-9_12.

[ZJP08] C. Zacharatou Jarlskog and H. Paganetti. “Risk of developing second cancer from neutron dose in proton therapy as function of field characteristics, organ, and patient age”. In: *Int J Radiat Oncol Biol Phys* 72 (2008), pp. 228–35. URL: http://www.biomedsearch.com/nih/Risk-developing-second-cancer-from/18571337.html.

[ZM89] J. F. Ziegler and J. M. Manoyan. “The Stopping of Ions in Compounds”. In: *Nucl. Instr. Meth. B* 35 (1989), pp. 215–228.